Reconstitution and Membrane Topology of Mistic from *Bacillus subtilis*

vom Fachbereich Biologie der
Universität Kaiserslautern
zur Verleihung des akademischen Grades
"Doktor der Naturwissenschaften"
(Doctor rerum naturalium, Dr. rer. nat.)

genehmigte D i s s e r t a t i o n

in der Wissenschaftsdisziplin
"Molekulare Biophysik"

von Herrn Dipl.-Biol. Martin Textor

Betreuer: Prof. Dr. Sandro Keller

Wissenschaftliche Aussprache: 29.03.2016
Erstgutachter: Prof. Dr. Sandro Keller
Zweitgutachter: Prof. Dr. Johannes Herrmann
Vorsitzender: Prof. Dr. Stefan Kins

Kaiserslautern, 2016

D 386

Contents

1 Abstract

Cells and organelles are enclosed by membranes that consist of a lipid bilayer harboring highly diverse membrane proteins (MPs). These carry out vital functions, and α-helical MPs, in particular, are of outstanding pharmacological importance, as they comprise more than half of all drug targets. However, knowledge from MP research is limited, as MPs require membrane-mimetic environments to retain their native structures and functions and, thus, are not readily amenable to *in vitro* studies. To gain insight into vectorial functions, as in the case of channels and transporters, and into topology, which describes MP conformation and orientation in the context of a membrane, purified MPs need to be reconstituted, that is, transferred from detergent micelles into a lipid-bilayer system.

The ultimate goal of this thesis was to elucidate the membrane topology of Mistic, which is an essential regulator of biofilm formation in *Bacillus subtilis* consisting of four α-helices. The conformational stability of Mistic has been shown to depend on the presence of a hydrophobic environment. However, Mistic is characterized by an uncommonly hydrophilic surface, and its helices are significantly shorter than transmembrane helices of canonical integral MPs. Therefore, the means by which its association with the hydrophobic interior of a lipid bilayer is accomplished is a subject of much debate. To tackle this issue, Mistic was produced and purified, reconstituted, and subjected to topological studies.

Reconstitution of Mistic in the presence of lipids was performed by lowering the detergent concentration to subsolubilizing concentrations via addition of cyclodextrin. To fully exploit the advantages offered by cyclodextrin-mediated detergent removal, a quantitative model was established that describes the supramolecular state of the reconstitution mixture and allows for the prediction of reconstitution trajectories and their cross points with phase boundaries. Automated titrations enabled spectroscopic monitoring of Mistic reconstitutions in real time.

On the basis of the established reconstitution protocol, the membrane topology of Mistic was investigated with the aid of fluorescence quenching experiments and oriented circular dichroism spectroscopy. The results of these experiments reveal that Mistic appears to be an exception from the commonly observed transmembrane orientation of α-helical MPs, since it exhibits a highly unusual in-plane topology, which goes in line with recent coarse-grained molecular dynamics simulations.

2 Introduction

2.1 Membrane Proteins

According to the seminal fluid mosaic model coined by Sanger and Nicholson [1], cells and organelles are enclosed by membranes comprising a two-dimensional fluid lipid bilayer that harbors embedded proteins in varying abundance [2]. The lipid matrix itself serves as a permeability barrier, whereas most cellular functions of a membrane are mediated by the proteins residing in it. The latter exert a plethora of essential duties in living organisms of all domains such as trafficking, energy and signal transduction, adhesion, cell–cell communication, motility, and more. Many membrane proteins (MPs) have extramembranous domains that are very similar to water-soluble proteins in terms of structure and electrostatics, but their association with the apolar membrane core is rendered possible by domains that are highly hydrophobic. However, the hydrophobicity of MPs is not organized oppositely to water-soluble proteins, which have a hydrophilic surface and an apolar interior; instead, the internal hydrophobicity of both water-soluble proteins and MPs is comparable, but the lipid-exposed residues of MPs are even more hydrophobic [3].

The apolar membrane domains of MPs are structurally characterized by either of two major motifs. First, the assembly of antiparallel β-strands to closed, cylindrical β-sheets results in β-barrels. Porins found in the outer membranes of gram-negative bacteria, mitochondria, and chloroplasts [4] are important representatives of this motif. Nevertheless, the most abundant class of MPs are α-helical proteins. About a quarter of all open reading frames putatively encode α-helical MPs [5], and their importance for pharmaceutical research, in particular, is reflected in the fact that they represent more than half of all drug targets in the human body [6]. However, knowledge of the structure and function of MPs substantially lags behind that of water-soluble proteins because of the difficulties in handling and studying them *in vitro*.

On the one hand, bacterial production of recombinant MPs is challenged by the need of membrane trafficking mediated by the translocon machinery [7]. The expression host often suffers from cytotoxicity because membrane insertion of the recombinant MP dominates over that of vital host MPs. This complication may be mitigated to some extent by using weak promoters and low-copy-number plasmids, which either requires large culture volumes or results in low yields [8]; by directing the MP to inclusion bodies, which requires subsequent refolding [9]; by choosing a different MP variant or host [10]; or by completely avoiding bacterial expression by using a cell-free system instead [11]. On the other hand, a major hurdle

is the requirement of a hydrophobic environment in all steps of MP research, as it is essential for MPs to retain their native and biologically active structure. The high energetic penalty that is associated with both the removal of a hydrophobic MP from its lipidic environment and exposure of its polypeptide backbone to the lipidic surrounding because of structural perturbation [12, 13] is reflected in the fact that MPs usually resist complete thermal or denaturant-induced unfolding [14].

2.1.1 Hydrophobic Environments

Detergent Micelles Detergents are widely used to confer water-solubility and maintain conformational stability of MPs in the absence of their native hydrophobic environment and, thus, are an invaluable tool for MP research [15]. They belong to the class of surfactant compounds and mediate MP solubilization by adsorbing to the interface between hydrophobic protein surface and polar aqueous bulk. The surface activity of detergents is due to their amphiphilic structure consisting of a polar headgroup and an apolar hydrocarbon moiety (Fig. 2.1A). The latter most often consists of a linear *n*-alkyl chain of 8–18 carbon atoms, whereas the headgroup is either ionic, zwitterionic, or nonionic. Owing to their hydrophobic portion, the solubility of detergent monomers in aqueous solvent is limited to low concentrations. At higher concentrations, the hydrophobic effect enforces a minimization of the entropically unfavorable exposure of the alkyl tails to water [16]. Thus, detergents reduce the water-accessible surface of their nonpolar tails by self-aggregation into non-covalent assemblies called micelles when the monomer concentration exceeds a certain concentration range [17] (Fig. 2.1A). As the hydrophilic headgroups tend to occupy a larger molecular area than the tails, the monomers of most detergents are cone-shaped and, hence, give rise to an—on average—spherical or ellipsoidal micelle structure with most of the hydrophobic tails buried inside. Nevertheless, micelles have a rather "rough" surface and are packed in a relatively disordered manner with some tails being substantially exposed to the solvent [15, 18]. The size of micelles depends on the average number of detergent monomers per micelle, the aggregation number.

The formation of micelles, referred to as micellization, is accompanied by a fairly abrupt change in various physical properties of the aqueous detergent solution at a specific concentration, the critical micelle concentration (CMC) [19]. However, it is important to note that micellization actually does not occur at a single concentration, but rather over a narrow concentration range. Nevertheless, the CMC is a fundamental characteristic of a detergent because MP solubilization is dependent on the presence of micelles, and, thus, the CMC dictates the amount of detergent required to solubilize an MP. Provided that micellization obeys a pseudophase model, which holds true for detergents with high aggregation numbers, free

detergent monomers remain present at an almost constant concentration equal to the CMC at total detergent concentrations above the CMC [20]. Detergents with low aggregation numbers show a dependence of monomer activity on total detergent concentration and require other theoretical models to describe micellization [21].

Several physicochemical properties of detergent monomers affect the CMC. Generally, the CMC is higher for detergents with ionic headgroups as compared with zwitterionic or nonionic headgroups because electrostatic repulsion between the equally charged headgroups of neighboring detergent monomers disfavors micellization. Likewise, larger headgroups give rise to higher CMCs because of better water solubility and to lower aggregation numbers because of increased steric repulsion. Also, the CMCs of detergents with ionic headgroups are reduced at increased ionic strength because of the shielding of charges. Moreover, the CMC decreases with increasing length of linear alkyl chains because the larger hydrophobic surface area intensifies the hydrophobic effect.

Frequently, a plethora of different detergents need to be screened to find a candidate suitable for solubilization of an MP of interest. Nevertheless, a detergent found to be optimal for the isolation of an MP need not necessarily be the best choice for downstream purification and biochemical studies. Ultimately, in each individual case, the MP together with the experimental purpose dictates the physicochemical requirements that need to be met by a detergent.

Lipid Bilayers Similar to detergents, phospholipid molecules are well-segregated into a polar and a nonpolar moiety (Fig. 2.1B). However, phospholipids bear two acyl chains, which results in an even lower solubility of less than 10^{-8} M [22]. The acyl chains occupy an area similar to that of the polar headgroup, resulting in a cylindrical shape of the molecule. Therefore, lipid monomers tend to aggregate into planar bilayers that consist of two monomolecular leaflets with an overall thickness of $\sim$40 Å (Fig. 2.1B). The two interfaces between the hydrophobic core of a lipid bilayer and the aqueous solvent are formed by the lipid headgroup regions, whereas the acyl chains make up an inner core with a hydrophobic thickness of $\sim$30 Å that may vary with lipid acyl chain length [23]. At physiological temperatures and lipid compositions, bilayers persist in the liquid–crystalline L_α phase and, thus, are fluid, allowing free lateral diffusion of the lipid monomers. The fluidity of a bilayer can further be increased by unsaturated or branched lipid acyl chains, which disrupt lipid packing. Moreover, fluidity is higher for short-tailed lipids as compared with long-tailed lipids because their hydrophobic chains undergo fewer stabilizing van der Waals interactions. Owing to thermal disorder, the positions of lipid monomer moieties along the bilayer normal are not fixed but rather follow smooth distributions [23], and, likewise, the changes in physical properties across the bilayer are gradual. Most importantly, the local relative permittivity decreases from $\sim$80 in the aqueous solvent to $\sim$10–30 in the headgroup

region [24, 25] and ∼2 in the hydrophobic core [25, 26], where the effect of electrostatic forces is most pronounced.

In vitro experiments that aim at deepening the understanding of native characteristics of MPs necessitate a hydrophobic environment that resembles that of a biological membrane more closely than a detergent micelle. To this end, simplified membrane-mimicking systems of different architectures and compositions have been developed allowing breaking down the complexity of a dynamic, anisotropic, and chemically heterogeneous natural membrane into individual biophysical properties [27]. For many functional studies, particularly on MPs with vectorial function such as channels and transporters, a model lipid bilayer that provides compartmentalization is necessary. The most common bottom-up systems for this purpose are differently sized unilamellar phospholipid vesicles, which provide an internal aqueous compartment and, in the most simple case, consist of a single type of phospholipid [28]. With a toolbox of preparation techniques and different lipids to choose from that can also be combined, specific biophysical properties of the vesicle lipid bilayer such as intrinsic curvature, asymmetry, hydrophobic thickness, and lateral pressure profile can be tailored.

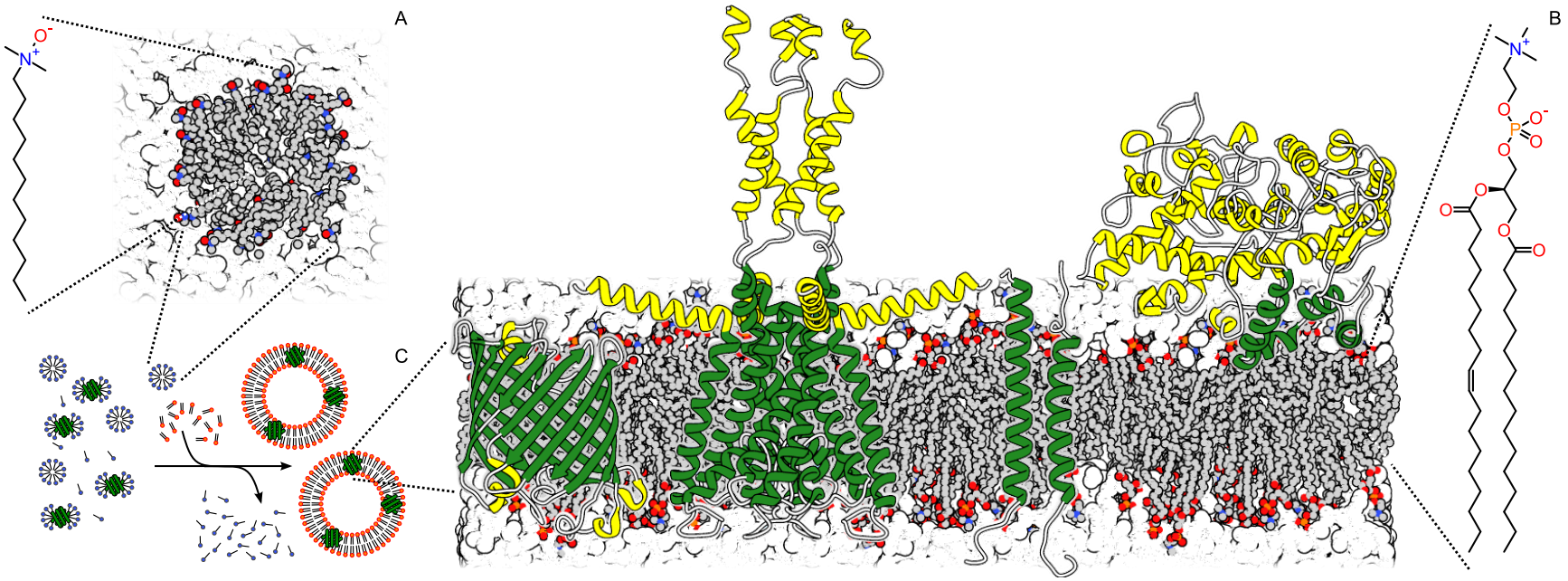

Figure 2.1: Membrane-Protein Topology and Reconstitution.
(A) (Left) Structure of the detergent *n*-dodecyl-*N,N*-dimethylamine-*N*-oxide (LDAO), which comprises a zwitterionic headgroup and an alkyl chain of 12 carbon atoms. (Right) Schematic cross section of a detergent micelle composed of LDAO monomers. The hydrocarbon tails are not completely burried, and there is a fast interchange of monomers between micelle and aqueous bulk. (B) (Right) Structure of the lipid 1-palmitoyl-2-oleoyl-*sn*-glycero-3-phosphocholine (POPC), which comprises a choline headgroup with phosphate and glycerol moieties and two acyl chains of 16 and 18 carbon atoms, the latter of which is unsatturated. (Left) Schematic cross section of a lipid bilayer composed of POPC monomers. The bilayer comprises (gray) a hydrophobic core and (red/blue/orange) two headgroup regions. Solvent molecules are indicated as white spheres to illustrate their deep penetration into the headgroup region. Models of different MPs illustrate main topologies, from right to left: a monotopic MP (cyclooxgenase–2, PDB 5COX [29]), a heterodimer of a bitopic MP (Integrin, PDB 2K9J [30]), a polytopic α-helix bundle MP (KcsA, PDB 1F6G [31]), and a polytopic β-barrel MP (OmpLA, PDB 1FW2 [32]). Note that proteins were only roughly positioned in a lipid bilayer that is enormously simplified as compared with a biological membrane. Hydrophobic domains are colored green, extramembranous α-helices and β-sheets yellow, and extramembranous loops white. (A, B) Structures of micelle and bilayer are based on molecular dynamics (MD) simulation snapshots adapted from [33]. Color code is gray for carbon, red for oxygen, blue for nitrogen, and orange for phosphorus atoms. (C) Schematic of MP reconstitution, the transfer of MPs from micelles into lipid bilayers, which requires both the addition of (red) lipids as well as the removal of (blue) detergent.

2.1.2 Topology

In the beginning of MP research, a crude classification of α-helical MPs distinguished between peripheral and integral MPs, which penetrate the membrane partially or completely, respectively [34]. Peripheral or monotopic MPs [29] are anchored to one of the lipid bilayer leaflets by amphipathic α-helices, hydrophobic loops, covalently bound membrane lipids, or by electrostatic interactions with lipid headgroups. The vast majority of integral MPs are polytopic and comprise a multispanning bundle of transmembrane (TM) helices, but bitopic MPs that consist of a single helix that spans the entire membrane are also known [35] (Fig. 2.1B). Some decades ago, the classical view of TM helices spanning about 20 hydrophobic amino acid residues and being straight and aligned more or less perpendicular to the membrane plane was considered a common principle. In light of this presumption, MP topology was perceived as the mere number of TM segments and their orientation with respect to the two sides of the lipid bilayer [36, 37]. However, nowadays a more intricate picture of MP topology reaching beyond a simplified geometry of TM segments has emerged [38, 39].

First, the prediction of TM segments on the basis of amino acid hydrophobicity scales is still considered reliable, but substantial deviations between available hydrophobicity scales have been recognized. The discrepancies originate in the methodologies by which these scales have been obtained [40]. Thus, hydrophobicities of amino acids cannot be defined as clear-cut as formerly assumed, and hydropathy predictions may yield differing TM helix lengths. Moreover, the minimum length of TM helices not only depends on their primary structure, but also on lipid bilayer width [41]. Second, the alignment of TM segments is not restricted to straight, canonical α-helices, but TM helices may have bends and kinks within the hydrophobic region of the bilayer that, in the most extreme case, distort the helix to a re-entrant segment that penetrates only halfway through the bilayer and loops back out [42]. Third, on the basis of crystallographic structures many TM helices have been found to be sloped and, in particular, tilting of TM helices has been identified as a possible adaptation to hydrophobic mismatch, that is, a deviation between TM segment length and thickness of the hydrophobic bilayer core [43, 44]. Fourth, the orientation of MPs, which in most cases is determined upon the initial insertion of the polypeptide chain into the membrane by the translocon machinery, may be ambiguous for marginally hydrophobic MPs resulting in dual-topology MPs [45]. Furthermore, in some cases topology has been shown to adapt dynamically to altered membrane properties, for instance in response to changes in lipid composition [46–48] or TM potential [49, 50].

Taken together, MP topologies are highly diverse with multifactorial dependencies on membrane environment properties and protein–lipid interactions in particular. Yet, some generalized principles of topology still apply to most MPs. These include the positive-inside rule, which

proposes a skewed distribution of positively charged residues towards the cytoplasmic compartment [51], the flanking of hydrophobic segments by aromatic residues tyrosin or tryptophan in the lipid–water interface regions [52, 53], or anchorage by charged residues that snorkel towards the lipid headgroups [52, 54].

2.1.3 Reconstitution by Detergent Removal

To introduce recombinantly produced and purified MPs into a well-defined membrane model system, they need to be transferred from detergent micelles into the lipid bilayer, a process which is referred to as MP reconstitution (Fig. 2.1C). The reconstitution of MPs can be achieved by four main technical strategies: (i) organic solvent-mediated reconstitution, (ii) mechanical means, (iii) direct incorporation into preformed liposomes, and (iv) detergent-mediated reconstitution, as reviewed in [55]. Usage of preformed liposomes, in particular, allows reasonable control over vesicle size as the latter are not formed spontaneously. Nevertheless, detergent-mediated reconstitution is most frequently used because of several shortcomings of the other strategies.

In general, detergent-mediated MP reconstitution is achieved by decreasing the concentration of free detergent in a ternary lipid/detergent/protein mixture to a value that is low enough for spontaneous formation of proteoliposomes to occur. For a lipid/detergent system that is described in terms of a pseudo-phase model, this concentration corresponds to a specific phase transition from mixed micelles to mixed bilayers (Section 4). Concentration-dependent phase transitions as such are described by a lipid/detergent phase diagram (Fig. 2.2 A). In many cases, two phase boundaries, the saturation (SAT) boundary and the solubilization (SOL) boundary, subdivide the phase diagram into three ranges, namely, (i) a vesicle range comprising mixed lipid/detergent vesicles only, (ii) a coexistence range that is characterized by the simultaneous presence of mixed micelles and vesicles, and (iii) a micellar range, wherein only mixed micelles exist. The phase boundaries are defined by their slopes, $R_{\mathrm{D}}^{\mathrm{b,SAT}}$, and $R_{\mathrm{D}}^{\mathrm{m,SOL}}$, respectively, and their ordinate intercept, $c_{\mathrm{D}}^{\mathrm{aq}^{\circ}}$. The SAT and SOL phase boundaries mark the saturation of the bilayer (b) phase with detergent (D) and complete solubilization of vesicles below saturation of the micellar (m) phase with lipids, respectively. According to the pseudo-phase model, the concentration of detergent in the aqueous (aq) phase remains constant within the coexistence range. With regard to MP reconstitution, the SOL boundary marks the onset of proteoliposome formation, whereas the last micellar lipid/detergent/protein complexes disintegrate at the SAT boundary. Most often in the course of reconstitutions, the detergent is removed completely or its concentration is at least reduced below the CMC. However, a detergent concentration above the CMC might already be sufficiently low as long as it is below the SAT boundary of the phase diagram.

Different strategies have been established to induce the transition from micelles to vesicles by detergent removal for MP reconstitution. These include (i) dilution, (ii) dialysis, (iii) gel filtration, (iv) adsorption to bio-beads, and (v) complexation by cyclic oligosaccharides called cyclodextrins (CyDs) [56–58]. Reconstitution trajectories obtained with these methods differ (Fig. 2.2 A), and their application is bound to certain limitations.

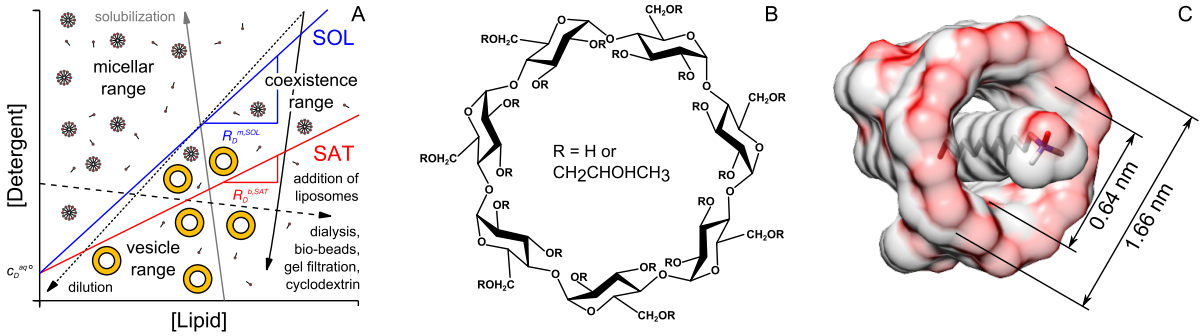

Figure 2.2: Reconstitution trajectories and cyclodextrin.
(A) Generic lipid/detergent phase diagram illustrating different reconstitution trajectories. (SAT) Saturation and (SOL) solubilization boundaries are defined by their slopes, $R_{\mathrm{D}}^{\mathrm{b,SAT}}$ and $R_{\mathrm{D}}^{\mathrm{m,SOL}}$, respectively, and their common ordinate intercept $c_{\mathrm{D}}^{\mathrm{aq}\circ}$. Arrows denote exemplary trajectories (gray arrow) for a solubilization experiment and (black arrows) obtained by different means of reconstitution, including (dotted) dilution, (dashed) addition of liposomes, and (solid) detergent extraction by dialysis, gel filtration, bio-beads, or cyclodextrins. Upon reconstitution, the three pseudophase ranges are traversed, namely the micellar range, the coexistence range, and the vesicle range. (B) Chemical structure of HPβCD. Given a degree of molar substitution of 1, on average, each glucopyranose unit carries one 2-hydroxypropyl moiety and two hydrogen moieties. (C) Molecular model of an inclusion complex of 2-hydroxypropyl-β-cyclodextrin (HPβCD) and LDAO. LDAO is depicted in stick representation, and both molecules are depicted as semitransparent surface representations. Values of inner and outer cavity diameters taken from [59]. Note the polar face formed by the hydroxyl oxygens that mediates solubility in aqueous solvent. Panels A and B adapted from [80] with permission from Elsevier.

Dilution Decreasing the detergent concentration in a ternary lipid/detergent/protein mixture by dilution [60, 61] results in a reconstitution trajectory that follows a straight line going through the origin of the phase diagram (Fig. 2.2 A). The concomitant decrease of the concentrations of all components may result, in particular, in a protein concentration that is insufficient for subsequent assays such as spectroscopic measurements. In such cases, dilution can be followed by centrifugation of the proteoliposomes and resuspension in a small volume of buffer, which prevents exact knowledge on final concentrations. Moreover, dilution needs to be followed by other methods for detergent removal if the detergent is to be removed completely. To avoid excessive dilution, which would be required to reach subsolubilizing concentrations of low-CMC detergents, dilution can be accompanied by the addition of preformed liposomes

[62]. Very similar to direct incorporation into preformed liposomes, this alternative results in a reconstitution trajectory almost parallel to the ordinate of the phase diagram. Nevertheless, dilution with concomitant vesicle addition still goes along with protein dilution and prevents a constant molar lipid/protein ratio (LPR).

Gel Filtration Size exclusion chromatography is not commonly used for detergent removal anymore because it results in incomplete or inhomogeneous incorporation of MPs and heterogeneous size distributions of proteoliposomes [58]. Moreover, a substantial drawback of this method is lipid retention on the column matrix [63] that can only be mitigated by presaturation of the exclusion gel with lipid [64, 65], eliminating control over the final lipid concentration.

Dialysis Dialysis is widely used for detergent extraction as this approach, in contrast with dilution and gel filtration, leaves the concentrations of lipid and protein unchanged [64]. However, dialysis is only applicable to high-CMC detergents because the removal of low-CMC detergents requires long durations for equilibration across the dialysis membrane, which can be critical for less stable MPs.

Bio-Beads The possibly most popular strategy for detergent removal is hydrophobic adsorption onto polystyrene beads known as bio-beads, which have been used for MP reconstitution as well as 2D crystallization with great success [66–68]. Detergent adsorption to bio-beads is independent of the detergent's CMC and bio-beads are in general expected to only remove detergent from a ternary lipid/detergent/protein mixture similar to dialysis. Indeed, the adsorptive capacity of bio-beads for egg yolk phosphatidylcholine is two orders of magnitude lower than for detergents [67]. Nevertheless, for the removal of Triton X-100 and octyl glucoside, a phospholipid loss of 40% and 55%, respectively, has been reported [69]. Thus, unspecific adsorption of phospholipids as well as other lipids by bio-beads cannot be excluded per se. Provided that lipid concentration is not affected, detergent removal by bio-beads leads to a reconstitution trajectory parallel to the ordinate of the phase diagram (Fig. 2.2 A).

For MP reconstitution, it is common practice to ultimately add bio-beads in excess for complete detergent removal. In this case there is no need for an exact knowledge of the amount of beads added. If quantitative detergent removal is desired, the total amount of bead slurry required can be inferred from their binding capacity for the detergent of interest [67]. However, stepwise addition of bio-beads requires rather small amounts of beads that are difficult to deploy reproducibly because of their finite and heterogeneous size and because they must not dry when being used. For example, slow reconstitution of Ca^{2+}-ATPase [70] necessitates amounts as low as 1 mg per addition, which—at a rough estimate—corresponds to four medium-sized beads.

Complexation by CyDs Complexation by CyDs has been introduced as an alternative method for detergent removal to reconstitute [71] and crystallize [72] MPs and to probe protein stability in the absence of a membrane-mimetic system [73]. CyDs are oligosaccharide rings consisting of 6, 7, or 8 α-D-glucopyranoside units denoted α-, β-, and γ-CyD, respectively (Fig. 2.2 B). The conically shaped CyD ring encloses a nonpolar cavity lined by carbon atoms 3 and 5 of the glucopyranoside units that is able to bind small hydrophobic molecules such as cholesterol, or hydrophobic moieties including detergent alkyl chains [74] (Fig. 2.2 C). The hydroxyl groups at the exterior of the ring are responsible for the aqueous solubility of CyDs and CyD inclusion complexes. Solubility as well as ligand specificity of CyDs can be tuned by substituting the hydroxyl groups by other moieties.

Provided that a highly concentrated CyD titrant is used, detergent extraction by addition of CyD is accompanied by a marginal dilution effect and results in a reconstitution trajectory comparable to that of bio-bead-mediated reconstitution (Fig. 2.2 A). Similar to the latter, unspecific binding of lipids needs to be considered for CyDs; however, this issue may be circumvented by using an alternative CyD derivative (as demonstrated later in Section 5.1.2).

A major difference between the methods for detergent depletion outlined above lies in their capability to control the rate of detergent removal, which substantially affects the size and homogeneity of liposomes formed upon reconstitution and may have an influence on the final bilayer topology of integral MPs [75]. For example, it has been reported that rapid dilution gives rise to heterodisperse and unstable vesicle preparations of cholesterol-containing liposomes [60]. Similar results have been observed for the reconstitution of rhodopsin from mixed micelles composed of egg PC and octylglucoside, although vesicle composition was more homogeneous than that resulting from reconstitution by dialysis [76]. For bio-bead-mediated reconstitution of Ca^{2+}-ATPase, two vesicle populations of different LPRs have been observed at a slow rate of detergent removal in the presence of $C_{12}E_8$ but not in the presence of octylglucoside or Triton X-100 [70]. Moreover, membrane incorporation of Ca^{2+}-ATPase occurs asymmetrically in the presence of $C_{12}E_8$ in that 20% of the cytoplasmatic domains face the interior of the vesicles. In light of examples as such, the homogeneity of proteoliposome dispersions and the orientation of incorporated MPs appear not only to depend on the rate of detergent removal but also on lipid bilayer composition, on the nature of the detergent, and on the method of detergent extraction. With regard to vesicle size, however, in general an inverse relationship between the rate of detergent removal and the mean diameter of vesicles obtained can be expected according to the mechanism of vesicle formation proposed by Lasic [77].

For detergent depletion by dilution, a reasonable rate control can be achieved by stepwise addition of the dilution buffer. When using gel filtration for detergent removal, rate control is

hardly possible as very slow flow rates are required in order to obtain an equilibrium between vesicles and mixed micelles and thus to ensure complete protein incorporation [64]. Dialysis allows for limited rate control by adjusting the dialysis volume or by using a continuous flow-through dialysis apparatus [78, 79]. The rate of detergent extraction with bio-beads can be controlled to some extent by stepwise addition of increasing amounts of beads to the reconstitution mixture [67] or by making use of the temperature dependence of detergent adsorption as observed for Triton X-100 [66]. More control over the reconstitution process can be achieved by combining multiple methods for detergent extraction, such as adding bio-beads to the outside of a dialysis bag [69]. In general, however, CyDs allow for the most accurate and precise adjustment of the rate of detergent extraction because they can be dispensed in small volumes and, most importantly, sequester detergent molecules stoichiometrically with defined and adjustable affinities [80, 81].

2.2 Mistic

Expression Tag In this work, the reconstitution and membrane topology of the small α-helical MP Mistic were investigated. The Mistic homolog that was first described [82] originates from *Bacillus subtilis* and comprises 110 amino acid residues (Fig. 2.3) that are arranged in a bundle of four helices (Fig. 2.4 A), as determined by solution nuclear magnetic resonance (NMR) spectroscopy in the presence of *n*-dodecyl-*N,N*-dimethylamine-*N*-oxide (LDAO) [82] and *n*-dodecyl phosphocholine (DPC) micelles [83]. The name of the 13-kDa protein is an acronym for "membrane-integrating sequence for translation of integral MP constructs", which points to its utilization as an N-terminal fusion tag that facilitates the production of prokayrotic as well as eukaryotic MPs by heterologous expression. Enhanced expression levels were achieved for Mistic fusion constructs in *Escherichia coli* and other hosts [10, 84] comprising integral MPs of various functions and origins—including viruses [85, 86]—such as rhodopsins [87–89], histidine kinase receptors [90, 91], G-protein-coupled receptors (GPCRs) [92–94], and other MPs [95–98]. Besides an improved yield of expression, the preservation of functionality could be demonstrated for most of these cargo proteins [86, 89, 91, 93, 98]. Targeting of eukaryotic Mistic fusion constructs to bacterial membranes is based on Mistic's putative ability to autonomously insert into the lipid bilayer [82]. The capability of Mistic of bypassing the Sec translocon machinery that is otherwise required for chaperoning the bilayer incorporation of integral MPs was indirectly presumed as Mistic lacks any recognizable signal sequence.

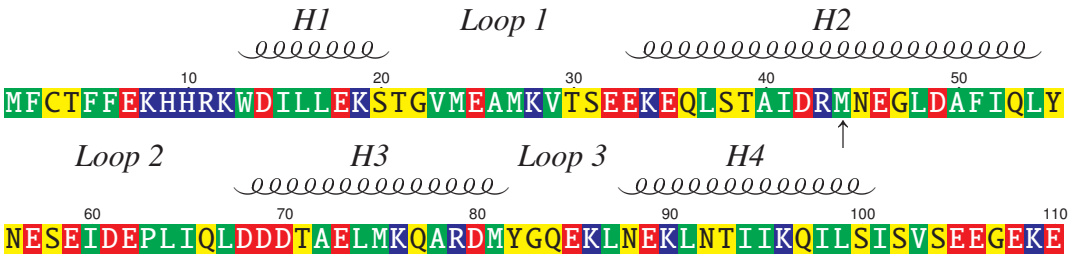

Figure 2.3: Amino acid sequence of Mistic from *B. subtilis*.
The protein consists of four α-helices H1–H4 comprising the amino acid residues 12–21, 32–55, 67–82, and 87–101. Residues are colored according to hydropathy: (Red) Acidic, (blue) basic, (yellow) polar uncharged, (green) hydrophobic nonpolar. The location of the central kink in the second helix H2 is marked by an arrow.

Hydrophilic Surface The membrane association of Mistic appears to conflict with its most outstanding peculiarity, that is, its uncommonly hydrophilic surface (Fig. 2.4 B, C). When expressed in *E. coli*, Mistic appears in both the cytoplasmic and membrane fraction after centrifugal separation [99]. Moreover, short-time atomistic molecular dynamics (MD) simulations suggest that the protein is stable in an aqueous environment [100], and production of a water-soluble variant is indeed possible [101]. At pH 7, Mistic has a net charge of −12, which suggests a positive free energy of insertion and thus, none of the common prediction software that is based on hydrophobicity scales for amino acid residues recognizes Mistic as an MP. In addition, three of the four helices are much shorter than an average TM helix and, thus, suggest that a presumed TM orientation would be accompanied by a substantial negative hydrophobic mismatch (Fig. 2.4 A). However, the short helix lengths have been ascribed to partial unraveling of the termini [82], and membrane association has been corroborated for Mistic *in vitro* [102], *in vivo* [103], and *in silico* with coarse-grained MD simulations [104]. Moreover, the absence of membrane-mimetic systems is known to result in aggregation of the protein [82, 105]. In fact, the very disparities between canonical MPs and Mistic are thought to be pivotal for its success as an expression tag and to render it a perfect candidate for MP unfolding studies. At the same time, the contradiction between hydrophilicity and membrane association has initiated substantial efforts to investigate the fundamental physicochemical properties that govern the interactions between Mistic and different membrane-mimetic systems [73, 82, 98–100, 102].

Conformational Stability The conformational stability of Mistic has been investigated comprehensively by unfolding studies. In general, such experiments have been performed in the presence of a reducing agent because Mistic tends to form disulfide-bridged dimers via its N-terminal cysteine residue *in vitro*. The stability of the monomeric full-length protein solu-

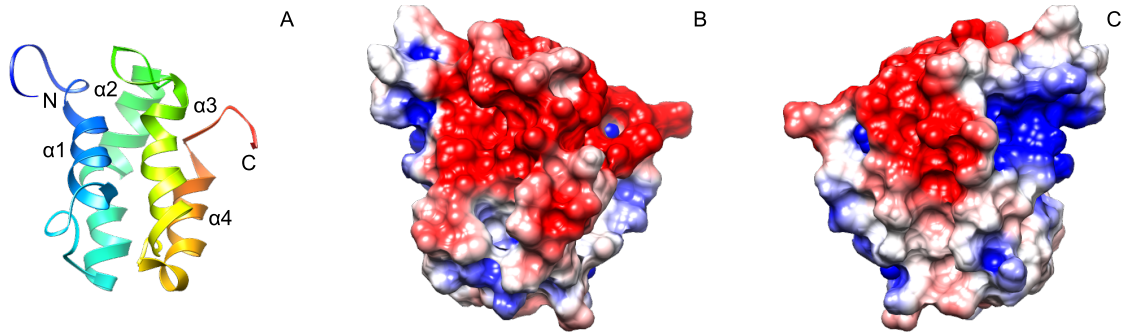

Figure 2.4: Mistic structure and electrostatic surface.
(A) NMR structure of the lowest-energy conformer of Mistic (PDB ID: 1YGM) as determined in detergent micelles composed of LDAO [82]. Helices H1, H3, and H4 of the four-helix bundle are substantially shorter than expected for a polytopic MP. (Blue to red) Rainbow coloring from N-terminus to C-terminus. (B, C) Surface representations of Mistic, (B) oriented as in A and (C) viewed from the opposite side. Mapping of the electrostatic potential is depicted by coloring from (red) negative charges ≤ -100 mV to (blue) positive charges ≥ 100 mV. Neutral surface is colored white. Electrostatic surface potential was calculated using PDB2PQR [106] and APBS [107] with default values, including a solvent relative permittivity of 78.

bilized in detergent micelles has been found to be dependent on the alkyl chain length of the detergent, but even more so on headgroup electrostatics. For a homologous series of nonionic maltoside detergents, longer detergent chains resulted in better shielding of Mistic from the aqueous solvent [73, 105], and, similarly, a relationship between chain length and solubilization yield was found for a homologous series of zwitterionic phosphocholine detergents [85]. In contrast with most solubilization trials for MPs, zwitterionic detergents were most suitable for stabilizing Mistic and extracting Mistic fusion constructs, whereas the use of most non-ionic detergents proved unsuccessful [87]. In the presence of most detergents, complete and reversible unfolding of Mistic was possible by addition of denaturants, whereby the nonionic denaturant urea was found to be less effective in destabilizing Mistic than the ionic denaturant guanidine hydrochloride [101]. When Mistic was solubilized in the zwitterionic detergent LDAO, denaturants induced only partial unfolding, which did not obey a two-state equilibrium [108]. The conformational stability of Mistic in LDAO was also studied by atomistic MD simulations, which suggested partial unfolding that is accompanied by helix H4 drifting away from a structural core comprising the other helices [100].

Helical Dissection The role of individual helices in the interaction with detergents and lipids was probed in more detail by different approaches that resulted in controversial observations. In general, the four helices of Mistic show no apparent differences in hydrophobicity or charge distribution among each other. In a "divide-and-conquer"-approach, peptide fragments

corresponding to the four α-helices were found to be water-soluble but unstructured, and assumed α-helical secondary structure upon micelle partitioning induced by the addition of detergent [109]. Bilayer partitioning was observed for helical fragments corresponding to helices H1, H2, and H4, but not for the one corresponding to helix H3. In contrast, helix H3 of full-length Mistic had shown the most pronounced interactions with detergent headgroups of LDAO micelles [108]. Importantly, a correlation between the ability of the helical fragments to assist in membrane association and an increase in expression levels was not found. N-terminal fusion constructs including truncated Mistic fragments and the human Y4 GPCR resulted in increased expression yield for all helical fragments except the one of the first helix [109]. It was thus concluded that the effect of the helical segments on overexpression of fusion constructs depends on their mRNA sequence rather than on physicochemical properties on the protein level.

Other Homologs The inability of the N-terminal helix to promote the overexpression of fusion constructs goes in line with the finding that other Mistic homologs lack the corresponding sequence spanning the N-terminal 26 amino acid residues and, hence, only consist of 84 amino acid residues [110]. To date, 20 Mistic homologs have been identified with sequence identities ranging from 34% to 99% [109] (for a phylogenetic tree, see supplementary information of [109]). Only four of these posses the sequence for helix H1 (those from *B. subtilis, B. vallismortis, S. pasteurii*, and *S. aidigensis*). Seven homologs stem from genera other than *Bacillus* [109]. Interestingly, in aqueous solution the shorter forms of Mistic that were investigated afforded significant solubility, which was even increased by a mutation of a methionine residue corresponding to M75 of the full-length protein. Mutation of this residue had already been found to tremendously reduce membrane association of the full-length protein, giving rise to cytoplasmic localization [82]. Moreover, the truncated forms of Mistic formed multimers consisting of four or more subunits in solution [99], and fibril formation was observed for some of these homologs at high concentrations. Alongside these findings it was speculated that polymerization might assist membrane incorporation of the soluble homologs by masking the charged surface of the monomers.

Biological Function The genetic organization around the gene encoding for Mistic, *mstX*, appears to be highly diverse among some of the Mistic homologs, which renders a common function of Mistic unlikely. A gene encoding for a putative potassium ion channel called YugO, *yugO*, is located directly downstream of *mstX*, and both genes overlap with a frame shift of one base pair. Thus, the two genes are expected to be expressed as two seperate polypeptide chains. Close to the overlapping region, a highly conserved Shine–Dalgarno sequence has been

identified, which is assumed to be required for downstream translation of *yugO* [109]. However, in five of the 20 species, *mstX* and *yugO* are not part of the same operon.

Nevertheless, in *B. subtilis*, both Mistic and YugO have been found to play an essential role in derepression of biofilm formation [111]. More precisely, the proteins together partake in a positive autoregulatory feedback loop that promotes biofilm assembly in a subpopulation of cells and is mediated by a pathway involving potassium ion efflux, activation of the kinase KinC, and phosphorylation of the sporulation and biofilm regulatory factor Spo0A. This is followed by activation of the antirepressor SinI, which finally alleviates repression of *mstX*, *yugO*, and genes for biofilm components by the master regulator for biofilm formation, SinR.

More strikingly, at the time of completing this thesis, YugO has been identified as the first example of a bacterial ion channel that appears to mediate long-range electrical communication within bacterial communities reminiscent of neuronal signalling [112]. Initiated by glutamate deprivation as a metabolic trigger, the release of intracellular potassium ions leads to a depolarization of neighboring cells, which, reinforced by the autoregulatory feedback loop, results in a spatially propagating wave of potassium ions throughout the biofilm. The oscillating potassium ion waves ultimately coordinate glutamate uptake that cells in the interior and peripheral regions of the biofilm compete for.

What still remains unknown is Mistic's mode of function and relation to YugO. As Mistic is thought to incorporate into the membrane autonomously, the initial and most obvious assumption made [82] was that Mistic might directly chaperon the membrane insertion of YugO, which, however, is not supported by the separate expression of the proteins and, even more so, assuming a translocon-dependent membrane insertion of YugO. Future research will hopefully elucidate if Mistic positively regulates YugO and, if so, whether direct interactions are involved.

2.3 Goals

As outlined above, to date there is great debate on how Mistic is able to autonomously associate with a lipid bilayer despite its hydrophilic surface. In a previous study [102], the membrane association of Mistic has been investigated by using a cell-free production system. The effect of different lipids on Misitc's stability was assessed by production yield and dimerization as a marker for protein folding quality. However, the components required for cell-free translation impede most downstream studies that would allow for elucidation of the protein's mode of interaction with the membrane, such as spectroscopic experiments, which calls for a conventional reconstitution protocol starting from the detergent-solubilized protein.

Thus, the main goals of this thesis were twofold. First, a quantitative protocol for the

reconstitution of Mistic in a lipid bilayer was to be established. Second, on the basis of this approach, the topology of the incorporated protein was to be investigated making use of, in particular, oriented circular dichroism (OCD) spectroscopy and fluorescence spectroscopy to obtain information on the rotational and translational orientation, respectively, of Mistic within the lipid bilayer. For reconstitution, focus was directed at the transfer of Mistic from LDAO micelles into POPC vesicles because LDAO has been demonstrated to afford optimal stability of Mistic as compared with other detergents [105], and vesicles composed of phosphatidylcholine lipids fared best in terms of both production and suppression of dimer formation of Mistic in the cell-free production system [102].

3 Materials and Methods

3.1 Chemicals and Enzymes

All chemicals and enzymes used in this thesis were purchased in highest possible purity. Acrylamide, agar-agar, benzamidine hydrochloride, $CaCl_2$, carbenicillin disodium salt, Coomassie brilliant blue G250, 1,4-dithio-DL-threitol (DTT), ethanol (EtOH), ethylenediamine tetraacetic acid (EDTA), glycerol, guanidine hydrochloride, HCl, isopropyl-β-thiogalactopyranoside (IPTG), imidazole, kanamycin sulfate, lysogeny broth (LB) medium, β-Mercaptoethanol, NaOH, sodium dihydrogen phosphate dihydrate ($NaH_2PO_4 \cdot 2H_2O$), tris(hydroxymethyl)-aminomethane (Tris), α-[4-(1,1,3,3-tetramethylbutyl)phenyl]-ω-hydroxy-poly(oxy-1,2-ethanediyl) (Triton X-100), and yeast extract were from Carl Roth (Karlsruhe, Germany). NaCl (AnalaR Normapure) was purchased from VWR International (Darmstadt, Germany), whereas NaF was purchased from Merck (Darmstadt, Germany). Sodium phosphate dibasic (Na_2HPO_4), *N*-acetyl-L-tryptophanamide (NATA), *n*-dodecyl-*N,N*-dimethylamine-*N*-oxide (LDAO), randomly methylated β-cyclodextrin (MβCD), and 2-hydroxypropyl-β-cyclodextrin (HPβCD) with an average molar degree of substitution of 1.0 were from Sigma-Aldrich (Steinheim, Germany). DL-tryptophan octyl ester (TOE) hydrochloride was purchased from Santa Cruz Biotechnology (Heidelberg, Germany). Benzonase and EDTA-free Complete were from Roche Applied Sciences (Penzberg, Germany). *n*-Octyl-β-D-maltopyranoside (OM), *n*-decyl-β-D-maltopyranoside (DM), and *n*-dodecyl-β-D-maltopyranoside (DDM) were purchased from Glycon Biochemicals (Luckenwalde, Germany). L-cysteine hydrochloride and L-cystine were from Applichem (Darmstadt, Germany). 1-palmitoyl-2-oleoyl-*sn*-glycero-3-phosphocholine (POPC) was obtained from Lipoid (Ludwigshafen, Germany), and 1,2-Dilauroyl-*sn*-glycero-3-phosphocholine (DLPC) and brominated lipids 1-palmitoyl-2-(*x,y*-dibromo)stearoyl-*sn*-glycero-3-phosphocholine (*x*-*y*BrPC, with *x*-*y* = 6-7, 9-10, and 11-12) were from Avanti Polar Lipids (Alabaster, AL, USA). Bio-Beads SM2 (20-50 mesh) were purchased from Bio-Rad (Hercules, United States). NaN_3 and citric acid monohydrate were obtained from the chemical supply of the University of Kaiserslautern.

If not otherwise stated, experiments were generally performed at 25°C using a default buffer that contained 50 mM Tris at pH 7.4 and 50 mM NaCl. All solutions were prepared using ultrapure water (resistivity >18 MΩ·cm). In general, samples containing Mistic were supplemented with 5 mM DTT to prevent dimerization of the protein.

3.2 Preparative Methods

3.2.1 Production and Purification of Enterokinase

Enterokinase (EK) protease from *Bos taurus* used for tag removal of purified Mistic was produced according to [113] with minor modifications. The plasmid pET-15b-EK_C122S_His5 was kindly provided by Wolfgang Skala. In brief, transformation, expression, and cell harvest were performed similar as described for Mistic in Section 3.2.2. After solubilization of inclusion bodies, refolding was carried out by diluting ∼53 mL of the protein solution dropwise into 5 L sterile filtrated refolding buffer with a syringe pump (LA-100, Landgraf HLL, Langenhagen, Germany) at 33.3 µL/min. After filtration with filter paper, the refolding solution was concentrated on an Äkta Purifier System (GE Healthcare, Uppsala, Sweden) by tangential flow filtration with a Connect Minimate TFF Capsule with a molecular weight cut-off (MWCO) of 10 kDa (Pall, Dreieich, Germany) to a final volume of ∼400 mL. After dialysis of the concentrate against storage buffer and removal of precipitates by centrifugation, autoactivation of EK was induced with NaN_3. Purification of EK was performed with a 5-mL Benzamidine HiTrap FF column (GE Healthcare) at a flowrate of 2.5 mL/min. After pooling all eluates and concentrating to 80 µg/mL with Amicon Ultra-15 Centrifugal Filter Units with a MWCO of 10 kDa (Millipore, Billerica, USA), aliquots of the EK solution were flash-frozen in liquid nitrogen and stored at −80°C.

3.2.2 Production of Mistic

The *mstX* gene was available as a fusion construct with an N-terminal hexahistidine-streptavidine tag, $(His)_6$-S-tag, cleavable with EK (cleavage site DDDDK↓). This construct was inserted into a pET-30 EK/LIC expression vector (Merck, Darmstadt, Germany), which contained a strong T7lac promoter, an optimized ribosome binding site, and a kanamycin (kan) resistance sequence that allows for the selection of positive transformants.

Transformation Mistic was produced according to [114] with minor modifications. Briefly, 25 µL chemically competent BL21(DE3) *E. coli* cells (Merck) were transformed with 1 µL plasmid DNA by 5-min incubation on ice followed by 30-s incubation at 42°C in a block heater (NeoBlock I, NeoLab, Heidelberg, Germany) and 2-min incubation on ice. After addition of 250 µL LB medium and gentle mixing, the transformed cells were incubated for 60 min at 37°C with agitation (1400 rpm; Thermomixer compact, Eppendorf, Hamburg, Germany). Afterwards,

80 µL of the cells were plated on a preheated 1.5% LB/kan agar plate and incubated at 37°C in a Minitron incubator (Infors HT, Ingolstadt, Germany) overnight.

Expression A volume of 50 mL of LB/kan medium was inocculated with an overnight colony and grown overnight with agitation (Minitron incubator, 180 rpm). For large scale expression, 4×1-L LB/kan in 2-L flasks were inocculated with 12 mL overnight culture each and the cells grown for ∼3 h at 120 rpm to an optical density (OD) of $OD_{600\,nm}$ = 0.8-1. The $OD_{600\,nm}$ was determined in a disposable polystyrene cell with an optical path length of 1 cm (Sarstedt, Nümbrecht, Germany) with a Lambda 40 spectrophotometer (Perkin-Elmer, Rodgau, Germany). Expression was induced with 0.5 mM IPTG at 18°C for 6 h at 120 rpm (Minitron incubator) and stopped afterwards by decreasing the temperature to 4°C and stopping agitation.

Cell Harvest Cells were transferred to centrifuge tubes and spun down (Beckman JA-10, 7500 rpm/9954 *g*, 15 min, 4°C). After resuspension of the pellets in 154 mM NaCl, cells were spun down again, weighed, and stored at −80°C.

3.2.3 Purification of Mistic

Purification of Mistic was performed similar to the protocols in [101] and [105] with minor modifications. All buffers used for Mistic purification contained 50 mM Tris, 50 mM NaCl, and 12 mM LDAO (prepared from ∼30% LDAO solution in H_2O) if not otherwise stated.

Cell Breakage Cell breakage was performed to recover Mistic from cell biomass. To this end, pellets were thawed on ice and resuspended in breakage buffer (pH 7.4, 40 mM imidazole, 4 M urea, 2 mM $MgCl_2$) to a final concentration of 10% (*w/v*) wet biomass. Before use, breakage buffer was freshly supplemented with 0.01% (*v/v*) nuclease (benzonase, 25 U/µL) and 4% (*v/v*) protease inhibitor (Complete EDTA-free, 1 tablet per 2 mL stock). Cell disruption was carried out with a tip sonicator (Sonifier 250, Ultrasonics, Danbury, USA) in 4 cycles of 10 min sonication and 10 min pause each at an amplitude of 40%. After cell lysis, cell debris was removed by centrifugation (Beckman JA-17, 10000 rpm/13766 *g*, 60 min, 10°C). The supernatant was filtered through a polyvinylidene fluoride membrane with a pore size of 0.45 nm (Carl Roth, Karlsruhe, Germany) and stored at 8°C until further use.

Affinity Chromatography His-tagged Mistic was seperated from other proteins by immobilized-metal affnity chromatography (IMAC) with a 5-mL HisTrap HP column (GE Healthcare) on an Äkta Purifier System (GE Healthcare). After equilibration of the column with buffer (pH 7.4) supplemented with 4 M urea and 40 mM imidazole to prevent unspecific binding,

the supernatant from cell breakage was applied to the column at a flowrate of 1 mL/min, and His-tagged Mistic was eluted with 50 mL elution buffer (pH 7.4, 1 M imidazole). The eluate was then dialyzed at room temperature (RT) overnight against a 300-fold buffer volume (pH 7.4) using a MWCO of 6-8 kDa. Precipitates were removed by centrifugation (Eppendorf F-35-6-30, 7000 rpm/5752 *g*, 10 min, 10°C) and the dialyzed eluate stored at 4°C until further use.

EK Digestion After IMAC, EK digestion was performed to cleave the His-tag from purified Mistic. To this end, the protein concentration was measured spectrophotometrically (Section 3.3.1.1) and reduced to 1 mg/mL if applicable by dilution with dialysis buffer. The solution was freshly supplemented with 5 mM DTT and 4 mM $CaCl_2$ and digested with EK at a molar EK/Mistic ratio of 10000 at RT for 23 h. EK digestion was stopped by addition of 4% (*v/v*) protease inhibitor (Complete EDTA-free) followed by 10-min incubation, and the pH of the solution was adjusted to 8.0.

Concentration The protein solution was concentrated by anion exchange (AIX) chromatography on a 20-mL self-packed diethylaminoethanol (DEAE) HiScale 16 column (GE Healthcare) at 8°C. The column was equilibrated with AIX binding buffer (pH 8.0 at RT) before loading the digested protein on the column with a flowrate of 3 mL/min. The protein was eluted in two steps of 100 mL 25% and 40 mL 100% AIX elution buffer (pH 8.0 at RT, 1 M NaCl) and fractions containing protein were pooled.

Reverse Affinity Chromatography Residual His-tagged Mistic, cleaved tag, and EK was seperated from digested Mistic by reverse IMAC. To this end, the eluate from AIX chromatography was applied to a 5-mL HisTrap HP column pre-equilibrated with buffer at 5 mL/min and the flowthrough containing tag-free Mistic was collected during loading. Residual tagged protein, tag, and EK were eluted with 25 mL elution buffer. The collected flowthrough was dialyzed at RT overnight against a 100-fold buffer volume (pH 7.4) using a MWCO of 6-8 kDa. Purified Mistic was frozen in liquid nitrogen and stored at −80°C until further use.

Detergent Exchange AIX chromatography followed by a desalting step was used to concentrate the protein solution after purification and to exchange the detergent. To this end, the protein solution was applied to a 1-mL HiTrap Q HP column (GE Healthcare) equilibrated at a flowrate of 1 mL/min with 5 mL buffer containing 50 mM Tris pH 8.0 at RT, 50 mM NaCl, and the detergent of choice at the target concentration. To obtain Mistic solubilized in LDAO, detergent exchange was performed using 6 mM high-purity LDAO (≥99.0% by non-aqueous titration). After washing the column with 10 mL detergent exchange buffer, the protein was

eluted with the same buffer containing 1 M NaCl. The eluate was collected in 0.5-mL fractions, and the protein concentration of each fraction was determined spectrophotometrically (Section 3.3.1.1). To adjust the salt concentration of the eluate, up to five fractions of highest protein concentration were pooled and applied to a PD-10 desalting SEC column (GE Healthcare) according to the manufacturer's instructions. The storage buffer used for elution contained 50 mM Tris pH 7.4, 50 mM NaCl, and the final detergent concentration. After determination of the protein concentration of the eluate, aliquots of the protein solution were flash-frozen in liquid nitrogen and stored at −80°C.

3.2.4 Preparation of Lipid Vesicles

For solubilization and reconstitution experiments (Section 3.3.2.4) as well as Mistic reconstitution by liposome addition, large unilamellar vesicles (LUVs) were prepared by extrusion [115]. First, solid lipid was allowed to thermally equilibrate to RT, weighed, suspended in buffer, and vortexed vigorously for at least 10 min to generate multilamellar vesicles (MLVs). The MLV suspension was then extruded in 35 steps through two stacked polycarbonate filters with a pore diameter of 100 nm using a LiposoFast extruder (Avestin, Ottawa, Canada). An odd number of passes was applied to avoid contamination of the LUV suspension by MLVs which might not have passed through the filters. Freshly prepared liposome stocks were layered with N_2 and stored at 4°C until use.

For release experiments (Section 3.3.2.1), lipid vesicles preloaded with detergent were prepared. To this end, weighed lipid was supplemented with detergent stock and buffer, and after vortexing, the dispersion was subjected to five freeze–thaw cycles (liquid N_2/40°C) before extrusion.

For depth-dependent fluorescence quenching (DDFQ) experiments (Section 3.3.4.2), lipid mixtures were prepared from chloroform stocks. Aliquots of stocks were mixed to the desired molar ratio and the solvent was evaporated under reduced pressure using a rotary evaporator Rotavapor R-210 (Büchi, Flawil, Switzerland). To remove any remaining traces of solvent, the phospholipid film was put in a vacuum desiccator overnight. After resuspension of the dried film in buffer by vortexing, the dispersion was subjected to five freeze–thaw cycles (liquid N_2/40°C). Thereafter, vesicles were prepared by extrusion as described above.

3.2.5 Reconstitution of Mistic

Reconstitutions of Mistic by cyclodextrin (CyD)-mediated detergent extraction were performed either (i) manually by adding the HPβCD titrant stepwise to the reconstitution mixture, (ii)

automatically with an isothermal titration microcalorimeter for calorimetric monitoring (Section 3.3.2.5), or (iii) automatically with a titrator (Section 3.4) for monitoring by dynamic light scattering (DLS) or fluorescence spectroscopy, or without monitoring. While constant stirring of the sample was maintained by the injection syringe in the case of ITC and by a magnetic stirrer for unmonitored reconstitutions and reconstitutions monitored by fluorescence spectroscopy, the DLS instrument used was not equipped with a magnetic stirrer. Thus, for automatic reconstitutions monitored by DLS, mixing of the sample was realized by repeated withdrawing and dispensing of the sample by one of the titrator syringes. This resulted in some retention of a sample fraction in the mixing tubing, which was, however, smaller than 5% of the total sample volume.

Reconstitutions were performed at 25°C with instruments providing temperature control and at RT when performed automatically without monitoring. To allow for sufficient equilibration after each injection during reconstitutions monitored by ITC, time spacings between injections were chosen in that the overall duration per reconstitution was 3.3 h. For reconstitutions monitored by DLS and fluorescence spectroscopy, data acquisition settings required durations of 2.5 and 5 h, respectively. For the sake of consistency, manual reconstitutions were also performed at a slow rate of detergent extraction within 2.5 h.

Mistic reconstitutions monitored by ITC were followed by circular dichroism (CD) measurements. Therefore, a relatively high protein concentration of 70 μM was used to ensure a decent spectroscopic signal at the short pathlength used. For the series of different molar lipid/protein ratios (LPRs), an intermediate concentration of 24 μM Mistic was used as a compromise between signal/noise ratio and increased vesicle-induced light scattering at higher LPRs. For reconstitutions monitored by DLS and fluorescence spectroscopy, a lower Mistic concentration of 8 μM was used to keep the vesicle concentration at the given LPR low.

3.3 Analytical Methods

3.3.1 UV/Vis Spectroscopy and Refractometry

3.3.1.1 Protein Concentrations and Extinction Coefficients Concentrations of protein solutions were determined spectrophotometrically with a NanoDrop 1000 (peqlab Biotechnolgy, Erlangen, Germany). After measuring the buffer blank, the UV absorbance at 280 nm was measured in triplicate and the average was used to calculate the protein concentration according to Lambert-Beer's law using the theoretical extinction coefficient of Mistic at 280 nm, $\varepsilon_{280\,\mathrm{nm}}$ = 8480 M^{-1} cm^{-1}, or EK, $\varepsilon_{280\,\mathrm{nm}}$ = 53900 M^{-1} cm^{-1}, and the nominal molecular weight of either

tagged Mistic (17.6 kDa), tag-free Mistic (12.8 kDa), or EK (27.0 kDa) as obtained with the ExPASy server [116].

To obtain extinction coefficients for DL-tryptophan octyl ester (TOE) and Mistic at an extinction wavelength of λ_{ex} = 295 nm, absorbances of five samples were measured with a 1-cm quartz glass cuvette at 25°C on a Jasco V-630 spectrophotometer (Jasco, Tokyo, Japan). Measurement parameters were set to a bandwidth of 1.5 nm and five-fold accumulation. Samples contained 2, 4, 6, 8, and 10 µM TOE or Mistic in buffer (50 mM Tris pH 7.4, 50 mM NaCl) in the presence of 6 mM LDAO and 5 mM DTT. After subtraction of the buffer blank that also contained LDAO and DTT, extinction coefficients were retrieved by a linear least-squares fit to plots of absorbance versus concentration.

3.3.1.2 Bio-Bead Binding Capacity The adsorptive capacity of bio-beads for LDAO was determined based on the time courses of detergent removal by different amounts of beads at known initial LDAO concentration similar as in [66–68, 117]. First, bio-beads were prepared in bulk prior to use by washing two times in methanol followed by three washing steps in ultrapure water. Each washing step was performed for 30 min at gentle agitation and followed by decantation and addition of fresh methanol or water. Bio-beads were stored in water at 4°C. In time-course measurements, the LDAO concentrations were inferred from the refractive index of the samples. To this end, the differential index of refraction, dn/dc, for LDAO in buffer was determined beforehand at 20°C for LDAO concentrations of up to 20 mM on an Abbemat 500 digital refractometer (Anton Paar, Ostfildern, Germany).

For time-course measurements, 12, 23, 46, and 86 mg wet beads were weighed. Beads were not blotted to exclude the possibility of excessive drying, which would affect binding capacity. Instead, dry weight was determined to be 45 ± 5% of wet weight on the basis of the weight difference for seperate batches of beads before and after blotting. The different amounts of beads were each added to 1 mL of 15 mM LDAO in buffer and gently stirred at RT. The LDAO concentration was determined refractometrically before addition (t = 0) and 5, 10, 15, 30 min, and 1, 2, 3, and 4 h after bio-bead addition. Analysis of time-course measurements was performed by applying a nonlinear least-squares fit (NLSF) on the basis of a negative exponential function (Eq. 3.1) to determine plateau values.

$$c_D(t) = (c_D^0 - c_D^{end})e^{-\tau t} + c_D^{end} \tag{3.1}$$

where $c_D(t)$ denotes the time-dependent LDAO concentration, c_D^0 the initial LDAO concentration, c_D^{end} the plateau concentration, and τ the rate of detergent removal. The adsorption capacity of bio-beads for LDAO was procured from the slope of a linear least-squares fit to plateau

values plotted against the amount of bio-beads added, assuming that the binding capacity is constant at low bead/detergent ratios.

3.3.2 Isothermal Titration Calorimetry (ITC)

In Section 4, a quantitative model for reconstitution by CyD-mediated detergent extraction is devised that predicts the supramolecular state(s) present in a complex reconstitution mixture for given concentrations of CyD, lipid, and detergent. The model comprises a set of linked equilibria among bilayer, micellar, and aqueous phases that are characterized in terms of the dissociation constant of the CyD/detergent inclusion complex, the detergent's critical micelle concentration (CMC), and partition coefficients reflecting the transfer of detergent and lipid between bilayer and micellar phases. All of these parameters were conveniently obtained by isothermal titration calorimetry (ITC), which provides unrivaled sensitivity, resolution, and reproducibility and is attracting increased attention in membrane-protein research in particular [118]. The components used for CyD-mediated reconstitution of Mistic included the CyD HPβCD, the phospholipid POPC, and the detergent LDAO. Thus, the calorimetric titrations required to derive the parameters for the quantitative model included a HPβCD/LDAO binding experiment, LDAO demicellization, and multiple solubilization and reconstitution experiments, which furnished the POPC/LDAO phase diagram in the absence of HPβCD.

ITC experiments were performed on either a VP-ITC, an iTC_{200}, or an Auto-iTC_{200} (all from Malvern Instruments, Worcestershire, UK). All measurements were carried out at 25°C using default buffer containing 50 mM Tris pH 7.4, 50 mM NaCl. Degassing of samples was refrained from because of the modest temperature used and to prevent foaming of samples containing detergent or CyD. For data evaluation, raw thermograms of all calorimetric experiments were subjected to automated baseline assignment by singular value decomposition and peak integration with NITPIC [119]. In general, the first injection was always excluded for analysis because mounting of the syringe and sample equilibration before the actual titration are accompanied by a loss of titrant.

3.3.2.1 Uptake and Release Assay To assess the capability of LDAO to translocate between the two leaflets of a lipid bilayer, uptake and release experiments were performed on a VP-ITC. For the uptake experiment, 20 mM POPC in the form of LUVs was titrated to 100 μM LDAO. For the release experiment, 20 mM POPC vesicles preloaded (see Section 3.2.4) with 2 mM LDAO were titrated into buffer. For both uptake and release, the injection volume was set to 5 μL, the time spacing to 300 s, the stirrer speed to 310 rpm, the filter period to 2 s, and

the reference power to 75 μJ/s. The lipid accessibility factor γ was deduced from a NLSF to the isotherms as described in Section 4.2.

3.3.2.2 Binding Experiments The dissociation constant of the HPβCD/LDAO complex was determined calorimetrically with a VP-ITC. In the binding experiment, 8 mM HPβCD was titrated into 1 mM LDAO with an injection volume of 5 μL, a time spacing of 300 s, a stirrer speed of 310 rpm, a filter period of 2 s, and a reference power of 75 μJ/s. A NLSF was applied to the binding isotherm in SEDPHAT [120] according to a one-site binding model as described in [121] to determine the dissociation constant $K_{\mathrm{D}}^{\mathrm{i/aq}}$, which is defined as in Section 4.3.

3.3.2.3 Demicellization The CMC of LDAO was determined by injecting 25 mM LDAO into buffer with a VP-ITC. The injection volume was set to 5 μL, the time spacing to 900 s, the stirrer speed to 310 rpm, the filter period to 2 s, and the reference power to 75 μJ/s. The CMC was extracted from the demicellization isotherm by a two-step analysis as explained in Section 4.4. In brief, estimates of fitting parameters were first deduced from the first derivative of the demicellization isotherm. In the second step, these estimates were used as fitting parameters for a generic sigmoidal fit to the isotherm.

3.3.2.4 Reconstitution and Solubilization The POPC/LDAO phase diagram was obtained from a number of solubilization and reconstitution experiments at different initial POPC and LDAO concentrations, respectively. For solubilization, 30 mM, 65.5 mM, 85 mM, or 131 mM LDAO was titrated to 1 mM, 3 mM, 4.5 mM, or 6 mM POPC vesicles, respectively. For reconstitution, 15 mM, 15 mM, 35 mM, or 40 mM POPC vesicles were titrated to 4 mM, 6 mM, 9 mM, or 13 mM LDAO, respectively. The injection volume was set to 4 μL, whereas other measurement parameters were set as for the demicellization experiment.

The cross points of saturation (SAT) and solubilization (SOL) boundaries reached during solubilization and reconstitution experiments were extracted by calculation of the numeric first derivatives of the isotherms. Local minima and maxima of the first derivative within the transition regions of the isotherms correspond to the cross points of SAT and SOL boundaries, respectively [122]. The phase diagram was furnished by plotting the LDAO concentrations at these cross points versus the respective POPC concentrations and applying two global linear least-squares fits according to Eqs. 4.20 and 4.21 comprising the phase-boundary slopes as local fitting parameters and a shared ordinate intercept, $c_{\mathrm{D}}^{\mathrm{aq}^{\circ}}$, as as a global fitting parameter. The latter was linked to $R_{\mathrm{D}}^{\mathrm{m,SOL}}$ through Eq. 4.30 by taking into account the CMC of LDAO to reduce the number of fitting parameters and thus narrow down the error margins of the

remaining parameters. Error margins for the phase boundaries were estimated by fitting data from either solubilization or reconstitution experiments individually.

3.3.2.5 CyD-mediated Reconstitutions Reconstitutions driven by CyD-mediated detergent removal were monitored on different instruments with different measurement parameters.

The reconstitution in the absence of Mistic shown in Section 5.3 was performed on a VP-ITC using an injection volume of 4 μL, a time spacing of 900 s, a stirrer speed of 310 rpm, a filter period of 2 s, and a reference power of 75 μJ/s. A titrant containing 75 mM HPβCD was titrated into mixed micelles composed of 3 mM POPC and 12 mM LDAO in a series of 60 injections.

The measurement in the presence of Mistic was performed on an iTC_{200}. The injection volume was set to 0.4 μL, the time spacing to 120 s, the stirrer speed to 1000 rpm, the filter period to 5 s, and the reference power to 25 μJ/s. A titrant containing 149 mM HPβCD was titrated into a ternary mixture of 70 μM Mistic, 14 mM POPC, and 40 mM LDAO in the presence of 5 mM DTT in a series of 100 injections.

The reconstitutions at different LPRs shown in Section 5.4 were monitored on an Auto-iTC_{200} using an injection volume of 0.4 μL, a time spacing of 120 s, a stirrer speed of 750 rpm, a filter period of 2 s, and a reference power of 21 μJ/s. The titrations comprised 100 injections each and concentrations were chosen as given in Table 3.1.

Table 3.1: Concentrations used in Mistic reconstitutions at different LPRs

	Cell			Syringe
LPR	[LDAO] above $R_D^{m,SOL}$ (mM)	[LDAO] (mM)	[POPC] (mM)	[HPβCD] (mM)
100	2.94	10.63	2.40	66.6
130	3.83	13.40	3.12	85.3
160	4.71	16.17	3.84	104.0
190	5.59	18.93	4.56	122.6
220	6.48	21.70	5.28	141.3
250	7.36	24.47	6.00	160.0
280	8.24	27.24	6.72	178.7
310	9.13	30.00	7.44	197.4

All cell samples also contained 24 μM Mistic and 6 mM DTT.

3.3.3 Circular Dichroism (CD) Spectroscopy

The secondary structure of Mistic in micelles or lipid bilayers was assessed by circular dichroism (CD) spectroscopy on a Chirascan-plus spectropolarimeter (Applied Photophysics, Leatherhead,

UK) equipped with a 150-W Xenon arc lamp and a large-area avalanche photodiode detector (Advanced Photonix, Ann Arbor, USA). A quartz glass cuvette with a pathlength of 0.2 mm (msscientific Chromatographie-Handel GmbH, Berlin, Germany) was used to reduce differential light scattering effects due to vesicles. For a 1 mm path length, undistorted spectra for samples containing 5 mM LUVs are expected for the spectral region above 200 nm [123]. Likewise, differential scattering is reduced even more for smaller path lengths. Standard measurement parameters included a step size of 1 nm, a bandwidth of 1 nm, and a digital integration time (DIT) of 1 s. Data analysis included averaging of five repeat spectra, subtraction of spectra obtained for control samples in the absence of protein, zeroing by an offset taken from the average between 270 and 280 nm, and conversion from ellipticity values (given in mdeg) to mean residue molar ellipticity values (θ_{MRW}, given in deg cm^2 dmol^{-1}).

3.3.3.1 Denaturant-Induced Unfolding Equilibrium unfolding of reconstituted Mistic was performed by stepwise addition of urea. Urea stock solutions were prepared in ultrapure water and deionized for 1 h with ∼10% (*w/w*) Amberlite IRN-150L mixed bead resin (GE Healthcare). Concentrations of urea stock solutions were determined on the basis of their refractive indices [124] using an Abbemat 500 digital refractometer (Anton Paar). Sterile filtrated stock solutions were stored at −80°C. For titrations, urea stocks were diluted with 20× buffer to obtain urea stocks with final concentrations of 50 mM Tris, 50 mM NaCl, pH 7.4.

Titrand and titrant were obtained by diluting Mistic samples after CyD-mediated reconstitution 1:6 into buffer and urea stock, respectively, with final concentrations of 1.3 mM POPC, 3.7 mM LDAO, 6.3 mM HPβCD, and 6.5 µM Mistic. Titration was performed in 30 steps of 0.2 M urea each to increase urea concentration to up to 5.8 M. Three replicate urea titrations were carried out at 25°C with a titrator (Section 3.4) and constant stirring of the sample in a 10 × 4 mm cuvette (pathlength 4 mm, Hellma Analytics, Müllheim, Germany). Each injection was followed by an equilibration period of 4 min and a stirrer settling time of 10 s before the measurement started. The measurement parameters were set to a step size of 1 nm, a bandwidth of 1 nm, and a DIT of 1 s. After each injection, five spectra were recorded over a wavelength range of 225–275 nm that were averaged for analysis. A titration took about five hours for completion.

3.3.3.2 Oriented Circular Dichroism (OCD) Spectroscopy The rotational orientation of Mistic in a POPC bilayer was analyzed by oriented circular dichroism (OCD) spectroscopy. For such measurements, first, the reconstituted membrane protein or peptide needs to be aligned macroscopically in a multilayer array of stacked lipid bilayers, and second, a CD spectrum is obtained at an orientation of the bilayer normal parallel to the incident light [125, 126].

Reconstitutions used for OCD measurements were performed at an LPR of 400 and a Mistic concentration of 10 μM. Different buffers, means of detergent extraction, and residual amounts of LDAO were explored to eliminate a potential influence of these parameters on the formation of bilayer stacks. Three reconstitutions were performed by CyD-mediated detergent extraction, two of which were performed in the presence of default buffer. For one of these, a highly concentrated HPβCD-solution was used as a titrant to reach a final molar bilayer fraction of LDAO of $X_D^b = 0.04$, whereas a titrant of lower concentration was used for the other one to reach $X_D^b = 0.3$. The third CyD-mediated reconstitution also reached a low LDAO concentration, but was performed in the presence of 10 mM sodium phosphate at pH 7.4 and 10 mM NaF. A fourth reconstitution was carried out similar to the latter but by addition of preformed POPC-LUVs instead of CyD-mediated detergent extraction.

Samples for OCD measurements were prepared by depositing 64 μL of a proteoliposome suspension—corresponding to 200 μg POPC and 8 μg Mistic—onto a circular quartz glass plate of 20-mm diameter (Suprasil QS, Hellma Optics, Jena, Germany) and allowing the solvent to evaporate under the air stream of a fume hood for at least 2 h until the sample appeared dry. The sample on the quartz glass window was then placed over night either in an air-tight box or in a sample holder with a reservoir of saturated K_2SO_4 solution to obtain full hydration at RT, which resulted in spontaneous alignment of the lipid into stacks of well-oriented bilayers [127]. OCD spectra were recorded on a Jasco J-810 spectropolarimeter equipped with a cylindrical OCD cell on a rotation stage including control of temperature and relative humidity as specified in [126]. Measurements were performed at 25°C and 97.8% relative humidity and experimental settings included a step size of 0.1 nm, a bandwidth of 1 nm, a scan speed of 10 nm/min, and a DIT of 8 s. Three OCD spectra each were recorded at eight different equidistant rotation angles of the OCD cell around the beam axis from 180 to 260 nm. These spectra were averaged to account for spectral artifacts due to linear dichroism (LD) that could arise from imperfections in the lamellar lipid bilayer stack and strain birefringence of the quartz glass plate [128]. To ensure low LD artifacts over the entire wavelength range, LD spectra acquired after each series of OCD measurements were evaluated. After subtraction of spectra for lipid films in the absence of Mistic obtained with otherwise identical sample preparation and measurement settings as a reference, OCD spectra were zeroed by an offset taken from the average between 250 and 260 nm. As there is no control over final concentrations and pathlength for OCD samples becasue of the varying thickness of bilayer stacks, OCD spectra were not normalized to mean residue molar ellipticity, but instead normalized to identical intensities at 222 nm to emphasize changes in spectrum shapes.

3.3.4 Fluorescence Spectroscopy

Fluorescence spectroscopy experiments, including reconstitution monitoring, DDFQ, as well as acrylamide quenching, were conducted at 25°C on a Jasco FP 6500 spectrofluorometer. Emission spectra between 305–500 nm were recorded with a 10 mm × 4 mm quartz glass cuvette at an excitation bandwidth of 1 nm, an emission bandwidth of 5 nm, a response time of 1 s, an excitation wavelength of λ_{ex} = 295 nm, a step size of 0.5 nm, a scan speed of 100 nm/min, and high sensitivity setting. Data analysis included averaging of five spectra for each measurement, baseline correction by subtraction of spectra in the absence of fluorophore, zeroing by an offset taken from the average intensity between 480 and 500 nm, and finally applying a fit to the emission spectra on the basis of a log-normal distribution according to Eq. 3.2 as in [129]:

$$I(\lambda) = I_{\max}\exp\left[-\frac{\ln 2}{\ln^2\rho}\ln^2\left(1+\frac{(\lambda-\lambda_{\max})(\rho^2-1)}{\rho\Gamma}\right)\right] \tag{3.2}$$

where $I(\lambda)$ denotes the wavelength-dependent intensity, $\lambda_{\max}$ the wavelength at maximum intensity, $I_{\max}$, Γ the width of the spectrum at half-maximal intensity, and ρ an asymmetry parameter.

3.3.4.1 Acrylamide Quenching Quenching of Mistic W13 emission by acrylamide was used to investigate how different hydrophobic environments, such as micelles composed of different detergents and a POPC lipid bilayer, affect shielding of the fluorophore. Acrylamide can be used as a quencher for this purpose because it has been shown to be able to permeate the lipid bilayer, but unable to quench deeply buried fluorophores [130]. In general, sample volumes of 1.3 mL containing 2 µM Mistic and 5 mM DTT were titrated with a titrant of the same composition and a supplement of 2 M acrylamide. Titration was performed in 25 steps of 10 mM acrylamide to increase acrylamide concentration to up to 250 mM. Acrylamide titrations were carried out with a titrator (Section 3.4) at constant stirring of the sample, variable injection volumes of >5 µL, and sample withdraw for constant total volume.

For measurements on detergent-solubilized Mistic, the samples contained detergent at a concentration of 5 mM above its respective CMC (Tab. 3.2). Titrations on proteoliposomes were performed for Mistic reconstituted by addition of vesicles as well as by CyD-mediated detergent removal. In both cases, samples comprised 0.83 mM POPC corresponding to an LPR of 415. The concentration of remaining LDAO after reconstitution by the addition of vesicles was 0.25 mM, whereas the concentration of free LDAO after CyD-mediated reconstitution was 0.96 mM at total concentrations of 3.75 mM LDAO and 3.13 mM HPβCD. Acrylamide

quenching of 2 μM NATA in the presence of 3.4 mM LDAO served as reference for a water soluble indol fluorophore.

Quenching efficiency was assessed by plotting the ratio of integrated fluorescence intensities in the absence and presence of acrylamide, F_0/F, against the acrylamide concentration, $[Q]$, and determining the Stern–Volmer quenching constant, K_{SV}, from a linear least-squares fit according to the Stern–Volmer equation (Eq. 3.3).

$$\frac{F_0}{F} = 1 + K_{SV}[Q] \tag{3.3}$$

Table 3.2: CMCs of detergents used for acrylamide quenching measurements

detergent	LDAO	DPC	OM	DM	DDM
CMC (mM)	1.84	1.50	21.6	2.03	0.15

The CMCs of alkyl maltosides were taken from [131], and the CMCs of LDAO and DPC from [73].

3.3.4.2 Depth-Dependent Fluorescence Quenching (DDFQ) To investigate membrane penetration of Mistic in a POPC bilayer, depth-dependent fluorescence quenching (DDFQ) was used. This method is based on a dependence of quenching efficiency on the distance between a fluorescent probe and quenchers that are located at different positions along the membrane depth coordinate. Here, the indole chromophore of Mistic's W13 residue served as the probe, whereas a set of three brominated lipids with bromine atoms at different positions of their alkyl chains were used as quenchers. The bromine atoms of the lipids used, 6-7BrPC, 9-10BrPC, and 11-12BrPC, are known from x-ray diffraction experiments [132] to be located 11.0, 8.3, and 6.5 Å, respectively, away from the membrane center [133].

For sample preparation, mixed POPC-LUVs with a mole fraction of quenching lipid $C(h) = 0.3$ were produced as described in Section 3.2.4. For DDFQ measurements, Mistic reconstitution was performed by addition of vesicles because parameters for CyD-mediated reconstitution were not available for mixtures of POPC and brominated lipids. However, the protein concentration required for fluorescence spectroscopy was low, reducing the risk of protein aggregation that might arise from suboptimal reconstitution conditions. For reconstitution, 10 μL LDAO-solubilized Mistic was added to 1 mL LUVs in buffer to reach final concentrations of 1.5 μM Mistic, 0.6 mM Lipid (LPR = 400), and $\leq$ 0.1 mM LDAO in the presence of 5 mM DTT. Reference measurements were performed similarly, but in the absence of LDAO and DTT and with a final concentration of 2.5 μM TOE.

For data analysis, integrated intensities of fits were used instead of peak intensities only to make use of the complete spectral information available, although using peak intensities at

332 nm yielded virtually identical results. Data points for the depth-dependent fluorescence quenching profile (DFQP) were then calculated by taking the logarithm of the ratio of fluorescence without quencher, F_0, to the fluorescence in the presence of quencher, $F(h)$, multiplied with $\exp[C(h)]$ to correct for the fraction of quenching lipid as suggested in [133] (left term in Eq. 3.4 below). Finally, DFQPs were analyzed by the parallax method (PM) [134] as well as by distribution analysis (DA) [133, 135–137]. As pairwise analysis of quenching leads to large variations depending on the pair of quenchers used [136], data for all three quenchers were included in both DA and PM analysis. Moreover, fitting parameters for both original two-parameter PM (PM-2) as well as three-parameter PM (PM-3) [136, 138] were obtained. To account for potential deep membrane penetration, fitting functions for DFQPs comprised two symmetrical components corresponding to *cis*- and *trans*-leaflet quenching as follows:

$$\ln\frac{F_0}{F(h)}\exp[C(h)] = \mathrm{QP}(h - h_\mathrm{m}) + \mathrm{QP}(h + h_\mathrm{m}) \tag{3.4}$$

where h is the distance to the bilayer center. DA is based on a Gaussian function including three parameters, that is, mean depth, h_m, dispersion, σ, and area, S.

$$\mathrm{QP}(h - h_\mathrm{m}) = \frac{S}{\sigma\sqrt{2\pi}} \cdot \exp\left[-\frac{(h - h_\mathrm{m})^2}{2\sigma^2}\right] \tag{3.5}$$

The mean depth, h_m, corresponds to the maximum of the DFQP and represents the most probable location of the fluorescent probe. The dispersion, σ, corresponds to the width of the DFQP and stems from the finite sizes of probe and quencher as well as from their fluctuational distribution within the membrane due to thermal motion. On the basis of σ, the half width (hw) at half-maximum of the underlying distribution of the fluorophore can be estimated by Eq. 3.6 as given in [137].

$$\sigma_\mathrm{trp}^\mathrm{hw} = \sqrt{(\sigma_\mathrm{DFQP}^\mathrm{hw})^2 - (\sigma_\mathrm{Q}^\mathrm{hw})^2} \tag{3.6}$$

where $\sigma_\mathrm{DFQP}^\mathrm{hw} \approx 2.355\sigma$ [137] denotes the width at half-maximum of the DFQP, and $\sigma_\mathrm{trp}^\mathrm{hw}$ and $\sigma_\mathrm{Q}^\mathrm{hw}$ are the widths of fluorophore (trp) and quencher (Q) distribution, respectively.

The area, S, of the DFQP is proportional to several experimental parameters [133], one of which is the absolute degree of probe exposure to the lipid phase, ω:

$$S = \gamma\omega\tau C \tag{3.7}$$

The latter allows gaining information on the relative exposure of a tryptophan residue to the lipid phase provided that (i) ω of a reference compound is known, and presuming (ii) complete

membrane binding of the probe and (iii) equal values of γ for both tryptophan and reference. In this case, the relative exposure, Ω, can be approximated as in Eq. 3.8 [133].

$$\Omega = \frac{\omega_{\text{trp}}}{\omega_{\text{ref}}} = \frac{S_{\text{trp}} \cdot \Phi_{\text{ref}}}{S_{\text{ref}} \cdot \Phi_{\text{trp}}} \tag{3.8}$$

where Φ_{trp} and Φ_{ref} denote the quantum yields of tryptophan and reference, respectively. The quantum yield of Mistic W13 was calculated relative to that of TOE, that is, $\Phi_{\text{TOE}} = 1$, as in Eq. 3.9.

$$\Phi_{\text{trp}} = \Phi_{\text{TOE}} \frac{I_{\text{trp}} \cdot \varepsilon^{\text{TOE}}_{295\text{ nm}}}{I_{\text{TOE}} \cdot \varepsilon^{\text{trp}}_{295\text{ nm}}} \tag{3.9}$$

where I is the integrated fluorescence emission intensity normalized to concentration. As the absorbance of reconstituted Mistic at the high LPR required could not be measured reliably, instead the extinction coefficients of Mistic and TOE at 295 nm in a micellar environment were determined (Section 3.3.1.1) and used to calculate the quantum yield as above. Fluorescence intensities were determined for 1, 1.5, and 2 µM Mistic or TOE in POPC vesicles with the same experimental parameters as for DDFQ measurements. Integrated and normalized fluorescence emission intensities were retrieved by plotting integrals of emmission spectra between 305 and 500 nm versus concentration and taking the slopes of linear least-squares fits to these plots.

PM is based on a parabolic function that also includes three parameters in the case of PM-3 (Eq. 3.10), that is, mean depth, h_{m}, radius of quenching, R_C, and the variable fraction of local quencher, f.

$$\text{QP}(h - h_{\text{m}}) = \pi \cdot C \cdot f \cdot [R_C^2 - (h - h_{\text{m}})^2] \tag{3.10}$$

with $\text{QP}(h - h_{\text{m}}) = 0$ for $h - h_{\text{m}} \geq R_C$, and $f = 1$ for PM-2 [138]. $C = C(h)/A_{\text{L}}$ denotes the total quencher concentration in the lipid bilayer. For POPC, the area per lipid molecule is $A_{\text{L}} = 68$ Å^2 [23]. More details on DA and PM can be found in the references provided throughout this section [133–138].

3.3.5 Dynamic Light Scattering (DLS)

The quality of extruded vesicles and particle size distributions before and after reconstitution were assessed by dynamic light scattering (DLS) on a Zetasizer Nano S90 (Malvern Instruments). The instrument operated at a detection angle of 90° and was equipped with a 633-nm He–Ne laser. For corroboration of unimodal size distributions after extrusion, 1:100-dilutions of vesicles were used in 10 mm × 10 mm disposable polystyrene cuvettes (Sarstedt). Measure-

ments on reconstitution samples were performed with a 3 mm × 3 mm quartz glass cuvette (Hellma Analytics) without dilution. Light scattering intensity was collected in scans of 5 s. Mean count rates were obtained in series of 10 repeated scans at an attenuator position fixed at maximum position (value = 11), whereas size distribution measurements consisted of 30 repeated scans with the attenuator position automatically determined by the instrument software. The influence of all buffer components on viscosity and refractive index were accounted for during data analysis, which was carried out by fitting the experimentally determined autocorrelation function with a non-negatively constrained least-squares function [139] to yield the size distribution in terms of the mean percentage of scattering intensity as a function of particle size. In addition, volume and number distributions were generated by the instrument software from intensity-weighted size distributions on the basis of Mie theory. Prior to each measurement, the sample was allowed to equilibrate to 25°C for 2 min.

To investigate lipid complexation by different CyD derivatives, a solubilization assay was performed by titrating lipid vesicles into CyD solutions and monitoring the light scattering intensity [140]. A stock suspension of lipid vesicles prepared by extrusion (Section 3.2.4) with a concentration of 13.25 mM was titrated to a 50-mM CyD solution in 20 injections of 6 µL each. The titrant contained the same CyD concentration as the titrand to maintain a constant CyD concentration throughout the titration, and all solutions and suspensions were prepared with default buffer. The solubilization of LUVs comprising either POPC or DLPC by MβCD as well as HPβCD was investigated. Solubilization assays were carried out with disposable polystyrene cuvettes at an attenuator position fixed at 11 using otherwise identical measurement settings as above.

3.4 Automated Titrations

Real-time monitoring of Mistic reconstitution by DLS and fluorescence spectroscopy as well as acrylamide quenching experiments were realized with a Microlab 500 titrator (Hamilton, Reno, USA) for improved reproducibility and reduced user attendance. As the only software control available for the titrator was limited to the use in conjunction with a Chirascan-plus spectropolarimeter, a script was written that enables access to the titrator controls of the spectrometer control software in emulation mode. The script was written for AutoIt[1], a freeware BASIC like scripting language for Microsoft Windows that allows for the simulation of keystrokes and mouse movements, manipulation of windows and processes, and interaction with standard Windows controls [141].

[1] Bennett J.: AutoIt, `https://www.autoitscript.com/` accessed Friday 19th February, 2016

The script enabled the synchronization of titrator and instrument softwares (Zetasizer v7.03 for Zetasizer Nano S90 or Spectra manager v1.54.03 for Jasco FP 6500) and included a graphical user interface allowing setting the following parameters: (i) instrument to be used (None, Zetasizer Nano S90, Jasco FP 6500, or Jasco V-630), (ii) titration (enabled or disabled for kinetic measurements), (iii) number of injections, (iv) time spacing between injections, (v) number of measurements per injection ("repeats"), (vi) fixed injection volume or fixed concentration steps, (vii) injection volume or concentration steps, (viii) option to refill the titrant syringe if emptied, (ix) option to use second syringe to mix the sample (x) after injections or after each measurement, (xi) mixing by withdraw or combined with air purging to prevent sample retention in the tubing, (xii) mixing volume and number of mixing repeats, (xiii) syringe speeds for both syringes, (xiii) number of measurements after titration to check for equilibrium, and (xiv) delay between injection and measurement for sample equilibration. Usability of the script was complemented by the possibility to save and load parameter settings, creation of a log-file for each measurement, display of measurement progression during titration, and a short user guide.

3.5 Confidence Interval Analysis

The Microsoft Excel add-in Solver (Frontline Systems, Incline Village, USA) was used for NLSFs. The reliability of best-fit (bf) values thus obtained was evaluated in terms of confidence interval analysis as detailed in [142]. In brief, the fitting procedure was repeated while fixing the parameter of interest at different values close to its best-fit value and keeping the remaining parameters adjustable. After each fitting cycle, the sum of squared residuals between data and fit, SSR, was used to calculate the corresponding percentile of Fisher's F-distribution, P, according to Eq. 3.11.

$$P = 1 - F\left(\left(\frac{\mathrm{SSR}}{\mathrm{SSR_{bf}}} - 1\right)\frac{N-M}{M}; M; N-M\right) \tag{3.11}$$

with $\mathrm{SSR_{bf}}$ being the SSR of the best fit, N the number of data points, and M the number of adjustable parameters. F is the right-tailed probability from the F-distribution for the given number of degrees of freedom. Percentiles were plotted versus the relative deviation of the fixed parameter from the best-fit value to yield a diagram that allows extracting the confidence interval for any desired level of confidence. The percentile for a given parameter value provides the fractional probability that the parameter value obtained by the NLSF deviates equal or less from the best-fit value. In the following Section, errors for parameter values determined by NLSFs are given in terms of margins of the 95% confidence interval.

4 Theory

4.1 The Pseudophase Concept

For a systematic approach to membrane-protein reconstitution, a theoretical framework is required that describes the interplay among protein, lipid, and detergent. From a thermodynamic viewpoint, the supramolecular structures that are observed owing to colloidal self-assembly phenomena during solubilization and reconstitution can be described—to a good approximation—as pseudophases [143]. The pseudophase concept lends itself to define the changes of the aggregational state in a given lipid/detergent mixture in terms of phase transitions, which are captured in a phase diagram. On the premise that partitioning of lipid and detergent among the pseudophases is not influenced by the membrane protein, such a phase diagram is two-dimensional and thus, provides pairs of lipid and detergent concentrations that characterize the occurrence of phase transitions.

For cyclodextrin (CyD)-driven reconstitution, the set of partition equilibria needs to be expanded by the equilibrium between CyD and free detergent, and the CyD/detergent inclusion complex. Thus, a quantitative model describing the linked equilibria in a ternary CyD/lipid/detergent mixture was furnished [80, 81] by combining a partitioning model for lipid/detergent mixtures [122] with a model for competitive binding [144–146] (Fig. 4.1).

In a lipid/detergent mixture, the detergent (D) can reside in the aqueous phase (aq), the bilayer phase (b), and the micellar phase (m). The lipid (L), to a good approximation, can partition only between the latter two as to its sub-micromolar solubility [22]. Moreover, an inclusion complex (i) can be formed by binding of detergent to CyD. The quantitative model assumes high specificity for inclusion complex formation and, thus, considers lipid binding to CyD negligible. In the following equations, the notation refers to molecular components (i.e., D, L, and CyD) in subscripts and pseudophases (i.e., aq, b, and m) or inclusion complex (i.e., i) in superscripts.

4.2 Transbilayer Movement of Detergents

In any ITC experiment, complete equilibration needs to be reached after each injection. For solubilization and reconstitution experiments, this is the case only if detergent partitioning is accompanied by sufficiently fast transbilayer distribution, which is true for most neutral detergents like oligo (ethylene oxide) dodecyl ethers and octyl glucoside [147, 148]. However,

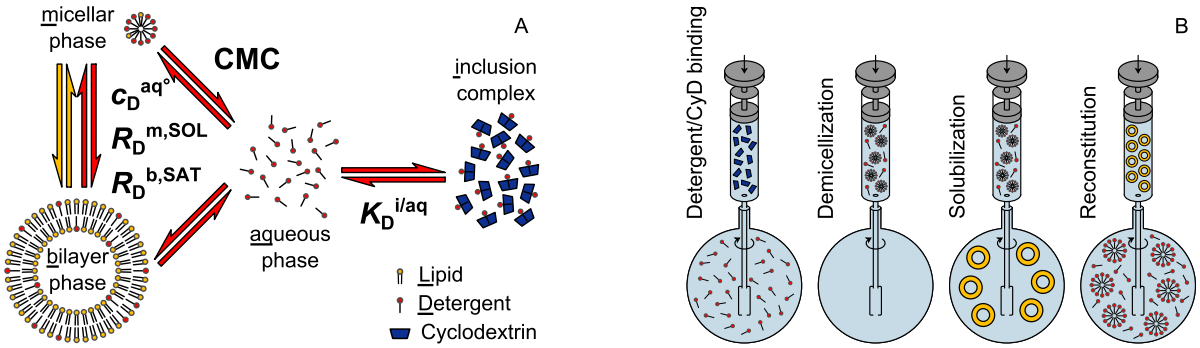

Figure 4.1: Quantitative Model for CyD-driven Detergent-Removal.
(A) Overview of chemical species, pseudophases, and linked equilibria involved in CyD-mediated reconstitution and (bold) thermodynamic parameters required for quantitative description. (B) Calorimetric experiments for obtaining thermodynamic parameters describing CyD-driven reconstitution. (Trapezoids) CyD, (circles) lipid, and (sticks) detergent. Figure adapted from [81] with permission from Elsevier.

as LDAO bears a zwitterionic headgroup, its passive translocation between the two bilayer leaflets of POPC vesicles was investigated by ITC with an uptake and release protocol [149–151].

An uptake and release protocol compares partitioning data from an uptake experiment, where lipid vesicles are added to detergent at submicellar concentration, with that from a release experiment, where vesicles preloaded homogeneously with detergent in both bilayer leaflets are diluted into buffer. If the detergent is unable to cross the lipid bilayer, one-sided membrane binding occurs in the uptake experiment, and only detergent from the outer bilayer leaflet is able to partition into the aqueous phase in the release experiment. Thus, slow detergent translocation results in different kinetically entrapped nonequilibrium states, whereas the same state is reached for fast transbilayer permeation in both experiments. The fraction of the bilayer phase accessible to detergent is defined by the lipid accessibility factor γ, which amounts to $\gamma = 1$ for permeable liposomes and to $\gamma = 0.5$ for impermeable LUVs as, in approximation, both inner and outer bilayer leaflet contain the same amount of lipid.

To obtain γ, a nonlinear least-squares fit (NLSF) was applied to the integrated and normalized heats of uptake and release experiments, according to Eq. 4.1 as in [151]. The partition coefficient for the transfer of detergent between aqueous phase and bilayer phase as well as γ and the standard molar enthalpy, $\Delta H_D^{b/aq,\circ}$, were globally fitted, whereas heats of dilution were set as local fitting parameters.

$$Q(i) = \frac{\Delta n_D^{trans}(i)\Delta H_D^{b/aq,\circ}}{\Delta V(i) c_L^{syr}} + Q_{dil} \tag{4.1}$$

where $Q(i)$ denotes the normalized heat of injection, Q_{dil} the normalized heat of dilution, $n_{\mathrm{S}}^{\mathrm{trans}}(i)$ the mole number of detergent that is transferred between lipid bilayer and aqueous phase upon re-equilibration, $c_{\mathrm{L}}^{\mathrm{syr}}$ the lipid concentration in the syringe, and $\Delta V(i)$ the net injection volume. As in [151], $\Delta n_{\mathrm{D}}^{\mathrm{trans}}(i)$ is given by:

$$\Delta n_{\mathrm{D}}^{\mathrm{trans}}(i) = V_0 \Delta c_{\mathrm{D}}^{\mathrm{b}^*}(i) - \Delta V(i) \left[c_{\mathrm{D}}^{\mathrm{b,syr}^*} - 0.5(c_{\mathrm{D}}^{\mathrm{b}^*}(i) + c_{\mathrm{D}}^{\mathrm{b}^*}(i-1)) \right] \tag{4.2}$$

where V_0 denotes the total cell volume and the asterisk indicates the exclusion of detergent entrapped within the inner bilayer leaflet. For $\gamma \neq 1$, the concentration of accessible lipid amounts to $c_{\mathrm{L}}^{*} = \gamma c_{\mathrm{L}}$. The fitting procedure was employed both based on a mole fraction partition coefficient, $P_{\mathrm{D}}^{\mathrm{b/aq}}$, and a mole ratio partition coefficient, $K_{\mathrm{D}}^{\mathrm{b/aq}}$ analogous to [151]. $P_{\mathrm{D}}^{\mathrm{b/aq}}$ is constant for ideal mixing of detergent and lipid, with

$$P_{\mathrm{D}}^{\mathrm{b/aq}} = \frac{c_{\mathrm{D}}^{\mathrm{b}^*} c_{\mathrm{W}}}{c_{\mathrm{D}}^{\mathrm{aq}} (c_{\mathrm{L}}^{*} + c_{\mathrm{D}}^{\mathrm{b}^*})} \tag{4.3}$$

with the concentration of water $c_{\mathrm{W}} = 55.5$ M. Inserting the mass balance equation $c_{\mathrm{D}}^{\mathrm{aq}} = c_{\mathrm{D}}^{*} - c_{\mathrm{D}}^{\mathrm{b}^*}$ into Eq. 4.3 and solving for $c_{\mathrm{D}}^{\mathrm{b}^*}$ furnishes a quadratic solution for the concentration of membrane-bound detergent:

$$c_{\mathrm{D}}^{\mathrm{b}^*} = \frac{-q + \sqrt{q^2 - 4r}}{2} \tag{4.4}$$

$$q = c_{\mathrm{L}}^{*} - c_{\mathrm{D}}^{*} + \frac{c_{\mathrm{W}}}{P_{\mathrm{D}}^{\mathrm{b/aq}}} \tag{4.5}$$

$$r = -c_{\mathrm{L}}^{*} c_{\mathrm{D}}^{*} \tag{4.6}$$

A partition model considering non-ideal mixing is better described by a mole ratio partition coefficient, $K_{\mathrm{D}}^{\mathrm{b/aq}}$, with

$$c_{\mathrm{D}}^{\mathrm{b}^*} = c_{\mathrm{D}}^{*} \frac{K_{\mathrm{D}}^{\mathrm{b/aq}} c_{\mathrm{L}}^{*}}{1 + K_{\mathrm{D}}^{\mathrm{b/aq}} c_{\mathrm{L}}^{*}} \tag{4.7}$$

According to [152], a mole fraction partition coefficient can be converted to a mole ratio partition coefficient with Eq. 4.8.

$$K_{\mathrm{D}}^{\mathrm{b/aq}} = \frac{P_{\mathrm{D}}^{\mathrm{b/aq}} (1 + R^{\mathrm{b}})}{c_{\mathrm{W}}} \tag{4.8}$$

where R^{b} denotes the mole ratio of surfactant to lipid in the membrane.

4.3 Inclusion Complex Formation

Presuming a 1:1 stoichiometry for binding of detergent to CyD, the inclusion complex is formed according to

$$c_{\mathrm{D}}^{\mathrm{aq}} + c_{\mathrm{CyD}}^{\mathrm{aq}} \rightleftharpoons c_{\mathrm{D}}^{\mathrm{i}} \tag{4.9}$$

where $c_{\mathrm{D}}^{\mathrm{aq}}$ and $c_{\mathrm{CyD}}^{\mathrm{aq}}$ denote the molar concentrations of unbound detergent and CyD in the aqueous phase, respectively, and $c_{\mathrm{D}}^{\mathrm{i}}$ the molar concentration of detergent in the inclusion complex, which is identical to the concentration of CyD in the inclusion complex for equimolar complex formation. This binding equilibrium is characterized by the dissociation constant $K_{\mathrm{D}}^{\mathrm{i/aq}}$ as

$$K_{\mathrm{D}}^{\mathrm{i/aq}} \equiv \frac{c_{\mathrm{D}}^{\mathrm{aq}} c_{\mathrm{CyD}}^{\mathrm{aq}}}{c_{\mathrm{D}}^{\mathrm{i}}} \tag{4.10}$$

Substituting $c_{\mathrm{CyD}}^{\mathrm{aq}} = c_{\mathrm{CyD}} - c_{\mathrm{D}}^{\mathrm{i}}$ into Eq. 4.10 then yields

$$c_{\mathrm{D}}^{\mathrm{i}} = \frac{c_{\mathrm{D}}^{\mathrm{aq}}}{c_{\mathrm{D}}^{\mathrm{aq}} + K_{\mathrm{D}}^{\mathrm{i/aq}}} c_{\mathrm{CyD}} \tag{4.11}$$

with c_{CyD} denoting the total concentration of CyD.

4.4 Demicellization

The partition coefficient for the transfer of a detergent monomer from the aqueous phase to the micellar phase, $P_{\mathrm{D}}^{\mathrm{m/aq}}$, can be derived from the critical micelle concentration (CMC) of the detergent according to Eq. 4.12.

$$P_{\mathrm{D}}^{\mathrm{m/aq}} \equiv \frac{X_{\mathrm{D}}^{\mathrm{m}}}{X_{\mathrm{D}}^{\mathrm{aq}}} = \frac{c_{\mathrm{D}}^{\mathrm{aq}} + c_W}{c_{\mathrm{D}}^{\mathrm{aq}}} \approx \frac{c_{\mathrm{W}}}{c_{\mathrm{D}}^{\mathrm{aq}}} = \frac{c_{\mathrm{W}}}{\mathrm{CMC}} \tag{4.12}$$

with $X_{\mathrm{D}}^{\mathrm{m}} = 1$ and $X_{\mathrm{D}}^{\mathrm{aq}}$ denoting the mole fractions of detergent in the micellar and aqueous phases, respectively. The molar concentration of detergent monomers in the bulk aqueous phase, $c_{\mathrm{D}}^{\mathrm{aq}}$, is negligible in comparison with the concentration of water, because the latter is much higher. In the absence of lipid, $c_{\mathrm{D}}^{\mathrm{aq}} = \mathrm{CMC}$. The CMC of LDAO was determined calorimetrically by a demicellization experiment, where the detergent at micellar concentration was titrated to buffer. Such an experiment typically gives rise to an isotherm of sigmoidal shape, the inflection point of which corresponds to the CMC. To extract the CMC, a two-step strategy

was used as elaborated in [153]. In brief, the two major approaches conventionally used to analyze demicellization isotherms were combined, that is, taking the extremum of the numeric derivative of the isotherm as the CMC [154] and inferring the CMC from a generic sigmoidal fit to the isotherm [131, 155]. Conjunction of these two approaches consisted in using estimates from the first approach as starting values for the fitting procedure of the second approach.

Estimates for Fitting Parameters First, the slopes between each two consecutive heats of injections were calculated to obtain the numeric derivative of the isotherm. After smoothing with a moving average to account for experimental noise, the extremum of the derivative was taken as the initial estimate of the CMC. Second, the coefficients of pre- and post-transition baselines were estimated on the basis of linear-least-squares fits. Third, from these values the estimate of the heat of demicellization was calculated according to Eq. 4.13.

$$Q_{\text{demic}} = m_1\text{CMC} + b_1 - m_2\text{CMC} - b_2 \tag{4.13}$$

From Q_{demic}, an estimate for the standard molar micellization enthalpy, $\Delta H^{\circ}_{\text{mic}}$, was obtained by normalization with respect to the fraction of micellar surfactant in the syringe.

$$\Delta H^{\circ}_{\text{mic}} = -Q_{\text{demic}} \frac{c_{\text{D}}^{\text{syr}}}{c_{\text{D}}^{\text{syr}} - \text{CMC}} \tag{4.14}$$

Finally, an estimate of Δc_{D} (cf. Eq. 4.16) was calculated on the basis of the slope of the isotherm at the CMC according to Eq. 4.15.

$$\Delta c_{\text{D}} = \frac{\text{CMC}}{2m^{\text{n}}_{\text{CMC}}}\left(1 - \frac{m^{\text{n}}_1 + m^{\text{n}}_2}{2}\right) \tag{4.15}$$

where slopes are normalized to the entire data range. The term in parentheses accounts for the fact that an increase in the baseline slopes may flatten the isotherm in a manner similar to the effect of increasing Δc_{D}.

Generic Sigmoidal Fit In the second step of analysis, a NLSF was applied to the isotherm based on Eq. 4.16 [131, 155].

$$Q(c_{\text{D}}) = \frac{A_1 - A_2}{1 + \exp\left(\frac{c_{\text{D}} - \text{CMC}}{\Delta c_{\text{D}}}\right)} + A_2 \tag{4.16}$$

with $Q(c_{\text{D}})$ denoting the normalized heat of reaction, c_{D} the detergent concentration in the calorimeter cell, and Δc_{D} a measure for the steepness of the isotherm or, in other terms, the

width of the transition range. The baselines for pre- and post-transition regions are described by linear functions A_1 and A_2.

$$A_1 = m_1 c_\mathrm{D} + b_1 \tag{4.17}$$

$$A_2 = m_2 c_\mathrm{D} + b_2 \tag{4.18}$$

Solving Eq. 4.14 for Q_demic, inserting into Eq. 4.13, solving the latter for b_1, and substituting into Eq. 4.16 yields the generic sigmoidal function (Eq. 4.19) that was ultimately used to fit the experimental data.

$$Q(c_\mathrm{D}) = \frac{(m_1 - m_2)(c_\mathrm{D} - \mathrm{CMC}) - \Delta H^\circ_\mathrm{mic}(c_\mathrm{D}^\mathrm{syr} - \mathrm{CMC})/c_\mathrm{D}^\mathrm{syr}}{1 + \exp(\frac{c_\mathrm{D} - \mathrm{CMC}}{\Delta c_\mathrm{D}})} + m_2 c_\mathrm{D} + b_2 \tag{4.19}$$

4.5 Lipid/Detergent Phase Diagram

A binary phase diagram is obtained by plotting detergent concentrations against the corresponding lipid concentrations at the phase boundaries (Fig. 2.2 A). In approximation, for many lipid/detergent mixtures the phase boundaries correspond to two straight lines [143, 156, 157] referred to as the saturation (SAT) boundary and the solubilization (SOL) boundary. These phase boundaries separate three ranges of different pseudophase composition, namely, (i) a vesicle range comprising mixed lipid/detergent vesicles only, (ii) a coexistence range that is characterized by the simultaneous presence of mixed micelles and vesicles, and (iii) a micellar range, wherein only mixed micelles exist. The phase boundaries are defined by their slopes, $R_\mathrm{D}^\mathrm{b,SAT}$, and $R_\mathrm{D}^\mathrm{m,SOL}$, respectively, and their ordinate intercepts, $c_\mathrm{D}^\mathrm{aq,SAT}$, and $c_\mathrm{D}^\mathrm{aq,SOL}$, respectively, which correspond to the concentrations of detergent monomers in the aqueous phase:

$$c_\mathrm{D}^\mathrm{SAT} = R_\mathrm{D}^\mathrm{b,SAT} c_\mathrm{L} + c_\mathrm{D}^\mathrm{aq,SAT} \tag{4.20}$$

$$c_\mathrm{D}^\mathrm{SOL} = R_\mathrm{D}^\mathrm{m,SOL} c_\mathrm{L} + c_\mathrm{D}^\mathrm{aq,SOL} \tag{4.21}$$

where $c_\mathrm{D}^\mathrm{SAT}$ is the total detergent concentration necessary for saturation of the bilayer with detergent, $c_\mathrm{D}^\mathrm{SOL}$ the total detergent concentration necessary for complete solubilization, and c_L the total lipid concentration. The slopes correspond to the molar ratios of detergent to lipid in lipid-saturated micelles, $R_\mathrm{D}^\mathrm{b,SAT} \equiv c_\mathrm{D}^\mathrm{b,SAT}/c_\mathrm{L}$, and in detergent-saturated bilayers, $R_\mathrm{D}^\mathrm{m,SOL} \equiv c_\mathrm{D}^\mathrm{m,SOL}/c_\mathrm{L}$,

respectively. Following from Gibbs' phase rule [158], the phase boundaries have a common ordinate intercept, $c_{\mathrm{D}}^{\mathrm{aq}^{\circ}} \equiv c_{\mathrm{D}}^{\mathrm{aq,\,SOL}} = c_{\mathrm{D}}^{\mathrm{aq,\,SAT}}$. Within the coexistence range, bilayer and micelle compositions as well as the concentration of detergent monomers in the aqueous phase remain constant. The latter is smaller than the CMC of the detergent because it refers to detergent monomers in equilibrium with mixed micelles and mixed bilayers instead of pure detergent micelles [159].

From the slopes of the phase boundaries, the mole fractions of detergent in detergent-saturated bilayers and in lipid-saturated micelles can be determined as

$$X_{\mathrm{D}}^{\mathrm{b,SAT}} = \frac{R_{\mathrm{D}}^{\mathrm{b,SAT}}}{1 + R_{\mathrm{D}}^{\mathrm{b,SAT}}} \tag{4.22}$$

$$X_{\mathrm{D}}^{\mathrm{m,SOL}} = \frac{R_{\mathrm{D}}^{\mathrm{m,SOL}}}{1 + R_{\mathrm{D}}^{\mathrm{m,SOL}}} \tag{4.23}$$

Pseudophase partitioning is described by partition equilibria, including the equilibrium for the transfer of lipid between micellar and bilayer phase, and equilibria for the transfer of detergent between micellar and bilayer phase as well as between aqueous and bilayer phase. These equilibria are characterized by the respective partition coefficients, $P_{\mathrm{L}}^{\mathrm{b/m}}$, $P_{\mathrm{D}}^{\mathrm{b/m}}$, and $P_{\mathrm{D}}^{\mathrm{b/aq}}$, which are given by the mole fractions of lipid and detergent in the pseudophases according to Eq. 4.24 and Eqs. 4.25 and 4.26, respectively.

$$P_{\mathrm{L}}^{\mathrm{b/m}} = \frac{X_{\mathrm{L}}^{\mathrm{b}}}{X_{\mathrm{L}}^{\mathrm{m}}} = \frac{1 - X_{\mathrm{D}}^{\mathrm{b}}}{1 - X_{\mathrm{D}}^{\mathrm{m}}} = \frac{c_{\mathrm{L}}^{\mathrm{b}}(c_{\mathrm{L}}^{\mathrm{m}} + c_{\mathrm{D}}^{\mathrm{m}})}{c_{\mathrm{L}}^{\mathrm{m}}(c_{\mathrm{L}}^{\mathrm{b}} + c_{\mathrm{D}}^{\mathrm{b}})} \tag{4.24}$$

$$P_{\mathrm{D}}^{\mathrm{b/m}} = \frac{X_{\mathrm{D}}^{\mathrm{b}}}{X_{\mathrm{D}}^{\mathrm{m}}} = \frac{c_{\mathrm{D}}^{\mathrm{b}}(c_{\mathrm{L}}^{\mathrm{m}} + c_{\mathrm{D}}^{\mathrm{m}})}{c_{\mathrm{D}}^{\mathrm{m}}(c_{\mathrm{L}}^{\mathrm{b}} + c_{\mathrm{D}}^{\mathrm{b}})} \tag{4.25}$$

$$P_{\mathrm{D}}^{\mathrm{b/aq}} = \frac{X_{\mathrm{D}}^{\mathrm{b}}}{X_{\mathrm{D}}^{\mathrm{aq}}} = \frac{c_{\mathrm{D}}^{\mathrm{b}}(c_{\mathrm{D}}^{\mathrm{aq}} + c_{\mathrm{W}})}{c_{\mathrm{D}}^{\mathrm{aq}}(c_{\mathrm{L}}^{\mathrm{b}} + c_{\mathrm{D}}^{\mathrm{b}})} \approx \frac{c_{\mathrm{D}}^{\mathrm{b}} c_{\mathrm{W}}}{c_{\mathrm{D}}^{\mathrm{aq}}(c_{\mathrm{L}}^{\mathrm{b}} + c_{\mathrm{D}}^{\mathrm{b}})} \tag{4.26}$$

4.6 Combination of Linked Equilibria

The equilibrium between CyD and detergent as described in Section 4.3 is combined with the partition equilibria from Sections 4.4 and 4.5 on the basis of mass conservation, which entails a total detergent concentration of

$$c_{\mathrm{D}} = c_{\mathrm{D}}^{\mathrm{m}} + c_{\mathrm{D}}^{\mathrm{b}} + c_{\mathrm{D}}^{\mathrm{aq}} + c_{\mathrm{D}}^{\mathrm{i}} \tag{4.27}$$

and a total lipid concentration of

$$c_{\mathrm{L}} = c_{\mathrm{L}}^{\mathrm{m}} + c_{\mathrm{L}}^{\mathrm{b}} \tag{4.28}$$

To predict the supramolecular state of a given mixture of lipid, detergent, and CyD, the concentration of free detergent that is not sequestered by CyD and thus able to partition between pseudophases, $c_{\mathrm{D}}^{\mathrm{free}} = c_{\mathrm{D}} - c_{\mathrm{D}}^{\mathrm{i}}$, needs to be known. Taking Eq. 4.11 into consideration, $c_{\mathrm{D}}^{\mathrm{free}}$ ultimately depends on $c_{\mathrm{D}}^{\mathrm{aq}}$. Seperate solutions for $c_{\mathrm{D}}^{\mathrm{aq}}$ apply to the three ranges of the phase diagram because of the different accessibility of pseudophases.

Coexistence Range Within the coexistence range, the concentration of detergent in the aqueous phase is constant with $c_{\mathrm{D}}^{\mathrm{aq}} = c_{\mathrm{D}}^{\mathrm{aq}^\circ}$. The concentration of lipid in the micellar phase derives from combining this equality with Eqs. 4.27 and 4.28 and with the definitions of $R_{\mathrm{D}}^{\mathrm{b,SAT}}$ and $R_{\mathrm{D}}^{\mathrm{m,SOL}}$.

$$c_{\mathrm{L}}^{\mathrm{m}} = \frac{c_{\mathrm{D}} - c_{\mathrm{D}}^{\mathrm{aq}^\circ} - c_{\mathrm{D}}^{\mathrm{i}} - R_{\mathrm{D}}^{\mathrm{b,SAT}} c_{\mathrm{L}}}{R_{\mathrm{D}}^{\mathrm{m,SOL}} - R_{\mathrm{D}}^{\mathrm{b,SAT}}} \tag{4.29}$$

where $c_{\mathrm{D}}^{\mathrm{i}}$ is given by Eq. 4.11, and, given that in the coexistence range $X_{\mathrm{D}}^{\mathrm{m}} = X_{\mathrm{D}}^{\mathrm{m,SOL}}$, $c_{\mathrm{D}}^{\mathrm{aq}^\circ}$ is provided by combination of Eqs. 4.12 and 4.23 according to Eq. 4.30.

$$c_{\mathrm{D}}^{\mathrm{aq}^\circ} = \mathrm{CMC} \cdot X_{\mathrm{D}}^{\mathrm{m,SOL}} = \mathrm{CMC} \cdot \frac{R_{\mathrm{D}}^{\mathrm{m,SOL}}}{1 + R_{\mathrm{D}}^{\mathrm{m,SOL}}} \tag{4.30}$$

The concentration of detergent in the micellar phase is then obtained through the definition of $R_{\mathrm{D}}^{\mathrm{m,SOL}}$ according to Eq. 4.31.

$$c_{\mathrm{D}}^{\mathrm{m}} = R_{\mathrm{D}}^{\mathrm{m,SOL}} c_{\mathrm{L}}^{\mathrm{m}} \tag{4.31}$$

Concentrations of detergent and lipid in the bilayer phase can then be calculated using the mass balance Eqs. 4.27 and 4.28, respectively.

Micellar Range Within the micellar range, lipid only resides in the micellar phase, thus $c_{\mathrm{L}}^{\mathrm{m}} = c_{\mathrm{L}}$, insertion of which into Eq. 4.12 and combining with $X_{\mathrm{D}}^{\mathrm{m}} = X_{\mathrm{D}}^{\mathrm{m,SOL}} = c_{\mathrm{D}}^{\mathrm{m}}/(c_{\mathrm{D}}^{\mathrm{m}} + c_{\mathrm{L}}^{\mathrm{m}})$ and $X_{\mathrm{D}}^{\mathrm{aq}} = c_{\mathrm{D}}^{\mathrm{aq}}/(c_{\mathrm{D}}^{\mathrm{aq}} + c_{\mathrm{W}})$ gives

$$c_{\mathrm{D}}^{\mathrm{m}} = \frac{c_{\mathrm{D}}^{\mathrm{aq}} P_{\mathrm{D}}^{\mathrm{m/aq}}}{c_{\mathrm{W}} - c_{\mathrm{D}}^{\mathrm{aq}} P_{\mathrm{D}}^{\mathrm{m/aq}}} c_{\mathrm{L}} \tag{4.32}$$

Combining Eq. 4.32 with Eqs. 4.11 and 4.27 furnishes

$$c_{\mathrm{D}}^{\mathrm{aq}} = c_{\mathrm{D}} - \frac{c_{\mathrm{D}}^{\mathrm{aq}} P_{\mathrm{D}}^{\mathrm{m/aq}}}{c_{\mathrm{W}} - c_{\mathrm{D}}^{\mathrm{aq}} P_{\mathrm{D}}^{\mathrm{m/aq}}} c_{\mathrm{L}} - \frac{c_{\mathrm{CyD}} c_{\mathrm{D}}^{\mathrm{aq}}}{c_{\mathrm{D}}^{\mathrm{aq}} + K_{\mathrm{D}}^{\mathrm{i/aq}}} \tag{4.33}$$

which can be rearranged into a cubic equation of the form

$$c_{\mathrm{D}}^{\mathrm{aq}^3} + p c_{\mathrm{D}}^{\mathrm{aq}^2} + q c_{\mathrm{D}}^{\mathrm{aq}} + r = 0 \tag{4.34}$$

with coefficients

$$p = P_{\mathrm{D}}^{\mathrm{m/aq}} (K_{\mathrm{D}}^{\mathrm{i/aq}} + c_{\mathrm{CyD}} - c_{\mathrm{D}} - c_{\mathrm{L}}) - c_{\mathrm{W}} \tag{4.35}$$

$$q = c_{\mathrm{W}} (c_{\mathrm{D}} - c_{\mathrm{CyD}} - K_{\mathrm{D}}^{\mathrm{i/aq}}) - P_{\mathrm{D}}^{\mathrm{m/aq}} K_{\mathrm{D}}^{\mathrm{i/aq}} (c_{\mathrm{D}} - c_{\mathrm{L}}) \tag{4.36}$$

$$r = K_{\mathrm{D}}^{\mathrm{i/aq}} c_{\mathrm{D}} c_{\mathrm{W}} \tag{4.37}$$

The single physically meaningful solution of Eq. 4.34 is

$$c_{\mathrm{D}}^{\mathrm{aq}} = \frac{2}{3} \sqrt{p^2 - 3q} \cos\left(\frac{2\pi - \Theta}{3}\right) - \frac{p}{3} \tag{4.38}$$

where

$$\Theta = \arccos \frac{-2p^3 + 9pq - 27r}{2\sqrt{(p^2 - 3q)^3}} \tag{4.39}$$

Bilayer Range Within the bilayer range, lipid resides only in the bilayer phase, thus $c_{\mathrm{L}}^{\mathrm{b}} = c_{\mathrm{L}}$, insertion of which into Eq. 4.26 yields

$$c_{\mathrm{D}}^{\mathrm{b}} = \frac{c_{\mathrm{D}}^{\mathrm{aq}} P_{\mathrm{D}}^{\mathrm{b/aq}}}{c_{\mathrm{W}} - c_{\mathrm{D}}^{\mathrm{aq}} P_{\mathrm{D}}^{\mathrm{b/aq}}} c_{\mathrm{L}} \tag{4.40}$$

in analogy to Eq. 4.32. Adopting the same substitutions and rearrangements as used above for the micellar range results in a cubic equation with coefficients analogous to those in Eqs. 4.35–4.37, the only difference being that $P_{\mathrm{D}}^{\mathrm{b/aq}}$ now takes the place of $P_{\mathrm{D}}^{\mathrm{m/aq}}$.

5 Results

5.1 Suitability of Compounds

The first major goal of this thesis was the establishment of a protocol for Mistic reconstitution by quantitative cyclodextrin (CyD)-mediated detergent extraction. Prior to the determination of the parameters that are required for application of the quantitative model devised in Section 4, (i) verification of fast interleaflet translocation of LDAO was required (Section 5.1.1), and (ii) a suitable CyD derivative had to be found that ensures high selectivity towards LDAO to exclude unspecific complexation of lipid (Section 5.1.2).

5.1.1 LDAO Interleaflet Translocation

The ability of LDAO to translocate between the two leaflets of a POPC bilayer within the experimental timescale of a reconstitution experiment was verified by uptake and release experiments (Section 3.3.2.1). These experiments probe the accessibility of the inner vesicle leaflet to detergent from the exterior aqueous solution (Section 4.2). In general, transbilayer equilibration is energetically unfavorable and slow at ambient temperature for nonionic detergents with large headgroups and ionic detergents such as sodium dodecyl sulfate. By contrast, fast kinetics is expected for the interleaflet translocation of nonionic detergents bearing small headgroups. For zwitterionic detergents such as LDAO, kinetics may vary in dependence of headgroup size.

The results of uptake and release experiments for LDAO are shown in Figure 5.1. The global nonlinear least-squares fit (NLSF) to the isotherms of both experiments (Fig. 5.1 B) yielded $K_{\mathrm{D}}^{\mathrm{b/aq}} = (1.17 \pm 0.08)\ \mathrm{mM}^{-1}$, $\Delta H_{\mathrm{D}}^{\mathrm{b/aq},\circ} = (10.02 \pm 0.52)$ kJ/mol, and an accessible lipid fraction of $\gamma = 1.08 \pm 0.11$, suggesting that LDAO quickly equilibrates across POPC membranes at 25°C. In conclusion, LDAO was a suitable detergent for the subsequent reconstitution experiments. When the NLSF was based on a mole fraction partition coefficient instead of a mole ratio partition coefficient, similar values were obtained for γ (1.02 ± 0.11) and $\Delta H_{\mathrm{D}}^{\mathrm{b/aq},\circ}$ ((10.23 ± 0.56) kJ/mol) with $P_{\mathrm{D}}^{\mathrm{b/aq}} = 62.8 \times 10^3 \pm 3.1 \times 10^3$. With the identity $\Delta G^\circ = -RT\ln P_{\mathrm{D}}^{\mathrm{b/aq}}$, the standard molar Gibbs free energy for the transfer of LDAO from the aqueous phase to the bilayer phase was calculated to $\Delta G_{\mathrm{D}}^{\mathrm{b/aq},\circ} = (-27.4 \pm 0.1)$ kJ/mol. Following from the equation $\Delta G_{\mathrm{D}}^{\mathrm{b/aq},\circ} = \Delta H_{\mathrm{D}}^{\mathrm{b/aq},\circ} - T\Delta S_{\mathrm{D}}^{\mathrm{b/aq},\circ}$, the change in entropy amounts to $-T\Delta S_{\mathrm{D}}^{\mathrm{b/aq},\circ} = (-37.4 \pm 0.7)$ kJ/mol. Thus, as expected owing to the energetic penalty for the exposure of the hydrophobic detergent tails to the solvent, the transfer of LDAO to the

lipid bilayer is highly favorable and dominated by the entropic contribution because of the hydrophobic effect [16].

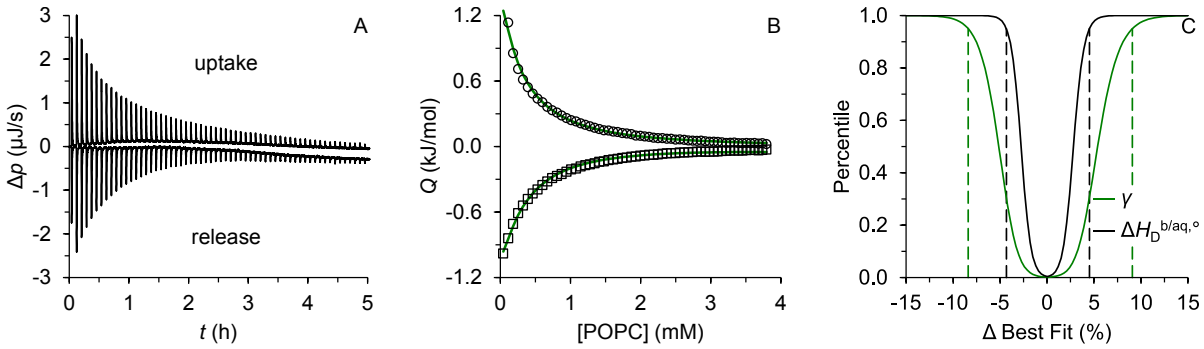

Figure 5.1: ITC uptake and release experiments with POPC and LDAO.
(A) Raw thermograms depicting differential heating power, Δp, versus time, t. (B) Isotherms showing integrated and normalized heats of reaction, Q, versus POPC concentration. Experimental data for (open circles) uptake and (open squares) release, and (solid lines) fits as described in [151], yielding an accessibility factor of $\gamma = 1.08$. (C) Percentiles are plotted as a function of the relative deviation from the best-fit value. (Dashed lines) Margins of 95% confidence intervals correspond to $\gamma = 0.98$–1.19, and $\Delta H_{\mathrm{D}}^{\mathrm{b/aq},\circ} = (9.51$–$10.54)$ kJ/mol. Panels A and B adapted from [81] with permission from Elsevier.

5.1.2 Cyclodextrin/Lipid Complexation

A plethora of CyD derivatives lend themselves to detergent extraction. As these are characterized by different ligand selectivities, a CyD derivative needs to be carefully selected for reconstitution trials to avoid unspecific complexation of lipid. For example, randomly methylated β-CyD (MβCD), which is frequently used for the transfer of cholesterol from or into lipid bilayers [160], is known to form an inclusion complex with POPC [161, 162] and, hence, was deemed to be of limited use for subsequent reconstitution trials. Therefore, the more hydrophilic CyD derivative HPβCD was considered for detergent extraction. A solubilization assay was performed to rule out unspecific complexation of lipid by HPβCD and to compare its lipid-solubilizing capacity to that of MβCD. To this end, the intensity of scattered light upon titration of LUVs into CyD solutions was monitored (Section 3.3.5). In this assay, a shift in the increase in scattering intensity to higher lipid concentrations is indicative of vesicle solubilization by CyD and, hence, formation of a CyD/lipid complex.

The complexation of POPC by MβCD, which has already been demonstrated [161, 162], was reproduced in the solubilization assay (Fig. 5.2, black circles). Solubilization of vesicles comprising the shorter-chain lipid 1,2-dilauroyl-*sn*-glycero-3-phosphocholine (DLPC) was even more pronounced, and an increase in light scattering intensity could not be observed for

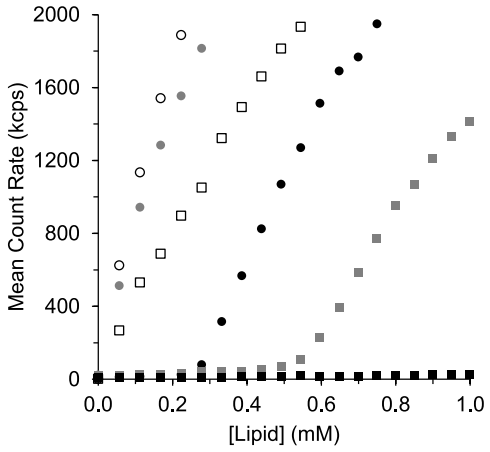

Figure 5.2: Lipid complexation by CyDs.
Formation of CyD/lipid inclusion complexes was assessed by monitoring the intensity of light scattered at 90° during titration of various CyD derivatives with lipid vesicles. A steep increase in mean count rate indicates presence of vesicles. (Open circles) POPC to buffer, (open squares) DLPC to buffer, (gray circles) POPC to 50 mM HPβCD, (gray squares) DLPC to 50 mM HPβCD, (black circles) POPC to 50 mM MβCD, (black squares) DLPC to 50 mM MβCD. In all experiments, the titrant contained the same CyD concentration as the titrand to maintain a constant CyD concentration. Figure adapted from [81] with permission from Elsevier.

even up to 4 mM DLPC (not shown). This result suggests that the lipid-solubilizing capacity of CyDs increases with decreasing acyl chain length. A CyD/lipid complex also formed between DLPC and HPβCD, albeit with lower affinity than for MβCD, as becomes evident from an increase in light scattering intensity above 0.5 mM DLPC (Fig. 5.2, gray squares). Most importantly, no shift in the increase in scattering intensity was observed for the titration of POPC to HPβCD as compared to the buffer control.

In conclusion, HPβCD was chosen for CyD-mediated LDAO extraction in the presence of POPC because of its superior binding selectivity as compared with MβCD. In addition, HPβCD allows for higher concentrations of CyD stock solutions because it is more soluble than MβCD owing to its hydroxypropyl moieties. The solubility of HPβCD is >600 mg/mL as compared with >500 mg/mL for MβCD in pure water at 25°C [163]. However, the solubilization assay also suggested inapplicability of DLPC to HPβCD-mediated detergent extraction.

5.2 Parameters Describing Linked Equilibria in HPβCD/POPC/LDAO Mixtures

With appropriate compounds at hand, the parameters characterizing the linked equilibria in a ternary HPβCD/POPC/LDAO reconstitution mixture were determined by ITC. These

parameters included the critical micelle concentration (CMC) of LDAO, $R_D^{b,SAT}$ and $R_D^{b,SOL}$ from the POPC/LDAO phase diagram, and $K_D^{i/aq}$ for the HPβCD/LDAO inclusion complex.

5.2.1 HPβCD/LDAO Binding

A calorimetric binding experiment (Sections 3.3.2.2 and 4.3) was performed to determine the dissociation constant of the inclusion complex formed by LDAO and HPβCD, $K_D^{i/aq}$ (Fig.5.3). From a NLSF with SEDPHAT [120] (Fig. 5.3 B) according to a one-site binding model, the stoichiometric formation of a 1:1 inclusion complex was confirmed, with $\Delta H_D^{i/aq,\circ} = (5.28 \pm 0.1)$ kJ/mol and $K_D^{i/aq} = (0.10 \pm 0.01)$ mM, which is comparable to the dissociation constant for the inclusion complex of HPβCD and the cationic detergent dodecyltrimethylammonium chloride (0.18 mM, [164]). The latter contains an alkyl chain of 12 carbon atoms just like LDAO, which suggests a minor influence of headgroup charge on inclusion complex stability.

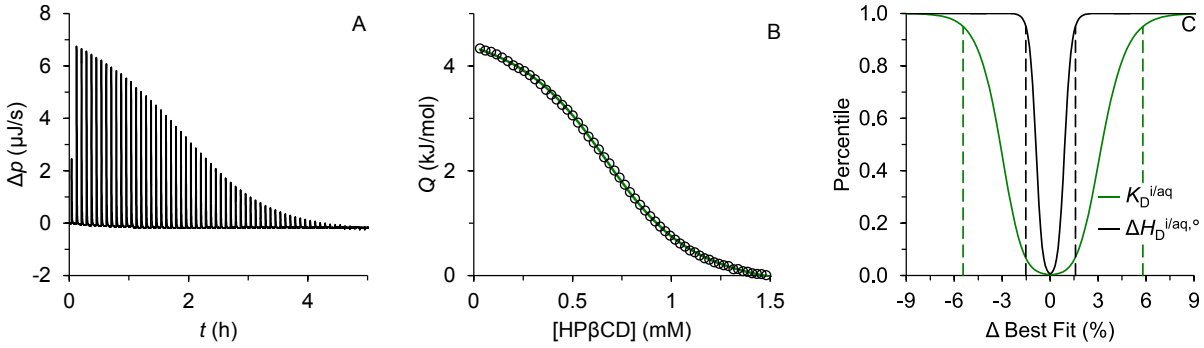

Figure 5.3: Determination of $K_D^{i/aq}$ for the binding of LDAO to HPβCD.
(A) Raw thermogram depicting differential heating power, Δp, versus time, t. (B) Isotherm showing integrated and normalized heats of reaction, Q, versus HPβCD concentration. (Open circles) Experimental data and (solid line) fit according to a single-site binding model as described in [121], yielding a dissociation constant of $K_D^{i/aq} = 0.10$ mM. (C) Percentiles are plotted as a function of the relative deviation from the best-fit value. (Dashed lines) Margins of 95% confidence intervals correspond to $K_D^{i/aq} = 0.097$–0.108, and $\Delta H_D^{i/aq,\circ} = (5.18$–$5.38)$ kJ/mol. Panels A and B adapted from [81] with permission from Elsevier.

To allow for a comparison between HPβCD and bio-beads as to their performance in detergent removal, the adsorptive capacity of bio-beads for LDAO was investigated (see Section 3.3.1.2 and Fig. 5.4). The binding capacity was determined to (0.45 ± 0.04) mmol LDAO per gram dry beads corresponding to (103 ± 10) mg LDAO per gram dry beads, which is comparable to that for dodecyl maltoside or hecameg [68]. At infinitely high binding affinity, that is, $K_D^{i/aq} = 0$ mM, HPβCD would be able to bind $1/M_{HP\beta CD} = 0.65$ mmol LDAO per gram, given an average molecular weight of HPβCD of $M_{HP\beta CD} = 1.54$ g/mmol. Given the

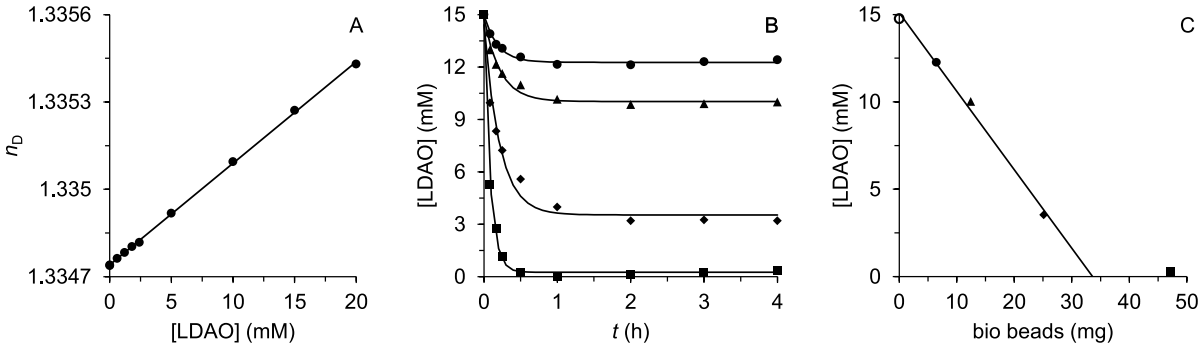

Figure 5.4: Binding capacity of bio-beads for LDAO.
(A) Determination of differential index of refraction for LDAO dissolved in buffer. Refractive index at 20°C plotted versus LDAO concentration. A linear least-squares fit yielded $\mathrm{d}n/\mathrm{d}c = 3.5 \cdot 10^{-2}$ M^{-1}. (B) Binding of LDAO by bio-beads over time. The residual LDAO concentration after addition of (circles) 6, (triangles) 12, (diamonds) 25, and (squares) 47 mg bio-beads to 15 mM LDAO as determined with the $\mathrm{d}n/\mathrm{d}c$ value obtained from A and (lines) negative exponential fits to the experimental data. (C) Final LDAO concentration reached 2–4 h after bio-bead addition versus amount of bio-beads added. A linear least-squares fit yielded a binding capacity of bio-beads for LDAO of (0.45 $\pm$ 0.04) mmol LDAO per gram dry beads, assuming a constant binding capacity at low bead/detergent ratios. The binding kinetics for 47 mg bio-beads was excluded from the fit because complete binding was reached in this case.

dissociation constant of $K_D^{i/aq} = 0.10$ mM for the CyD/LDAO inclusion complex, 0.44 mmol LDAO would be sequestered by one gram HPβCD at equimolar concentrations of HPβCD and LDAO of 0.65 mM, which is similar to the binding capacity of bio-beads. Nevertheless, at higher concentrations the fraction of CyD-complexed LDAO increases.

5.2.2 LDAO Demicellization

The CMC of LDAO was obtained by injecting LDAO micelles into buffer in the course of a demicellization titration (Sections 3.3.2.3 and 4.4). The results of this experiment are shown in Figure 5.5. At the beginning of the titration, the injected micelles dissociated into monomers, whereas at the end of the titration disintegration of micelles had ceased. Accordingly, the heat of demicellization and the heat of dilution together gave rise to the sigmoidal shape of the isotherm (Fig. 5.5 B). As detailed in Section 4.4, the CMC of LDAO was extracted from the isotherm by a two-step analysis to CMC = (1.80 ± 0.02) mM, and the molar micellization enthalpy amounted to $\Delta H_D^{m/aq,\circ} = (8.9 \pm 0.3)$ kJ/mol. The obtained CMC of LDAO is in agreement with literature values refering to similar conditions [105, 165, 166].

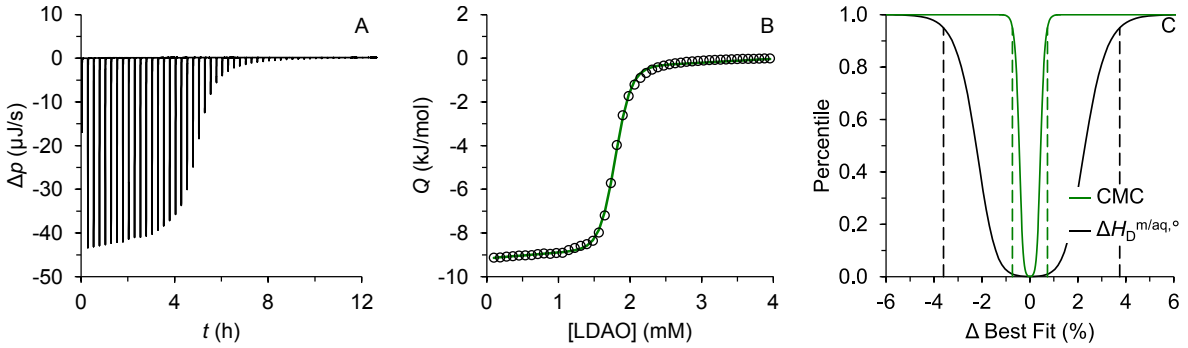

Figure 5.5: Determination of the CMC of LDAO by ITC demicellization.
(A) Raw thermogram depicting differential heating power, Δp, versus time, t. (B) Isotherm showing integrated and normalized heats of reaction, Q, versus LDAO concentration. (Open circles) Experimental data and (solid line) fit as described in [153], yielding a CMC of 1.80 mM. (C) Percentiles are plotted as a function of the relative deviation from the best-fit value. (Dashed lines) Margins of 95% confidence intervals correspond to CMC = (1.78–1.81) mM, and $\Delta H_{\mathrm{D}}^{\mathrm{m/aq,\circ}}$ = (8.6–9.2) kJ/mol. Panels A and B adapted from [81] with permission from Elsevier.

5.2.3 POPC/LDAO Phase diagram

For establishing the POPC/LDAO phase diagram, a series of solubilization (Fig. 5.6) and reconstitution (Fig. 5.7) experiments were performed by titrating micellar LDAO to a suspension of POPC-LUVs with diameters of ∼170 nm and vice versa, respectively (Section 3.3.2.4). Similar to other examples for this type of experiment [122, 143, 150, 156, 167], solubilization isotherms were initially characterized by the disintegration of micelles and the transfer of LDAO monomers into the lipid bilayer giving rise to net endothermic heats at POPC concentrations > 3 mM (Fig. 5.6). An abrupt change to large exothermic heats marked the saturation (SAT) boundary, which was followed by a plateau region that reflects the coexistence range in which, according to the pseudophase model, further addition of detergent increases the number of mixed micelles at the expense of mixed vesicles while their respective composition remains unaffected. As the solubilization (SOL) boundary was reached, a sudden decrease in exothermic heats occurred. The overall reverse shape of reconstitution isotherms (Fig. 5.7B, D, F, H) reflects the fact that the reconstitution process can be considered the mirror image of solubilization. In the regions covering the micellar range at the beginning of reconstitution isotherms, an additional peak in the experimental heat was observed at larger overall concentrations. This peak likely stems from a sphere-to-rod transition of mixed POPC/LDAO micelles [152]. Tubular mixed micelles comprising LDAO have already been observed for reconstitution of CD40 [95] and upon solubilization of 1,2-Dioleoyl-*sn*-glycero-3-phosphocholine (DOPC) bilayers [168]. However, this peak did not impede analysis as care was taken not to mistake its edges for phase boundaries. From the first derivatives of all isotherms, extrema within the transition regions

allowed for the extraction of phase boundary cross points for the construction of the phase diagram (Fig. 5.8).

The linear least-squares fits to the points in the phase diagram that correspond to the two phase boundaries yielded $R_D^{b,SAT} = 1.39$ (1.33–1.44) and $R_D^{b,SOL} = 2.62$ (2.53–2.83) for the slopes of the phase boundaries, with $c_D^{aq^\circ} = 1.40$ mM ((1.39–1.43) mM) for the common ordinate intercept. Reconstitution experiments suggest slightly higher slopes of both SAT boundary ($\Delta R_D^{b,SAT} \approx 8\%$) and SOL boundary ($\Delta R_D^{m,SOL} \approx 12\%$) than solubilization experiments (Fig. 5.8). This observation cannot be ascribed to hysteresis [56], which would rather result in a right-shift of phase-boundary cross points. Too fast rates of titrant addition would require higher detergent concentrations to reach the phase boundaries upon solubilization, whereas a higher detergent concentration would be retained by the vesicles during reconstitution. Nevertheless, the deviation corresponds to an apparent left-shift of phase-boundary cross points in both solubilization and reconstitution experiments of <0.5 mM titrant or to a left-shift of 1–2 out of 75 injections and, thus, is small. To account for the observed uncertainty of phase boundaries nevertheless, error margins for the phase boundaries were estimated by fitting data from either solubilization or reconstitution experiments individually. It should also be noted that the transitions in the isotherms occur over narrow but finite titrant concentration ranges rather than at a single titrant concentration. This is similar to the demicellization process, which also extends over a finite concentration range, thus complicating determination (or even definition) of the CMC [153]. This uncertainty was accounted for by considering the titrant concentration ranges in which the first derivatives of the isotherms deviate by less than 10% from their extrema (Fig. 5.6 and 5.7, shaded regions).

Another factor one needs to bear in mind is that the presence of a membrane protein (MP) might have a profound influence on the location of the phase boundaries. This has been observed, for instance, for the reconstitution of the potassium ion channel KcsA from octylglucoside micelles into *E. coli* polar lipid extract bilayers [62]. In this case, the deviations of the experimental phase boundaries from those predicted on the basis of the simple lipid/detergent mixtures were attributed to incomplete reconstitution and precipitation of the protein. To exclude a similar effect by Mistic on the POPC/LDAO phase diagram, multiple reconstitution experiments similar to those shown in Fig. 5.7 were repeated in the presence of 25 μM Mistic, and the extracted phase-boundary cross points were compared with the phase diagram (Fig. 5.8, open circles). Only a minute contraction of the coexistence range and a virtually identical ordinate intercept were observed as compared with the phase diagram determined in the absence of Mistic, suggesting a negligible influence of Mistic on the phase diagram.

From the slopes of the phase boundaries and the ordinate intercept, the molar fractions of LDAO in detergent-saturated bilayers and in lipid-saturated micelles were calculated according

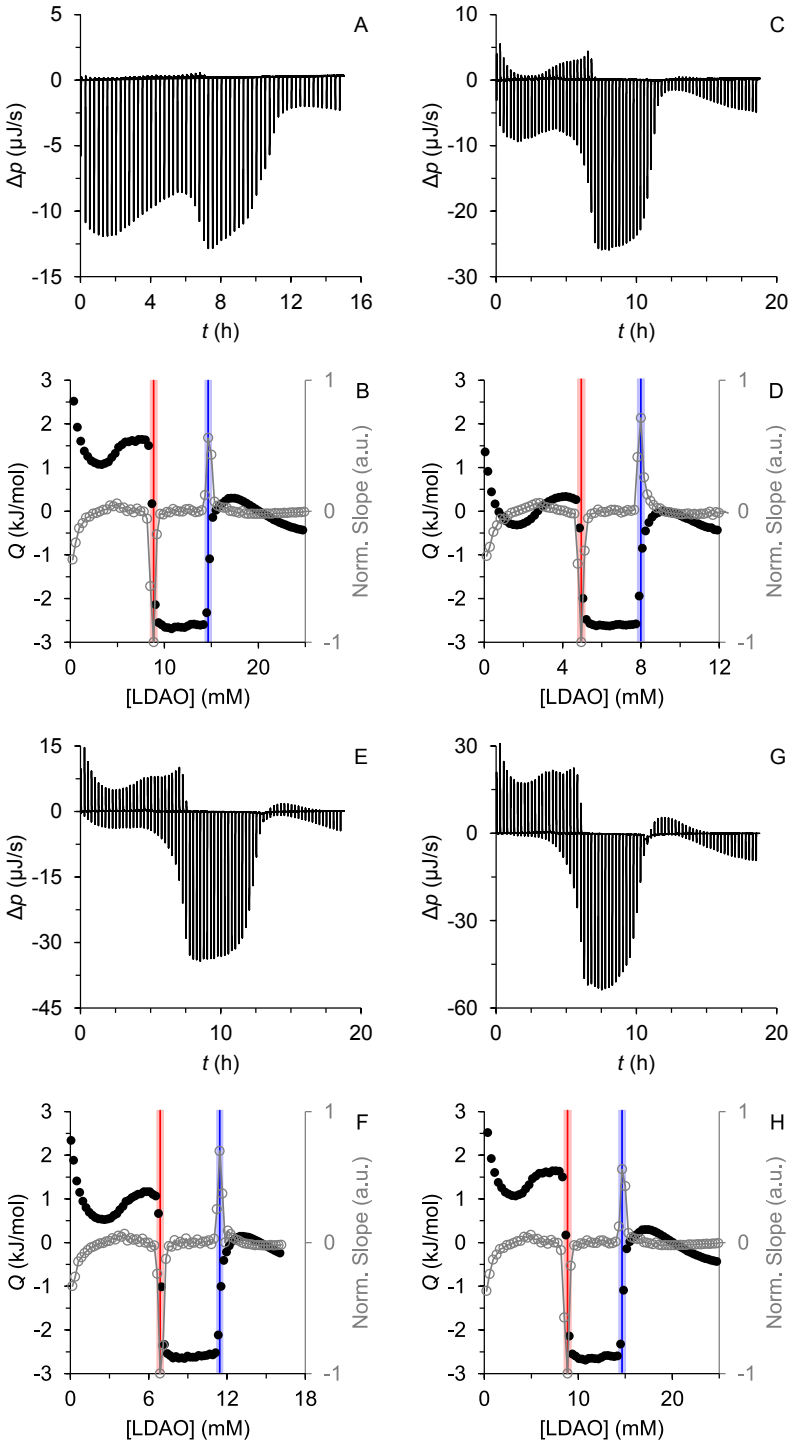

Figure 5.6: Determination of phase boundaries by ITC solubilization experiments.
For solubilization, (A, B) 30 mM, (C, D) 65.5 mM, (E, F) 85 mM, or (G, H) 131 mM LDAO was titrated to 1 mM, 3 mM, 4.5 mM, or 6 mM POPC vesicles, respectively. (A, C, E, G) Raw thermograms depicting differential heating power, Δp, versus time, t. (B, D, F, H) Isotherms showing integrated and normalized heats of reaction, Q, versus LDAO concentration. Shown are (filled black circles) experimental data and (open gray circles) corresponding numeric first derivatives as functions of titrant concentration together with (SOL, blue) solubilization and (SAT, red) saturation boundaries derived therefrom. (Shaded bands) Uncertainties of phase boundaries correspond to the titrant concentration range over which the first derivative of the isotherm deviates by less than 10% from its extremum. Panels G and H adapted from [80] with permission from Elsevier.

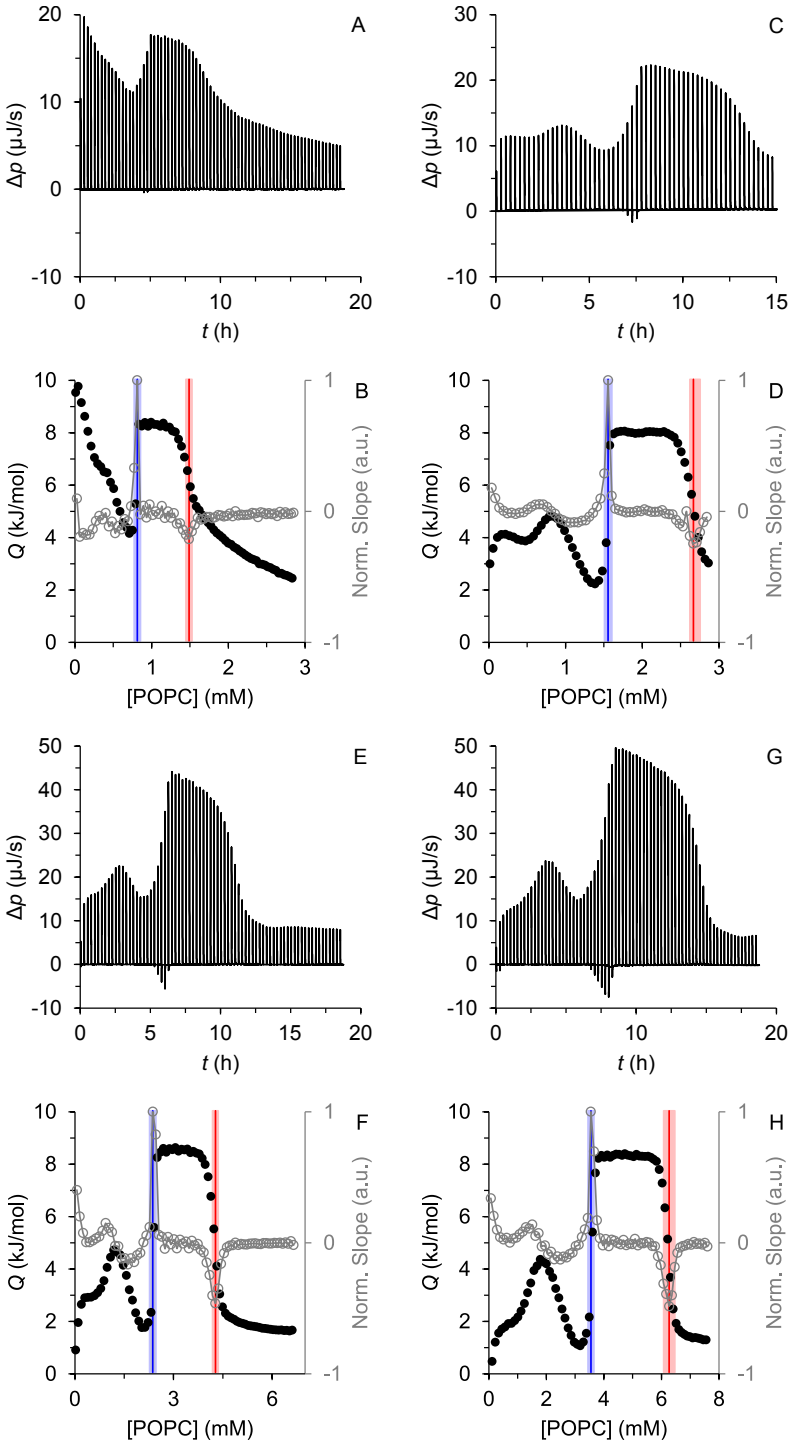

Figure 5.7: Determination of phase boundaries by ITC reconstitution experiments.
For reconstitution, (A, B) 15 mM, (C, D) 15 mM, (E, F) 35 mM, or (G, H) 40 mM POPC vesicles were titrated to 4 mM, 6 mM, 9 mM, or 13 mM LDAO, respectively. (A, C, E, G) Raw thermograms depicting differential heating power, Δp, versus time, t. (B, D, F, H) Isotherms showing integrated and normalized heats of reaction, Q, versus POPC concentration. Shown are (filled black circles) experimental data and (open gray circles) corresponding numeric first derivatives as functions of titrant concentration together with (SOL, blue) solubilization and (SAT, red) saturation boundaries derived therefrom. (Shaded bands) Uncertainties of phase boundaries correspond to the titrant concentration range over which the first derivative of the isotherm deviates by less than 10% from its extremum. Panels E and F adapted from [80] with permission from Elsevier.

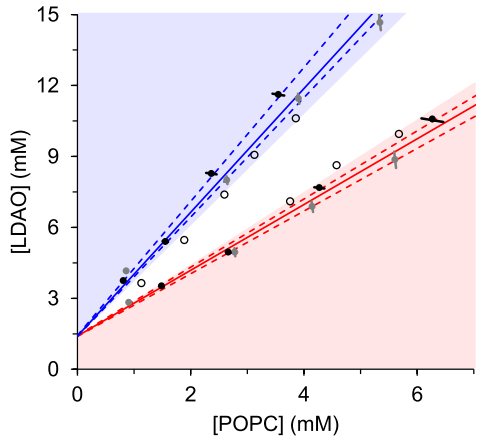

Figure 5.8: POPC/LDAO phase diagram.
Experimental data obtained by plotting LDAO concentrations against corresponding POPC concentrations at the inflection points showing up in (gray circles) solubilization and (black circles) reconstitution titrations and linear fits to (red and blue solid lines, respectively) SAT and SOL boundaries with shared ordinate intercept. (Black and gray error margins) Uncertainties for individual data points were derived from the widths of the transition regions in the corresponding isotherms, while (dashed lines) uncertainties for phase boundaries were estimated by fitting data from either solubilization or reconstitution experiments alone. The phase ranges obtained from (open circles) reconstitutions in presence of 25 μM Mistic are depicted by colored areas. Figure adapted from [80] with permission from Elsevier.

to Eqs. 4.22 and 4.23 as $X_{\mathrm{D}}^{\mathrm{b,SAT}} = 0.58\ (0.57–0.59)$ and $X_{\mathrm{D}}^{\mathrm{b,SOL}} = 0.72\ (0.72–0.74)$, respectively. In addition, the partition coefficients for the transfer of LDAO and POPC from the micellar phase into the bilayer phase together with the corresponding standard molar Gibbs free energies of transfer were determined on the basis of these parameters (Tab. 5.1).

The partition coefficient for the transfer of LDAO between aqueous phase and bilayer phase obtained from the phase diagram, $P_{\mathrm{D}}^{\mathrm{b/aq}} = 23.0 \times 10^3$, is smaller by a factor of ∼3 than that from uptake and release experiments with $P_{\mathrm{D}}^{\mathrm{b/aq}} = 62.8 \times 10^3$ (Section 5.1.1). This discrepancy originates from non-ideal mixing of detergent and lipid resulting in detergent-induced changes of the bilayer phase, which limits the assumption of a constant mole fraction partition coefficient to high lipid/detergent ratios [152]. This condition is given for the uptake and release experiments, but not for the reconstitution and solubilization experiments. Thus, these two sets of experiments are better compared on the basis of a molar ratio partition coefficient. With Eq. 4.8, $K_{\mathrm{D}}^{\mathrm{b/aq}}$ was calculated with $P_{\mathrm{D}}^{\mathrm{b/aq}}$ and $R^{\mathrm{b}} = R_{\mathrm{D}}^{\mathrm{b,SAT}}$ from the phase diagram to $K_{\mathrm{D}}^{\mathrm{b/aq}} = 0.99\ \mathrm{mM}^{-1}$, which is close to the value obtained by uptake and release experiments, $K_{\mathrm{D}}^{\mathrm{b/aq}} = 1.17\ \mathrm{mM}^{-1}$.

A compilation of all thermodynamic parameter values determined by ITC to describe the linked equilibria between HPβCD, POPC, and LDAO can be found in Table 5.1.

Table 5.1: Thermodynamic parameter values derived from ITC experiments at 25°C

Experiment	C	$p1 \rightarrow p2$	$E_C^{p2/p1}$	$\Delta G_C^{p2/p1,\circ}$(kJ/mol)	$\Delta H_C^{p2/p1,\circ}$(kJ/mol)	$-T\Delta S_C^{p2/p1,\circ}$(kJ/mol)
Uptake/Release	D	aq → b	62.8×10^3	–27.4	10.02	–37.4
			(59.7×10^3 to 66.0×10^3)	(–27.3 to –27.5)	(9.51 to 10.54)	(–36.8 to –38.1)
LDAO	D	aq → m	30.8×10^3	–25.6	8.92	–34.6
demicellization			(30.7×10^3 to 31.1×10^3)	(–25.6 to –25.7)	(8.60 to 9.24)	(–34.2 to –34.9)
POPC/LDAO	D	aq → b	23.0×10^3	–24.9		
phase diagram			(22.8×10^3; 22.9×10^3)	(–24.9; –24.9)		
	D	m → b	0.804 (0.796; 0.799)	0.541 (0.566; 0.556)		
	L	m → b	1.51 (1.52; 1.57)	–1.03 (–1.03; –1.12)		
HPβCD/LDAO	D	aq → i	102 μM	–22.8	5.28	–28.1
binding			(96.8 to 108.3 μM)	(–22.6 to –22.9)	(5.18 to 5.38)	(–28.0 to –28.1)

$E_C^{p2/p1}$ denotes an equilibrium constant. For the binding experiment, $E_C^{p2/p1}$ is the dissociation constant. For all other experiments, $E_C^{p2/p1}$ corresponds to the partition coefficient for the transfer of component C from pseudophase *p1* to pseudophase *p2*. For uptake/release experiments, the molar fraction partition coefficient is given as well as for the phase digram, although non-ideal mixing affects the latter. Standard molar Gibbs free energies, $\Delta G_C^{p2/p1,\circ}$, were calculated according to $\Delta G_C^{p2/p1,\circ} = -RT\ln E_C^{p2/p1}$. Entropic contributions were calculated according to $\Delta G_C^{p2/p1,\circ} = \Delta H_C^{p2/p1,\circ} - T\Delta S_C^{p2/p1,\circ}$. The precision of parameter values derived from fits to uptake/release, demicellization, and binding experiments is expressed in terms of the width of 95% confidence intervals. Error margins for phase diagram parameters were derived from individual fits of the phase boundaries to either solubilization or reconstitution data. Because of correlations between the ordinate intercept and the slopes of both the SAT and SOL boundaries, the values of the partition coefficients derived from only solubilization or only reconstitution data do not bracket the best-fit value obtained from a simultaneous fit to all data. Table adapted from [80] with permission from Elsevier.

5.3 Real-Time Monitoring of Mistic Reconstitution

Real-Time Monitoring by ITC After the establishment of model parameter values that characterize the linked equilibria in a ternary HPβCD/POPC/LDAO mixture, the model was tested by comparing the predicted phase transitions with those observed in calorimetric experiments. The results of a representative experiment are shown in Figure 5.9. ITC is ideally suited for monitoring the reconstitution process in real time as to its high sensitivity [62]. Reconstitution by CyD-mediated detergent extraction was performed by titrating HPβCD into mixed micelles composed of 3 mM POPC and 12 mM LDAO in a series of 60 injections (Section 3.3.2.5). Concentrations of components were chosen on the basis of the model while aiming at a rather broad coverage of the coexistance range to identify phase boundaries with appropriate resolution. The expected reconstitution trajectory for the given concentrations was calculated in advance (Fig. 5.9 A) and the process was monitored by ITC (Fig. 5.9 B). An excellent agreement of the experimentally observed phase boundaries with those predicted is apparent from the corresponding isotherm (Fig. 5.9 C).

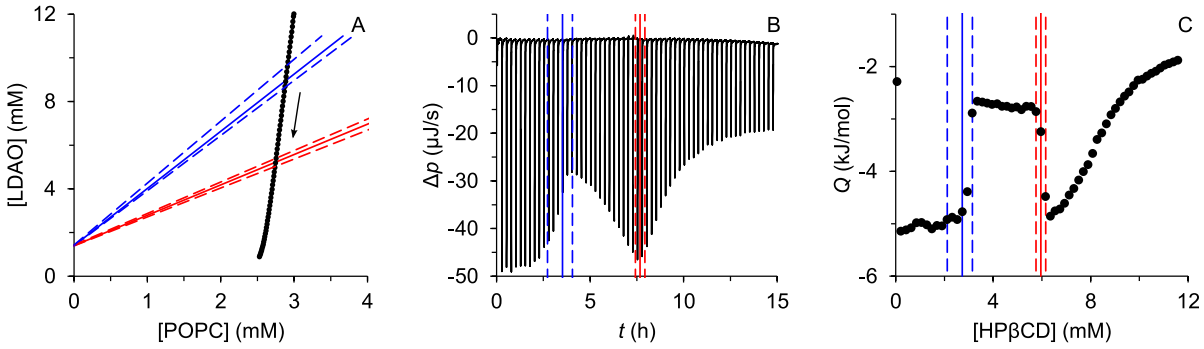

Figure 5.9: Real-time monitoring of CyD-driven reconstitution by ITC.
(A) POPC/LDAO phase diagram with reconstitution trajectory as calculated on the basis of the quantitative model. Each point of the trajectory corresponds to a single injection of titrant. (B) Raw thermogram depicting differential heating power, Δp, versus time, t. (C) Integrated heats of reaction, Q, versus HPβCD concentration as monitored by ITC. 75 mM HPβCD was titrated into a binary mixture of 3 mM POPC and 12 mM LDAO in a series of 60 injections. SOL and SAT boundaries as predicted by the quantitative model are indicated by blue and red vertical solid lines, respectively. Error margins of phase boundaries are denoted by vertical dashed lines. Panels B and C adapted from [80] with permission from Elsevier.

Following reconstitution in the absence of protein, the phase boundaries encountered in the course of CyD-mediated detergent extraction were investigated in the presence of Mistic (Fig. 5.10). To allow for a decent signal in a subsequent circular dichroism (CD) measurement, on the one hand, and to avoid excessive light scattering, on the other hand, a protein concentration of 70 μM at a molar lipid/protein ratio (LPR) of 200 was chosen. Thus, over-

all concentrations needed to be higher than in reconstitutions without Mistic. HPβCD was titrated into a ternary micellar reconstitution mixture composed of Mistic, POPC, and LDAO (Section 3.3.2.5). The transition regions in the resulting isotherm were less sharp than but still clearly reminiscent of those observed in the absence of Mistic (Fig. 5.10 A). Within experimental error, the predicted phase boundaries coincide with the transition regions in the isotherm, implying that the presence of Mistic has no significant influence on the supramolecular state of the system in the course of CyD-mediated reconstitution, as had previously been demonstrated for reconstitution without CyD (Section 5.2.3).

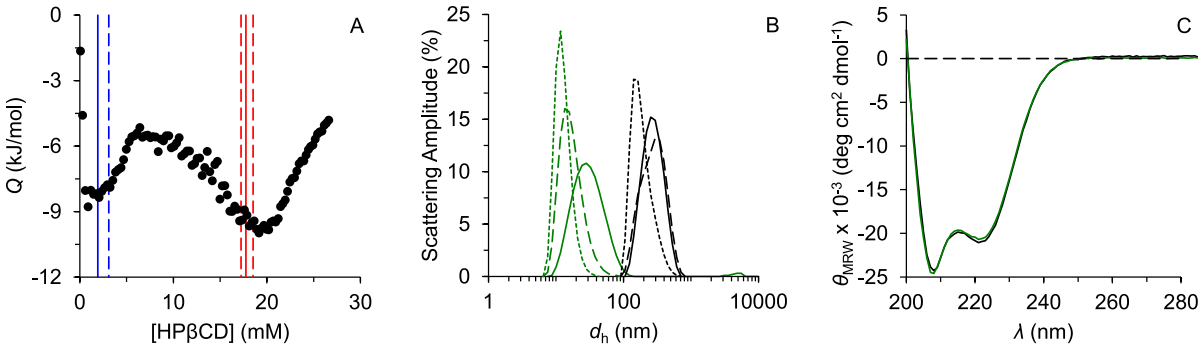

Figure 5.10: Real-time monitoring of Mistic reconstitution by ITC.
(A) Integrated heats of reaction, Q, versus HPβCD concentration as monitored by ITC. 149 mM HPβCD was titrated into a ternary mixture of 70 µM Mistic, 14 mM POPC (LPR = 200), and 40 mM LDAO in the presence of 5 mM DTT in a series of 100 injections. SOL and SAT boundaries as predicted by the quantitative model are indicated by blue and red vertical solid lines, respectively. Error margins of phase boundaries are denoted by vertical dashed lines. (B) Aggregational state before and after reconstitution as determined by DLS. Size distribution (green) before and (black) after reconstitution weighted by (solid lines) intensity, (dashed lines) volume, and (dotted lines) number versus hydrodynamic diameter, d_h. (C) Confirmation of structural integrity of Mistic by CD spectroscopy. Normalized CD spectra (green) before and (black) after reconstitution are shown as normalized mean residue molar ellipticity, θ_{MRW}, versus wavelength, λ. Figure adapted from [80] with permission from Elsevier.

The integrity of proteoliposomes and Mistic secondary structure after reconstitution was verified by dynamic light scattering (DLS) and CD spectroscopy, respectively. DLS revealed a unimodal size distribution and, thus, a uniform aggregational state both before and after reconstitution (Fig. 5.10 B). Prior to reconstitution, there was a single peak corresponding to an average hydrodynamic diameter of ∼30 nm. As lipidfree LDAO/Mistic micelles are <10 nm in size [108], the larger hydrodynamic diameter suggested a nonspherical geometry of lipid/detergent/protein micelles like rod-shaped micelles as observed, for instance, for the fluorinated octyl maltoside F_6OM [155]. Reconstitution was accompanied by a pronounced shift to an average hydrodynamic diameter of ∼250 nm, indicating the formation of large vesicles upon CyD-mediated detergent removal.

The CD spectrum of solubilized Mistic before reconstitution exhibited a double minimum at 208 nm and 222 nm characteristic of a largely α-helical conformation (Fig. 5.10 C). The spectrum after reconstitution, corrected for the small dilution caused by addition of CyD, superimposed virtually perfectly, demonstrating that no protein was lost as a result of aggregation or precipitation and that the secondary structure of Mistic remained unaffected by reconstitution.

Real-Time Monitoring by Fluorescence Spectroscopy The advantage of CyD to be small and spectroscopically inert was exploited by following CyD-mediated reconstitution of Mistic in real time also by fluorescence spectroscopy (Fig. 5.11) and DLS (Fig. 5.12). To avoid too strong a decrease of fluorescence intensity due to the attenuation of both excited and emitted light, fluorescence spectroscopy measurements were performed at a decreased initial lipid concentration of 3 mM POPC, being the same as for the reconstitution without Mistic in Figure 5.9 and, thus, resulting in a similar reconstitution trajectory (Fig. 5.11 A). Accordingly, the protein concentration was reduced to 8 μM Mistic, which afforded an adequate fluorescence signal and corresponded to an LPR of 385. The quantitative model not only allowed for prediction of the reconstitution trajectory but also of the change in concentrations of all components in each pseudophase (Fig. 5.11 B). Mistic contains a single tryptophan residue, W13, the emission maximum of which was expected to shift to lower wavelengths upon reconstitution caused by decreased solvent relaxation in the hydrophobic bilayer environment. Control measurements were performed in the absence of Mistic using *N*-acetyl-L-tryptophanamide (NATA) as a water-soluble chromophore.

As becomes apparent from the series of fluorescence emission spectra, changes in intensity and wavelength of maximum intensity, λ_{max}, differed between the control reconstitution in the presence of NATA (Fig. 5.11 C) and that in the presence of Mistic (Fig. 5.11 D). During CyD-mediated reconstitution of Mistic, a blue-shift of λ_{max} by $\sim$2 nm was observed (Fig. 5.11 E), which reached its minimum value at the SAT boundary. Within the vesicle range, λ_{max} stayed constant. The shift of λ_{max} from 336 nm to 334 nm is a strong indication of Mistic's membrane association because a decrease in λ_{max} for tryptophan fluorescence attests to a decrease in environmental polarity.

For both NATA and Mistic, the overall intensity decreased substantially during reconstitution because of vesicle-induced light scattering. For the purpose of comparison, relative intensities were calculated by dividing the integrated absolute intensities by the initial intensity, I_0. To correct relative intensities of Mistic reconstitution for the attenuation arising from light scattering, they were divided by those of the NATA reconstitution (Fig. 5.11 E, gray squares). In general, tryptophan fluorescence is expected to increase upon reconstitution of a peptide or protein [129]. In accordance, corrected intensity increased for Mistic reconstitution within the

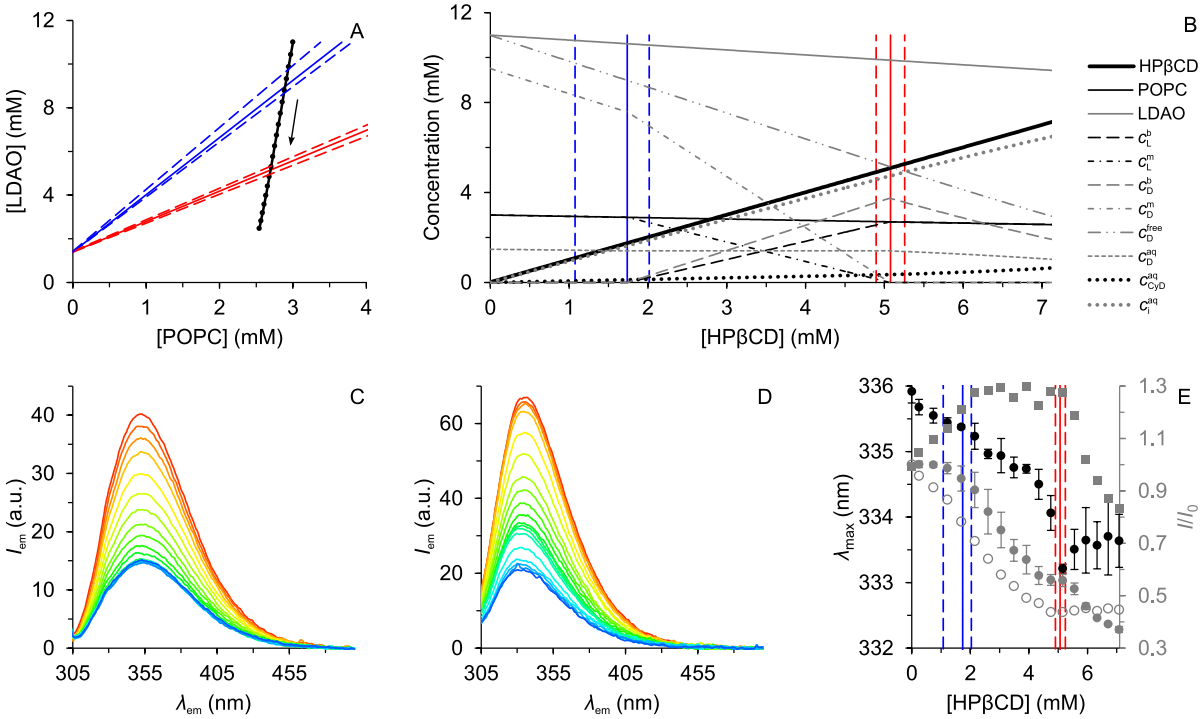

Figure 5.11: Real-time monitoring of Mistic reconstitution by fluorescence spectroscopy. (A) POPC/LDAO phase diagram with reconstitution trajectory and (B) speciation plot as calculated on the basis of the quantitative model for CyD-mediated reconstitution in the presence of (C) 8 µM NATA as control and (D) 8 µM Mistic as (E) monitored by fluorescence spectroscopy. (A) Each point of the trajectory corresponds to a single injection of titrant. 180 µL 50 mM HPβCD were titrated in 18 injections to 1 mL mixed micelles composed of 3 mM POPC (LPR = 385) and 11 mM LDAO in the presence of 5 mM DTT. (B) (Solid lines) Total concentrations and concentrations in (dotted lines) the aqueous phase, (dash-dotted lines) the micellar phase, (dashed lines) the bilayer phase of (thin black lines) POPC, (gray lines) LDAO, and (thick lines) HPβCD as well as the concentrations of (thick gray dotted line) inclusion complex and (dash double-dotted line) free LDAO. (C, D) Emission intensity, I_{em}, is plotted versus emission wavelength, λ_{em} (λ_{ex} = 295 nm). Progression of reconstitution is indicated by rainbow coloring from red to blue. (E) With fluorescence spectroscopy, reconstitution in presence of (open circles) NATA and (filled symbols) Mistic was monitored in terms of (black circles) wavelength at maximum emission intensity, λ_{max}, and (gray circles) emission intensity integrated over 305–500 nm relative to initial intensity, I/I_0. Fluorescence data for Mistic reconstitution is the average of three independent measurements. (Gray squares) Intensity data for Mistic reconstitution were corrected for attenuation due to light scattering by normalizing to that for NATA reconstitution. (B, E) SOL and SAT boundaries as predicted by the quantitative model are indicated by blue and red vertical solid lines, respectively. Error margins of phase boundaries are denoted by vertical dashed lines.

micellar range (Fig. 5.11 E). At the SOL boundary, intensity ceased to increase. The decrease of intensity after reaching the SAT boundary most probably stemmed from increasing light scattering within the vesicle range because of the proceeding increase of the vesicle diameter. The latter was only observed in the presence of Mistic (Fig. 5.12 B, see below) and thus could

not be corrected for with reconstitution data from the NATA control.

It should be noted that a potential complexation of NATA by CyD was not accounted for in the control experiment. Although equilibrium constants for the inclusion complexes between CyD and ligands similar to NATA, such as aromatic amino acids, are two to three orders of magnitude lower than for LDAO [74], complexation of NATA at the high CyD concentration used is likely. However, a blue-shift that would be expected to accompany the binding of NATA to the hydrophobic cavity of CyD was not observed.

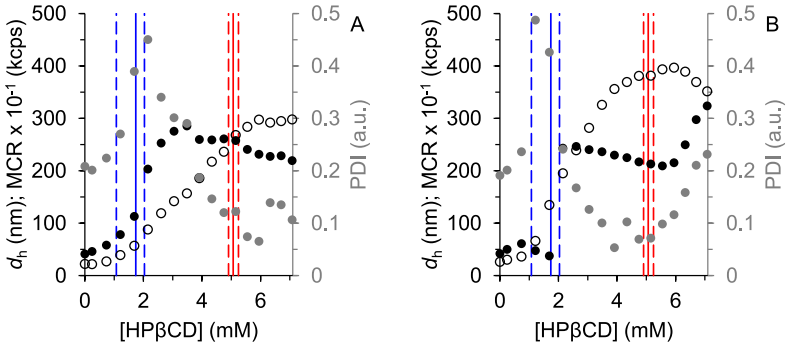

Figure 5.12: Real-time monitoring of Mistic reconstitution by DLS.
CyD-mediated reconstitution (A) in the absence of Mistic and (B) in the presence of 8 μM Mistic as monitored by DLS. Reconstitution was performed likewise to Figure 5.11, hence the same reconstitution trajectory (Fig. 5.11 A) and speciation plot (Fig. 5.11 B) apply. With DLS, reconstitution was monitored in terms of (black circles) mean hydrodynamic diameter, d_h, (gray circles) polydispersity index (PDI), and (open circles) mean count rate (MCR). SOL and SAT boundaries as predicted by the quantitative model are indicated by blue and red vertical solid lines, respectively. Error margins of phase boundaries are denoted by vertical dashed lines.

Real-Time Monitoring by DLS Reconstitution was also monitored by DLS (Fig. 5.12) both in the absence (Fig. 5.12 A) and in the presence of Mistic (Fig. 5.12 B). The same concentrations as for reconstitution monitored by fluorescence spectroscopy were used, and, thus, the same reconstitution trajectory applied (Fig. 5.11 A). When Mistic reconstitution was followed by DLS, the predicted SOL boundary coincided with an increase in both mean count rate (MCR) as well as an increase of the average hydrodynamic diameter, d_h, to ~250 nm, indicative of the formation of vesicles (Fig. 5.12 B). In addition, the SOL boundary was marked by a maximum of the polydispersity index (PDI) because the size distribution became bimodal at the onset of vesicle formation owing to the presence of both micelles and vesicles. The decrease in PDI following the SOL boundary originated in the quickly increasing number of vesicles masking light scattering due to micelles. Likewise, the SAT boundary was unnoticeable by DLS in the absence of protein as the disappearance of micelles was masked by light scattering due

to vesicles. However, the SAT boundary was followed by an increase of both d_h and PDI and by a small decrease in MCR in the presence of Mistic. These changes suggest coalescence of vesicles, as the pairwise fusion of 250-nm vesicles would give rise to the observed increase of d_h to roughly 350 nm (assuming preservation of lipid area) as well as to a broadening of the size distribution.

5.4 Mistic Reconstitution at Different Lipid/Protein Ratios

One fundamental parameter deciding about failure or success of MP reconstitution is the molar lipid/protein ratio (LPR), which is of particular importance for experiments that require high protein concentrations such as nuclear magnetic resonance (NMR) spectroscopy or crystallization [169]. The influence of low LPRs on the outcome of CyD-mediated Mistic reconstitution was investigated by performing reconstitutions at LPRs ranging from 100 to 310 (Section 3.3.2.5). All of these reconstitution were performed at the same Mistic concentration, whereas POPC and LDAO concentrations were varied. LPRs from 100 to 310 correspond to ∼5600 to ∼1800 protein molecules per POPC vesicle assuming an average vesicle diameter of 250 nm and an area per lipid molecule of 0.68 nm^2 [23]. Reconstitutions were monitored with an Auto-iTC_{200} preceded and followed by DLS and CD measurements.

ITC With the help of the quantitative model, trajectories for all reconstitutions followed by ITC were planned in such a way that the different phase ranges were covered by the same numbers of injections during each titration (Fig. 5.13 A). This experimental design aimed at allowing for a direct comparison of titrations in terms of relative titrant concentration. As anticipated, the phase boundaries were reached, within experimental error, after the same number of injections in each titration (Fig. 5.13 B–I). However, the phase boundaries were reached slightly earlier as compared with the model prediction, as becomes most noticeable by the shifted extrema in the first derivatives of the isotherms (Fig. 5.13 B, C). This left-shift occurred systematically in all measurements and corresponds to a deviation of ∼3 µL of titrant. Most probably, this deviation stemmed from excess titrant introduced by the syringe upon transfer into the sample cell within the automated microcalorimeter.

From the thermograms (Fig. 5.13 D, G) and isotherms (Fig. 5.13 E, H) both in the absence and the presence of Mistic, a systematic dependence of the magnitude of heats on overall concentrations was apparent. A change of the LPR by 30 corresponded to a difference in heats by ∼0.23 kJ/mol at the end of the titrations. Nevertheless, the concentrations of all components but the protein were different in each titration, thus pinpointing the origin for the observed differences in heats in terms of partitioning of a particular component was not feasible.

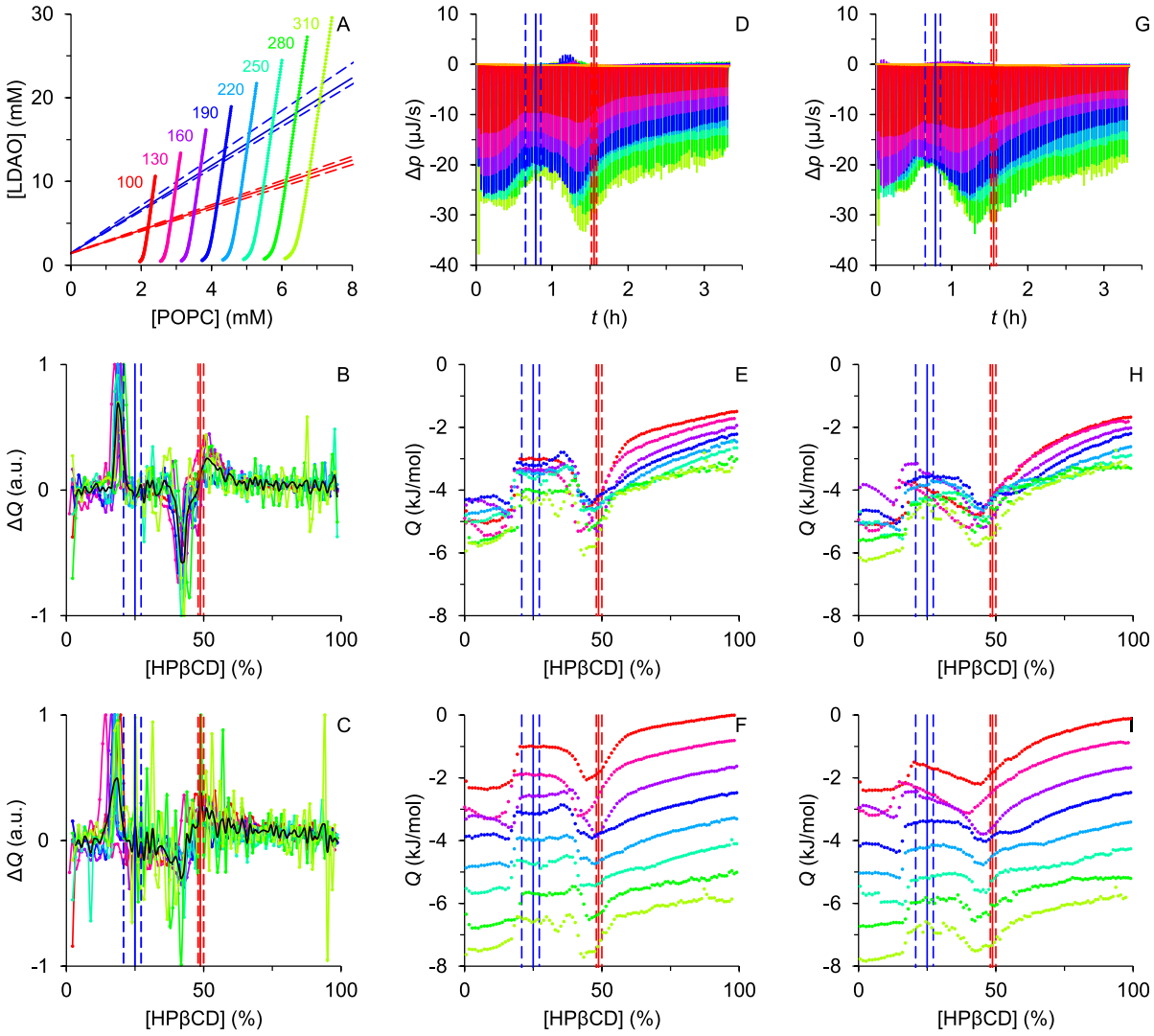

Figure 5.13: HPβCD-mediated reconstitution at different LPRs as monitored by ITC.
(A) Reconstitution trajectories explored in reconstitution experiments. Coloring of trajectories for different LPRs as labeled apply to other panels as well. In all panels, SOL and SAT boundaries as predicted by the quantitative model are indicated by blue and red vertical solid lines, respectively. Error margins of phase boundaries are denoted by vertical dashed lines. (B, D–F) Reconstitutions in the absence and (C, G–I) in the presence of 24 μM Mistic at different LPRs were monitored by ITC. (B, C) Normalized numeric first derivatives of isotherms in E and H as functions of relative HPβCD concentration. Averages of all derivatives are depicted in black. (D, G) Raw thermograms depicting differential heating power, Δp, versus time, t. (E, H) Isotherms showing integrated and normalized heats of reaction, Q, versus relative HPβCD concentration. (F, I) Isotherms as in E and H with offset for clearity.

Whereas the presence of Mistic influenced neither the location of phase boundaries nor the magnitude of overall heats, it indeed altered the appearance of isotherms. Most particularly at low LPRs, in the coexistence range in the absence of Mistic (Fig. 5.13 F), a plateau region was followed by an increase of heats towards the SAT boundary, while heats increased almost linearly throughout the entire coexistence range in the presence of Mistic (Fig. 5.13 I). In addition, the decrease of heats following the SAT boundary was steeper in the absence of Misic. In summary, CyD-mediated reconstitutions of Mistic at different LPRs revealed no substantial disparities in terms of phase boundary locations and calorimetric output.

DLS The aggregational state at different LPRs before and after reconstitutions monitored by automated microcalorimetry was checked by DLS measurements (Fig. 5.14). In the absence of Mistic, unimodal size distributions shifted from $d_h \approx 20$ nm characteristic for mixed micelles to $d_h \approx 250$ nm indicating the formation of vesicles upon CyD-mediated detergent extraction as shown before in Section 5.3 (Fig. 5.14 A–C). However, in the presence of Mistic, multimodal size distributions after reconstitution were indicative of the formation of aggregates (Fig. 5.14 D, E). Aggregates were observed at all LPRs including LPRs of 190 and 220, ratios which were close to that of the reconstitution in Figure 5.10 that lacked a formation of aggregates. Nevertheless, multiple experimental parameters were different including total concentrations, and control over automated sample handling by the Auto-iTC$_{200}$ was limited, hence narrowing down the reason for the formation of aggregates in this series of experiments was hampered. Large aggregates were more apparent in intensity-weighted and volume-weighted size distributions because light scattering intensity is proportional to the sixth power of the particle radius (Fig. 5.14 D, E). A peak at $d_h \approx 250$ nm indicated the presence of proteoliposomes for LPRs >160, and number-weighted size distributions revealed that the amount of aggregates was small (Fig. 5.14 F). In conclusion, LPRs of roughly 200 or higher should be chosen to ensure a negligible amount of aggregates at similar measurement parameters. In any case, assessing the aggregational state of reconstitutions by DLS proved to be indispensable.

CD The stability of Mistic after reconstitution at different LPRs was qualitatively checked by CD spectroscopy (Fig. 5.15). Spectroscopic measurements on reconstituted MPs have proven to be complicated by both differential light scattering and absorption flattening [123, 170–172]. Differential light scattering arises from different refractive indices of the scattering particle for left and right circularly polarized light, n_L and n_R, and occurs in the presence of LUVs because of their large size that is comparable to far-UV wavelengths. This effect leads to an apparent increase or decrease in ellipticity, depending on whether $n_L - n_R$ is positive or negative in a given spectral region. Absorption flattening is a decrease in apparent ellipticity

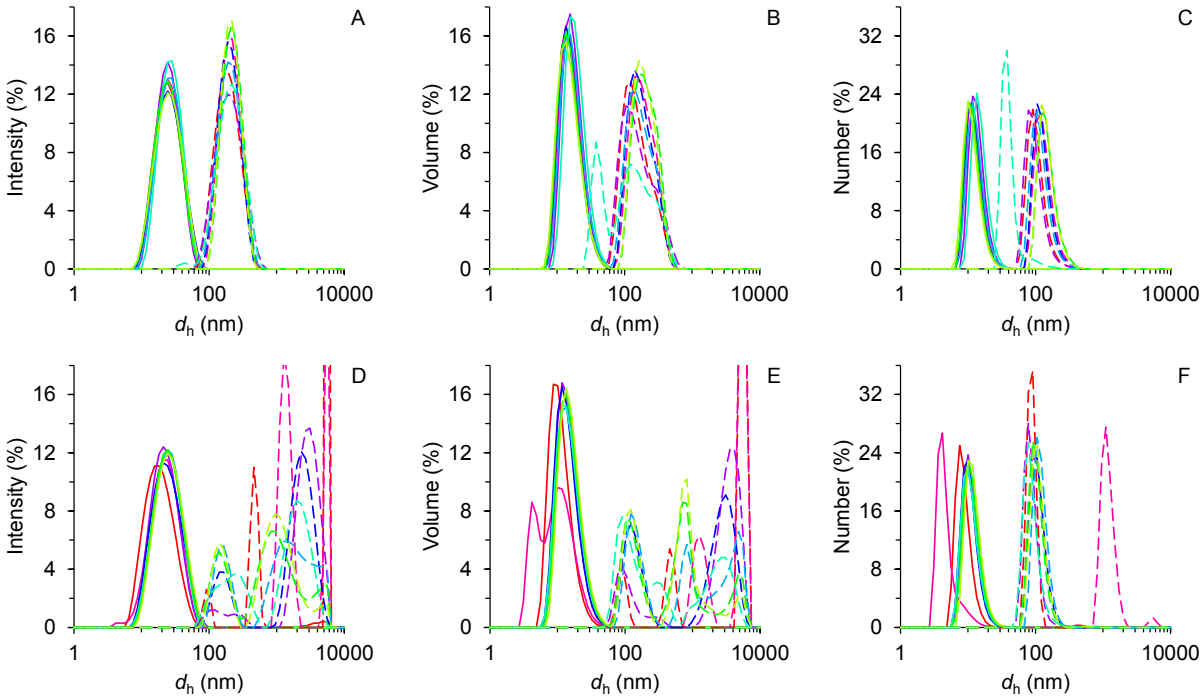

Figure 5.14: DLS experiments for HPβCD-mediated reconstitutions at different LPRs.
DLS experiments (A–C) in the absence and (D–F) in the presence of 24 μM Mistic (solid lines) before and (dashed lines) after reconstitution were performed on the same samples as in Figures 5.13 and 5.15. Plots show light scattering weighted by (A, D) intensity, (B, E) volume, and (C, F) number versus hydrodynamic diameter, d_h. Reconstitutions were performed at different LPRs (red to green for low to high LPRs, respectively; refer to legend in Figure 5.13 A for LPR color indication).

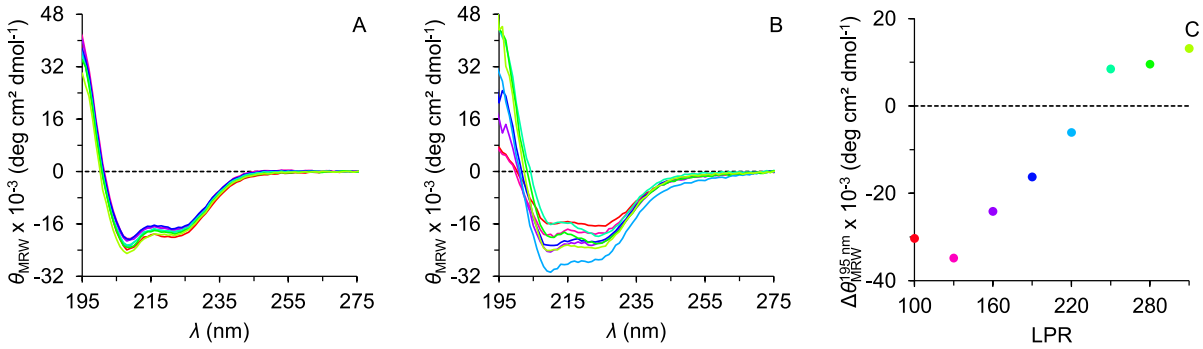

Figure 5.15: CD spectra of Mistic before and after reconstitution at different LPRs.
The secondary structure of Mistic (A) before and (B) after reconstitution as assessed by CD spectroscopy for the same samples as in Figures 5.13 and 5.14. (A, B) Plots show normalized mean residue molar ellipticity, θ_{MRW}, versus wavelength, λ. (C) Difference between normalized mean residue molar ellipticity at 195 nm before and after reconstitution versus LPR to illustrate absorption flattening and differential scattering effects. Reconstitutions were performed at different LPRs (red to green for low to high LPRs, respectively; refer to legend in Figure 5.13 A for LPR color indication).

due to the anisotropic distribution of the absorbing chromophore in the sample. In the case of proteoliposomes, the protein is confined to the lipid bilayer and thus, the probability of incident light to reach a protein molecule is lessened because of the close presence of neighboring proteins.

To take these optical effects into account, CD spectra for reconstituted Mistic were corrected by subtracting spectra for samples containing LUVs in the absence of Mistic at otherwise identical concentrations. However, a correction as this can only account for differential spectroscopic effects if they are comparable for reference and sample, which might not have been the case here as the samples without Mistic lacked large aggregates. Thus, differences between CD spectra before reconstitution (Fig. 5.15 A) and after reconstitution (Fig. 5.15 B) could still arise from changes in secondary structure as well as from differential light scattering and absorption flattening.

After reconstitution, CD signals deviated substantially among spectra for different LPRs, with decreased overall ellipticities for low LPRs of 100 and 130 as compared with those before reconstitution. This could potentially indicate some loss of folded Mistic upon aggregation. Nevertheless, the ratio between CD signals at 208 nm and 222 nm that is indicative for differential changes of ellipticity was substantially decreased at LPRs 100 and 130 and LPRs 250 to 310, suggesting contributions from both scattering, which is expected to be more pronounced at higher lipid concentrations, and absorption flattening, which is expected to be increased at lower LPRs. Absorption flattening becomes most evident for CD bands at strong absorption peaks. As typical for α-helical proteins, the band at 190 nm was expected to have the most intense signal, but detector high tension showed that the detection limit was already reached at this low wavelength. Therefore, to illustrate absorption flattening, the difference between normalized mean residue molar ellipticity at 195 nm before and after reconstitution was plotted versus the LPR (Fig. 5.15 C). This plot reveals a clear tendency of the CD signal at 195 nm to decrease in magnitude upon reconstitution at lower LPRs. These changes most probably arose from absorption flattening and differential scattering because of aggregates, although a minor contribution by rearrangements of secondary structure to the measured CD spectra, albeit not expected, cannot be excluded.

In summary, changes in CD spectra upon Mistic reconstitution can most likely be attributed to absorption flattening and differential scattering effects. Although differentiation between optical artifacts and structural changes is intractable both experimentally and by theoretical conceptualization, overall signal intensities were similar to those before reconstitution suggesting a negligible loss of folded protein due to aggregation.

5.5 Membrane Topology of Mistic

Various fluorescence specroscopic and CD specroscopic approaches were employed to elucidate how Mistic associates with a POPC bilayer. More precisely, the accessibility of Mistic's single tryptophan residue W13 and both the translational position along the bilayer normal and the rotational orientation of reconstituted Mistic were investigated.

5.5.1 Urea Unfolding of Reconstituted Mistic

The conformational stability of Mistic in detergent micelles has already been investigated comprehensively by denaturant-induced unfolding experiments [73, 105]. With such experiments, protein stability is assessed in terms of the Gibbs free-energy change of unfolding, which is obtained from a sigmoidal unfolding isotherm for a two-state equilibrium between folded and unfolded protein by applying a NLSF. The Gibbs free-energy change is linearly dependent on the denaturant concentration within the transition region of the unfolding isotherm and, thus, is extrapolated to the absence of denaturant. The unfolding isotherm also provides information on the sensitivity of the protein against the denaturant in terms of the so-called *m*-value. Likewise, stability and accessibility of Mistic within a POPC bilayer was assessed by urea-induced unfolding of the reconstituted protein monitored by CD spectroscopy (Section 3.3.3.1). The results of these experiments are shown in Figure 5.16. Osmotic effects on vesicle integrity and size due to the addition of urea were not expected [173], which was confirmed by preceding DLS measurements (Fig. 5.16 A).

Canonical MPs residing in a lipid bilayer are usually not amenable to denaturant-induced unfolding [14]. Interestingly, addition of up to 6 M urea to Mistic reconstituted in POPC LUVs clearly gave rise to a decrease in ellipticity (Fig. 5.16 B). Unfortunately, unfolding experiments met technical limits as a pathlength of at least 4 mm was required to allow for tubing access, and, thus, increased high tension of the detector due to light scattering confined the wavelength range amenable to analysis to >225 nm. Owing to the low signal/noise ratio and poorly defined pre- and post-transition baselines, the resulting isotherms allow for reliable determination neither of the Gibbs free energy change of unfolding nor of the *m*-value and the urea concentration at half-maximal unfolding (Fig. 5.16 C), as 99% confidence intervals were in the range of $\pm$ $\sim$100% of the best-fit values. Nevertheless, the fact that a loss of secondary structure resulted from addition of urea indicated a certain accessibility of reconstituted Mistic to the denaturant.

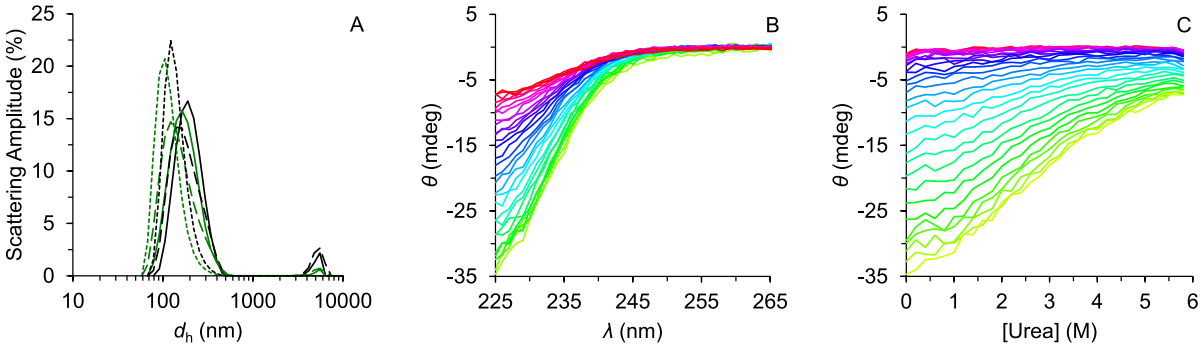

Figure 5.16: Urea-induced unfolding of reconstituted Mistic.
(A) Aggregational state after 1:6 dilution of reconstituted Mistic with (black) buffer and (green) urea as determined by DLS. Osmotic effects due to addition of urea were not observed. Size distribution weighted by (solid lines) intensity, (dashed lines) volume, and (dotted lines) number versus hydrodynamic diameter, d_h. (B) CD spectra of 6.5 µM Mistic in POPC vesicles at LPR 200 in the presence of (green to red) 0–5.8 M urea, plotted as ellipticity, θ, versus wavelength, λ. (C) Unfolding isotherms depicting θ versus urea concentration at wavelengths (green to red) 225–255 nm. Different line depictions in panel A refer to replicates of reconstitutions. Panels B and C show averaged data from three titration replicates.

5.5.2 Acrylamide Quenching in Hydrophobic Environments

The degree of exposure of Mistic's single tryptophan residue W13 in dependence of different hydrophobic environments was investigated by acrylamide quenching (Section 3.3.4.1). Shielding due to detergent micelles was compared to that invoked by reconstitution within a POPC bilayer. Detergents used for solubilization included a homologous series of alkyl maltosides, namely OM, DM, and DDM bearing alkyl chains of 8, 10, and 12 carbon atoms, respectively, as well as LDAO and the alkyl phosphocholine DPC with alkyl chain lengths of 12 carbon atoms.

In general, solvent exposure of W13 is expected to be reduced compared with a water-soluble indole fluorophore like NATA by two reasons. Quencher-accessibility of W13 is reduced by (i) the hydrophobic environment of micelles or vesicles and (ii) the protein scaffold itself, as W13 resides at the N-terminal end of the four-helix bundle of Mistic and is covered by the loop between helices H2 and H3. First, a higher shielding of W13 as compared with NATA becomes apparent from the substantially higher acrylamide quenching efficiency of NATA (Fig. 5.17), which is not expected to interact with detergent micelles at all. Indeed, the quenching efficiency of NATA in the presence of LDAO micelles with $K_{SV} = 15.0 \pm 0.2$ M^{-1} is similar to that of NATA in water, $K_{SV} = 17.5$ M^{-1} [174]. Second, the influence of different hydrophobic environments on W13 exposure becomes evident by the differential reduction in quenching efficiency in micelles of various compositions (Fig. 5.17). The detergents with zwitterionic headgroups, LDAO and DPC, gave rise to the highest quenching constants (Tab. 5.2), whereas

quenching was reduced in micelles composed of detergents with nonionic headgroups. This difference corresponds to lower shielding of W13 in the presence of zwitterionic detergents, which was expected as these are packed less tightly because of increased headgroup repulsion. Interestingly, for the homologous series of alkyl maltoside detergents, a linear decrease of quenching efficiency with alkyl-chain length by 0.5 M^{-1} per methylene group was apparent from the respective quenching constants (Tab. 5.2). For reconstituted Mistic, quenching efficiency was significantly reduced and virtually independent of the reconstitution strategy employed. However, acrylamide quenching suggested higher accessibility of W13 in Mistic when reconstituted in a POPC bilayer as compared with Mistic in DDM micelles.

Stern–Volmer plots were analyzed with the unmodified Stern–Volmer equation, although some of them exhibit somewhat unusual profiles (Fig. 5.17). In particular, the Stern–Volmer plot for Mistic in DM deviates from linearity, as quenching efficiency seems to increase more steeply above 175 mM acrylamide. The same was observed in the plots for the other detergents, albeit less pronounced. It is known that an upward curvature of Stern–Volmer plots might be indicative for a contribution of static quenching [175]. However, the plots appear sigmoid-like rather than upward-curved. This peculiar appearance is quite reminiscent of Stern–Volmer plots obtained for apo glyceraldehyde-3-phosphate dehydrogenase [176]. In the latter case, acrylamide itself had an influence on tryptophan accessibility. Still, the exact reason for the deviation observed remains to be identified.

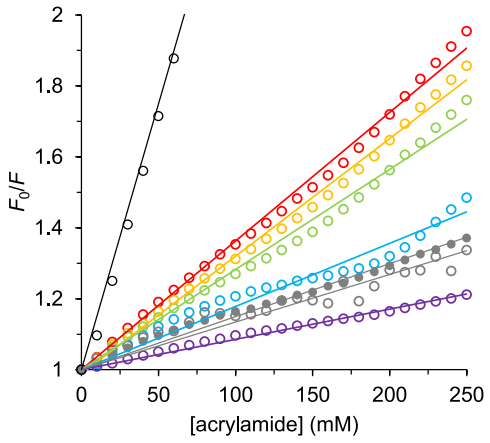

Figure 5.17: Stern–Volmer plot for acrylamide quenching of Mistic.
Acrylamide quenching of (black) NATA in the presence of LDAO micelles and of Mistic solubilized in (red) LDAO, (yellow) DPC, (green) OM, (blue) DM, (purple) DDM micelles, and Mistic reconstituted in POPC bilayers by (gray open circles) CyD-mediated detergent extraction and (gray filled circles) addition to preformed vesicles. Measurements were performed at 25°C in buffer. The ratio of integrated fluorescence intensities in the absence and presence of acrylamide, F_0/F, is plotted versus acrylamide concentration. Lines are linear least-squares fits on the basis of which Stern–Volmer constants were determined.

Table 5.2: Stern–Volmer quenching constants for acrylamide quenching of Mistic

	NATA	Mistic					
	LDAO	LDAO	DPC	OM	DM	POPC (Add / CyD)	DDM
K_{SV} (M^{-1})	15.0	3.63	3.25	2.83	1.78	1.49 / 1.34	0.85
	± 0.2	± 0.06	± 0.05	± 0.06	± 0.07	± 0.03 / ± 0.07	± 0.02

Acrylamide quenching of Mistic W13 was investigated for Mistic in different hydrophobic environments including Mistic reconstituted by both the addition of vesicles (Add) and CyD-mediated detergent extraction (CyD). Precision of K_{SV} as determined by linear regression is expressed in terms of the width of 95% confidence intervals.

5.5.3 Translational Orientation by DDFQ

To elucidate whether Mistic is only peripherally associated with or rather incorporated into a POPC bilayer and, if so, how deeply, the DDFQ technique was used (Section 3.3.4.2). This methodology yields a profile that comprises the distance-dependent quenching efficiencies of a membrane-bound fluorophore obtained in the presence of brominated lipids, the quenching moieties of which are located at different known alkyl chain positions. To validate the performed protocol, DDFQ was also applied to DL-tryptophan octyl ester (TOE) as a reference. The quenching of 2.5 μM TOE and 1.5 μM Mistic within a POPC bilayer containing 30% of one of the three brominated lipids used at an LPR of 400 is shown in Figures 5.18 A and 5.18 B, respectively. Whereas triplicate measurements for the entire set of brominated lipids procured comparable results for TOE, reproducibility was rather poor for quenching of Mistic fluorescence by 9-10BrPC (Fig. 5.18 B, yellow spectra). Therefore, the following analysis of DFQPs for Mistic was applied to the complete data as well as to a selective data set excluding from five spectra for 9-10BrPC the three spectra with the lowest apparent quenching efficiencies observed. All DFQPs were analyzed by distribution analysis (DA) as well as by two types of the parallax method (PM), PM-2 and PM-3.

The three approaches of data analysis yield comparable results for TOE quenching (Fig. 5.18 C and Tab. 5.3). The obtained values, in particular those for mean depth, h_m, and profile area, S, are well within the range of values reported by Ladokhin [138]. Only the widths of DFQPs, represented by either dispersion, σ, or radius of quenching, R_C, are significantly higher than the corresponding literature values, which can be attributed to the higher temperature in this study (25°C compared with 20°C in [138]), which is expected to result in higher thermal motion of the lipid acyl chains and, thus, in broader dispersion of the DFQP.

Distribution analysis of the DFQP for the complete data of Mistic DDFQ yields a rather broad distribution, although with limits that are within the dimensions of the bilayer and with a mean depth that is close to the center of the hydrophobic membrane core (Fig. 5.18 D).

PM-2 and PM-3 result in much narrower distributions with h_m = 7.9 Å and h_m = 6.9 Å, respectively, although DA and PM-3 have been shown to perform equally well in other cases [138]. Interestingly, very similar values are obtained irrespective of the mode of analysis for the selective data set (Fig. 5.18 E), with h_m = 7.8 Å in all cases. Eventually, the mean depth obtained for Mistic W13 lies well within the bounds of the hydrophobic membrane core of D_c = 13.6 Å, as defined on the basis of the location of the POPC carbonyl-glycerol component [23], independent of data set or mode of analysis applied.

The width of Mistic W13 distribution along the membrane depth coordinate was estimated on the basis of σ using Eq. 3.6 and assuming an underlying width of quencher (Q) distribution of $\sigma_Q^{hw} \approx 8$ Å [137]. On the one hand, on the basis of the complete data a distribution width for W13 of $\sigma_{trp}^{hw} = 31.8$ Å is obtained, which would suggest a distribution of W13 across the entire hydrophobic region of the membrane. On the other hand, considering the selective data results in a width of $\sigma_{trp}^{hw} = 7.5$ Å, implying a localization of W13 that is confined to one bilayer leaflet.

In addition to mean depth and distribution, the lipid exposure of W13 relative to TOE was inferred from the DFQPs. Normally, determination of the relative exposure, Ω, would require the quantum yields of probe and reference bound to lipid vesicles (Eq. 3.8), which, in turn, requires knowledge of the absorbances of both compounds at the excitation wavelength. Obtaining absorbances is feasible for membrane peptides such as the nonpolar peptide of cytochrome b_5 [138], which comprises three tryptophan residues and can be incorporated into a lipid bilayer at rather low LPRs. By contrast, the absorbance of reconstituted Mistic at 295 nm could not be determined because of substantial differential scattering at the high LPR required in conjunction with a low signal originating from Mistic's single tryptophan residue. Thus, the extinction coefficients at 295 nm, $\varepsilon_{295\,nm}$, of TOE and Mistic in 6 mM LDAO were determined and used instead of absorbances in the presence of vesicles for the calculation of quantum yields, assuming that the ratio of absorbances of TOE to Mistic in a bilayer environment is the same as in a micellar environment. The extinction coefficients for TOE and Mistic obtained are $\varepsilon_{295\,nm}^{TOE} = 3231$ M^{-1} cm^{-1} and $\varepsilon_{295\,nm}^{trp} = 3007$ M^{-1} cm^{-1}, respectively. With integrated and normalized fluorescence emission intensities of 284 μM^{-1} and 219 μM^{-1} for TOE and Mistic, respectively, the quantum yield of Mistic relative to TOE was calculated with Eq. 3.9 to $\Phi_{trp} = 0.83$. By inserting this value into Eq. 3.8 together with S = 19.2 for TOE and the DFQP area obtained on the basis of either the complete Mistic data set, S = 13.3, or of the selective data set, S = 8.2, relative exposures of $\Omega = 0.83$ or $\Omega = 0.51$, respectively, are obtained. Both values suggest substantial shielding of W13 as compared with TOE and the latter value even suggests lower exposure as compared with, for instance, W109 of the nonpolar peptide of cytochrome b_5 at 20°C with $\Omega = 0.69$ [138].

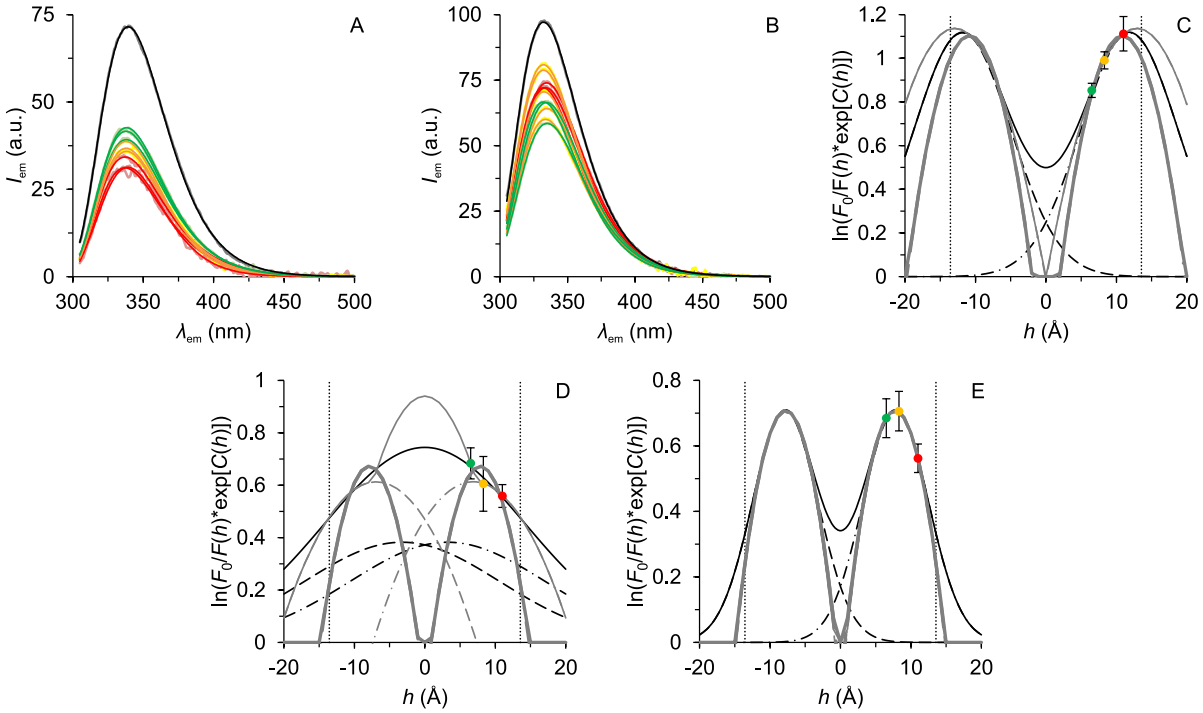

Figure 5.18: Translational orientation of Mistic within a POPC bilayer by DDFQ.
(A, B) Quenching of (A) TOE and (B) Mistic W13 fluorescence emission by brominated lipids (red) 6-7BrPC, (yellow) 9-10BrPC, (green) 11-12BrPC, and (black) emission spectrum in the absence of quencher. Emission intensity, I_{em}, is plotted versus emission wavelength, λ_{em} (λ_{ex} = 295 nm). Measured spectra in pale colors and log-normal fits in strong colors. (C–E) DDFQ for (C) TOE and (D, E) Mistic plotted as DFQP versus depth, h. A depth of h = 0 corresponds to the middle of the lipid bilayer. Fits were based on (black lines) DA, (thick gray lines) PM-2, and (thin gray lines) PM-3. Symmetrical components of fits corresponding to (solid lines) both leaflets, (dashed lines) inner leaflet, and (dash-dotted lines) outer leaflet are shown. DFQP data points corresponding to different brominated lipids are colored as in A and B. The width of the hydrocarbon region as determined in [23] is indicated by vertical lines. For reconstituted Mistic, fits were applied to averaged integrated intensities for (D) complete data (triplicates for 6-7BrPC and 11-12BrPC, quintuplicate for 9-10BrPC) and (E) selective data (only the two highest values considered for 9-10BrPC).

Table 5.3: Results of fits to DFQP for Mistic and TOE on the basis of DA and PM analysis

	DA			PM-2		PM-3		
data	h_m (Å)	σ (Å)	S	h_m (Å)	R_c (Å)	h_m (Å)	R_c (Å)	f
TOE [138]	11.3	5.5	18.9	10.3	5.8	11.4	8.9	0.38
TOE (this study)	11.9	6.9	19.2	10.9	8.9	12.9	12.8	0.5
Mistic (complete)	3.2	13.9	13.3	7.9	7.0	6.9	14.2	0.2
Mistic (selective)	7.8	4.6	8.2	7.8	7.1	7.8	7.0	1.0

Selective data comprised only the two highest DFQP values for 9-10BrPC. Analysis of TOE quenching corresponds to Figure 5.18 C. Analysis of complete and selective data for reconstituted Mistic correspond to Figures 5.18 D and 5.18 E, respectively.

5.5.4 Rotational Orientation by OCD

The alignment of Mistic within a macroscopically oriented POPC bilayer was investigated by oriented circular dichroism (OCD) spectroscopy (Section 3.3.3.2). This method has predominantly been used on α-helical peptides to distinguish between helix orientations perpendicular and parallel to the membrane surface.

OCD spectra were obtained for Mistic reconstituted at different conditions in a POPC bilayer (Fig 5.19). In addition to exploring different reconstitution conditions, other measures were taken to exclude adverse effects of experimental parameters on OCD measurements. Aggregational states after reconstitution were assessed by DLS and shown to be similar among different reconstitution conditions, some aggregates occurring only upon CyD-mediated reconstitution in the presence of Tris buffer at high residual LDAO concentrations (Fig. 5.19 A–C). Moreover, the absence of significant LD artifacts in OCD spectra was confirmed by a maximum LD ≤ 0.003 over the entire wavelength range, and the integrity of lipid films throughout the measurements was validated by photographs taken afterwards showing no signs of drifting (Fig. 5.19 D).

Although OCD spectroscopy, in principle, allows for an estimation of a helix tilt angle [177], for a helix-bundle MP like Mistic, an average angle would be obtained at best. Even more so, gaining quantitative information is commonly hindered by differential scattering and absorption flattening effects similar as in the case of conventional CD spectroscopy. Likewise, these effects became apparent for Mistic samples by the minute ellipticities at low wavelengths (Fig. 5.19 E, shaded region) as well as by the decreased ratio of ellipticities at 208 nm to 222 nm. Nevertheless, qualitative information on the orientation of Mistic could be deduced from the "fingerprint" band at around 208 nm in these spectra, which exhibited almost identical shapes after accounting for differences in absolute concentration by normalization to ellipticity at 222 nm (Fig. 5.19 F). A transmembrane (TM) orientation of an inserted α-helix (sometimes referred to as "I-state") is characterized by a strong decrease in ellipiticity at 208 nm giving rise to a positive signal at this characteristic wavelength, whereas a negative ellipticity at 208 nm corresponds to an alignment parallel to the membrane surface ("S-state") [126]. Most importantly, from the OCD spectra for reconstituted Mistic a TM orientation of the protein was ruled out because ellipticity was considerably negative in all of these, irrespective of reconstitution conditions.

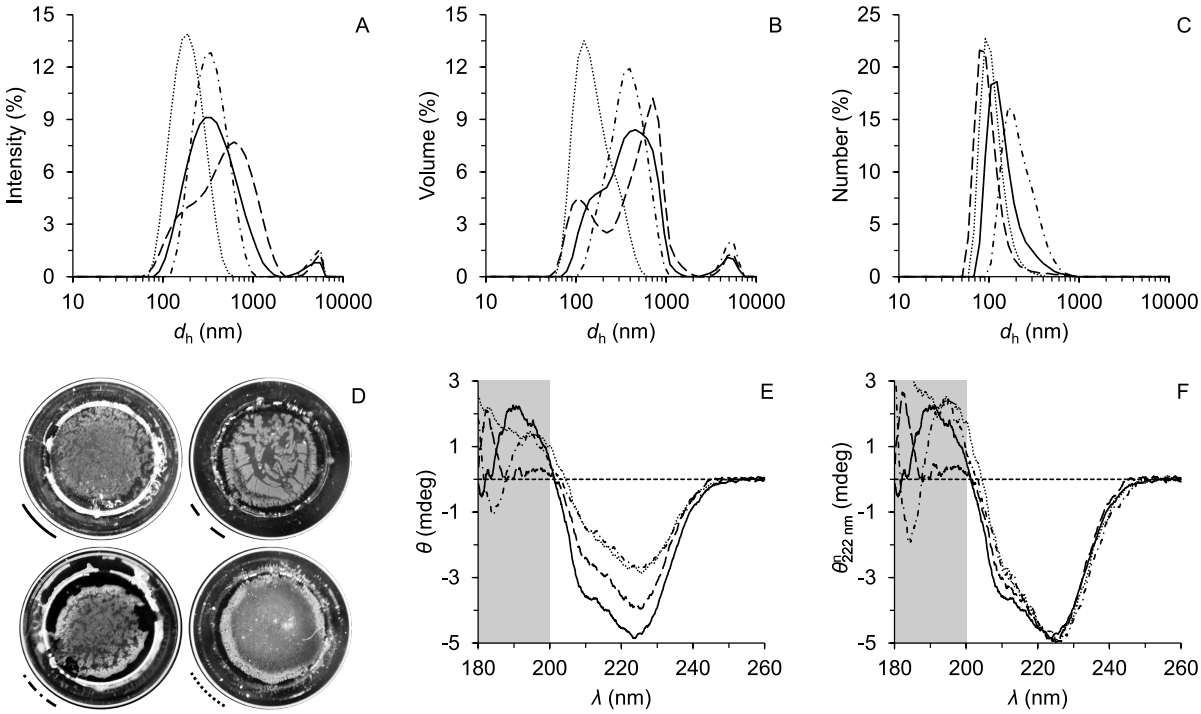

Figure 5.19: Rotational orientation of Mistic within a POPC bilayer by OCD.
(A–F) DLS and OCD measurements for Mistic in POPC bilayers at an LPR of 400 (solid lines) after CyD-mediated reconstitution in the presence of 50 mM Tris at pH 7.4 and 50 mM NaCl with $X_D^b = 0.04$, (dashed lines) after CyD-mediated reconstitution in the presence of 50 mM Tris at pH 7.4 and 50 mM NaCl with $X_D^b = 0.3$, (dash-dotted lines) after CyD-mediated reconstitution in the presence of 10 mM sodium phosphate buffer at pH 7.4 and 10 mM NaF with $X_D^b = 0.04$, and (dotted lines) after reconstitution by addition of vesicles in the presence of 10 mM sodium phosphate buffer at pH 7.4 and 10 mM NaF with $X_D^b = 0.04$. (A–C) DLS data obtained after reconstitutions and before OCD measurements showing light scattering weighted by (A) intensity, (B) volume, and (C) number versus hydrodynamic diameter, d_h. (D) Photographs of dried lipid films after OCD measurements. Reference to corresponding data in other panels is indicated by line segments. (E) OCD spectra with ellipticity, θ, versus wavelength, λ. (F) OCD spectra normalized to the same intensity at 222 nm to illustrate similar lineshapes.

6 Discussion

In this thesis, Mistic from *B. subtilis* was reconstituted into a POPC bilayer using a quantitative model for detergent removal by cyclodextrin (CyD), and, on basis of this approach, the topology of the bilayer-incorporated protein was investigated in terms of its rotational and translational orientation.

6.1 Cyclodextrin-Mediated Reconstitution

To fully exploit the advantages offered by CyD-mediated detergent removal and to apply this strategy to the reconstitution of Mistic, a quantitative model was furnished that describes the supramolecular state of a ternary CyD/lipid/detergent mixture (Section 4). The suitability of compounds chosen for Mistic reconstitution, that is, HPβCD, POPC, and LDAO, was verified by demonstrating fast interleaflet translocation of LDAO and the absence of substantial complexation of POPC by HPβCD (Section 5.1). Moreover, it was shown that LDAO removal by HPβCD is comparable to that by bio-beads and even fares better above millimolar concentrations.

Flip–Flop of LDAO Across the Lipid Bilayer As opposed to other detergents such as SDS, DDM, and $C_{12}E_8$ [178], fast translocation, or flip–flop, between the leaflets of a lipid bilayer has not been verified for LDAO by uptake and release experiments so far. Thus, as a prerequisite for reconstitution and solubilization experiments, fast kinetics of LDAO translocation across a POPC bilayer at 25°C was demonstrated herein. Although fast flip–flop of LDAO has already been construed from its fast solubilization kinetics [179] and its higher lipophilicity compared with ionic detergents, this result was not as obvious as one might assume.

On the one hand, flip–flop rates depend on the size and polarity of the detergent headgroup, both of which have an impact on the detergent's packing parameter [180]. In general, detergents with ionic or large polar headgroups are considered unlikely to rapidly traverse the hydrophobic bilayer core from one leaflet to the other, whereas nonionic detergents such as Triton X-100 [181] have been shown to exhibit fast flip–flop kinetics. For amphiphiles with headgroups of intermediate polarity such as zwitterionic detergents—including LDAO—assumptions on flip–flop kinetics cannot be made as readily. For instance, acyl carnitines, the zwitterionic headgroup of which contains a quaternary ammonium and a carboxyl moiety, cannot flip–flop across a

lipid bilayer comprising egg yolk phosphatidylcholine [182]. By contrast, palmitoyl carnitines exhibited measurable flip–flop rates for the translocation across erythrocyte membranes [183].

On the other hand, flip–flop rates are also sensitive to multiple experimental parameters, in particular to those directly pertaining to the lipid bilayer such as vesicle preparation procedure, lipid composition [184, 185], and intrinsic bilayer curvature [186, 187]. For instance, the localization of the sucrose monoester of myristic acid, which is a nonionic detergent, within the lipid bilayer depends on lipid headgroup characteristics and cholesterol content, which results in altered membrane insertion and, in turn, in different solubilization kinetics [185]. An effect of intrinsic bilayer curvature on flip–flop has been shown for bile salts [187]. Virtually no flip–flop was observed in SUVs [188], while transbilayer movement occurred in the hour time regime in LUVs composed of egg yolk phosphatidylcholine. Other parameters that may affect flip–flop rates are temperature and ionic strength, as in the case of the anionic detergent SDS [189]. Whilst transbilayer distribution is negligibly slow for SDS at 25°C, it occurs reasonably fast at elevated temperatures above 55°C [189].

Likewise, the capability of LDAO of flip–flopping between the two lipid bilayer leaflets is expected to depend on pH and ionic strength, as changes in headgroup moiety pK_a values and in shielding of the headgroup dipole affect its overall polarity, and on lipid composition. Therefore, it was important to confirm LDAO transbilayer equilibration under the same experimental conditions employed for subsequent solubilization and reconstitution experiments. In fact, the fast transbilayer movement observed for LDAO most likely is owed to the fact that its amine oxide headgroup is not a canonical zwitterion as, for instance, the phosphocholine moiety of the detergent *n*-dodecyl phosphocholine (DPC) or lipids such as POPC. Rather, amine oxides are characterized by a dipolar or dative bond, as the basic amine nitrogen donates two electrons to form the covalent bond with the oxygen atom. Furthermore, since the dipole moment of the amine oxide headgroup is oriented inversely with respect to that of the phosphocholine headgroup of POPC, and since it is known that lipid flip–flop can be induced by other amphiphiles [190], one might speculate that flip–flop of LDAO across the POPC bilayer is a cooperative process in that the opposing dipole moments of nearby detergent and lipid headgroups partially cancel each other out. Thus, the resulting reduction in headgroup polarity might result in concomitant flip–flop of LDAO and POPC from one leaflet to the other.

Application and Practical Aspects of Quantitative CyD-Mediated Reconstitution After validating the suitability of the constituents chosen for CyD-mediated reconstitution, values of all thermodynamic parameters required for application of the quantitative model were obtained for this set of compounds by means of multiple ITC experiments. These parameters included the critical micelle concentration (CMC) of LDAO, $R_D^{b,SAT}$ and $R_D^{b,SOL}$ from the

POPC/LDAO phase diagram, and $K_D^{i/aq}$ for the HPβCD/LDAO inclusion complex (Tab. 5.1). With the parameter values at hand, the quantitative model proved to be suitable to predict the cross points of reconstitution trajectories with the solubilization (SOL) and saturation (SAT) phase boundaries encountered upon CyD-mediated reconstitution both in the absence and presence of Mistic. An example of how the expected cross points of a reconstitution trajectory with the phase boundaries are calculated can be found in [81]. In conjunction with automated titrations, these predictions allowed for a correlation of distinct spectroscopic changes observed in real time by dynamic light scattering (DLS) and fluorescence spectroscopy with the phase boundaries (Section 5.3). Moreover, on the basis of the quantitative model, a systematic construction of reconstitution trajectories was possible that corresponded to different molar lipid/protein ratios (LPRs) but identical coverage of phase ranges, thus allowing for the direct comparison of resulting ITC isotherms (Section 5.4). These reconstitution experiments, together with results from DLS and circular dichroism (CD) spectroscopy, suggested that LPRs below 200 tend to promote protein-aggregate formation and, hence, should be avoided.

Implementation of Mistic reconstitution by CyD-mediated detergent extraction revealed some practical aspects that need to be considered to ensure the applicability of the approach in individual cases [81]. For example, besides the absence of undesirable lipid complexation, a suitable CyD derivative needs to be sufficiently soluble because CyD solubility imposes an upper bound on the titrant concentration for reconstitution, which, in turn, limits the amount of detergent that can be complexed. Thus, the phase diagram can be explored up to a certain lipid concentration only, so that poor CyD solubility ultimately constrains the accessible range of LPRs. A more intricate methodological issue is the physical removal of the CyD/detergent inclusion complex after reconstitution. Different approaches to separate inclusion complexes from proteoliposomes were investigated, all of which turned out to fail in the case of Mistic: (i) Size exclusion chromatography is suboptimal because of pronounced lipid retention on the column matrix [63]. Typically, losses of up to 40% of proteoliposomes were encountered with this method. (ii) Dialysis proved unsuccessful because the permeation behavior of dialysis membranes changes in the presence of CyD as observed earlier [71], resulting in the escape of protein through the dialysis membrane. (iii) High-speed centrifugation in a sucrose step gradient has been found to be most suitable for separating CyD/detergent inclusion complexes from proteoliposomes [71]. However, this approach did not succeed with Mistic as proteoliposomes remained in the top layer of the sucrose gradient, presumably because of Mistic's low molar mass.

Irrespective of how well a method performs in removing inclusion complexes after CyD-mediated reconstitution, validation of CyD-removal requires the quantitation of submillimolar residual concentrations, which poses another experimental challenge. Thin-layer chromatogra-

phy has a suboptimal detection limit for this purpose, and infrared spectroscopy was unable to yield reliable CyD concentrations as the corresponding bands overlapped substantially with the protein bands. This obstacle might be circumvented if the protein concentration is available from another method such as UV/Vis spectroscopy. The latter is, in turn, yet complicated by light scattering due to the proteoliposomes. Hence, more elaborate methods such as high-performance liquid chromatography or mass spectrometry are required to demonstrate complete removal of CyD and detergent. Nevertheless, as the vast majority of CyD derivatives are small, fairly inert, and do not absorb considerably in the UV/Vis range, downstream biophysical, or biochemical investigations involving spectroscopic methods such as CD spectroscopy or scattering techniques such as DLS are not impeded by the residual CyD/detergent complexes. This holds true for HPβCD, the removal of which was therefore refrained from after Mistic reconstitution.

Moreover, the quantitative model is limited in that it does not take into account (i) the possibility that a membrane protein (MP) might itself affect the lipid/detergent phase diagram, as is the case for KcsA [62], (ii) micellar sphere-to-rod transitions [152], (iii) non-ideal mixing of lipid and detergent, which has considerable impact at low lipid/detergent ratios, and (iv) partitioning of CyD into the micellar core that could add to and thus complicate the partition equilibria underlying the model [191]. In the case of POPC and LDAO, in particular, micellar sphere-to-rod transitions were reflected in reconstitution isotherms by additional, rather smooth transitions outside the coexistence range (Fig. 5.7), and preferential interactions between the dipolar headgroups of POPC and LDAO might contribute to non-ideal mixing. However, inclusion of such interactions into the model was of little relevance for Mistic reconstitution, as can be concluded from the close agreement of observed and predicted phase boundary cross points. In summary, as long as some practical requirements are followed, CyD-mediated extraction allows for tightly controlled MP reconstitution.

6.2 Membrane Topology of Mistic

The classical notion of canonical α-helical MPs having an ideal transmembrane (TM) orientation perpendicular to the membrane plane persists because deviations from this idealized scheme are normally limited to individual helices, and, up to now, an example of an α-helical MP with a topology substantially other than this has remained unknown. Strikingly, oriented circular dichroism (OCD) spectra of Mistic reconstituted in a POPC bilayer suggest the protein to be immersed in the lipid bilayer with a non-TM topology (Section 5.5.4). Although the results from OCD spectra only allow drawing conclusions on the average helix vector of the entire helix-bundle, the strongly negative band at 208 nm renders an in-plane topology likely.

The following sections will discuss how such a highly unconventional orientation conforms with what is known so far on Mistic's topology from experimental approaches as well as from MD simulations, and with speculations in the literature.

6.2.1 Membrane Association

The membrane association of Mistic, which has been shown before [82, 99, 102, 109], was reproduced by CyD-mediated reconstitution. Although Mistic lacks any known activity that may be exploited to directly demonstrate membrane association, the retained integrity of secondary structure and concurrent lack of protein aggregates in the presence of POPC vesicles left no doubt that Mistic associated with the lipid bilayer (Section 5.3). The proteoliposomes had a mean hydrodynamic diameter of 200–300 nm, which is relatively large and can be attributed to the slow rate of detergent removal and some residual LDAO [77, 192]. Assuming d_h = 250 nm on average, they contained ~1400 Mistic molecules at an LPR of 400, taking into account a headgroup area per POPC molecule of 0.68 nm^2 [23]. Membrane association was furthermore demonstrated by acrylamide fluorescence quenching measurements, which indicated substantially reduced accessibility of W13 to the water-soluble quencher for Mistic reconstituted in a POPC bilayer as compared with solubilized Mistic in micellar environments of various detergents except for DDM (Section 5.5.2). In addition, the relative exposure of W13 as inferred from DDFQ experiments indicated considerable lipid shielding.

Predictions based on hydropathy plots fail to recognize Mistic as an integral MP. Likewise, in the Orientations of Proteins in Membranes (OPM) database [193], Mistic is classified as a peripheral MP with an insertion depth of merely 2.6 ± 1.8 Å^2. However, this prediction is based on a continuum approach that minimizes the transfer free energy from the aqueous phase to the lipid bilayer by approximating the membrane hydrocarbon core as a planar slab. Therefore, mechanisms that affect topology such as membrane bending and specific lipid–protein interactions are ignored. There are multiple experimental clues suggesting that bilayer defects are, in fact, of utmost importance for membrane association of Mistic. First, an increase of d_h observed by DLS at proceeding detergent removal (Fig. 5.12 B) was attributed to fusion of proteoliposomes. Fusion may be caused by the presence of zwitterionic detergents with fusogenic activity such as CHAPS [194]. However, the absence of a similar observation in the absence of Mistic rather indicates the presence of protein-induced bilayer defects that promote vesicle fusion [195]. Second, acrylamide quenching experiments (Section 5.5.2) yielded a K_{SV} for reconstituted Mistic with a value between those for Mistic solubilized in DM and DDM

[2] Lomize A., Lomize M. & Pogozheva I., University of Michigan: Orientations of Proteins in Membranes (OPM) database, `http://opm.phar.umich.edu/protein.php?pdbid=1ygm` accessed Friday 19th February, 2016

micelles. Thus, the accessibility of W13 was low but still comparable to a micellar environment of large hydrophobic thickness. It cannot be excluded though that this residual accessibility arises merely from the intermediate hydrophobic thickness of the POPC bilayer rather than from water defects. The hydrophobic thickness of a pure POPC bilayer is 27.1 Å [23] and, thus, lies between the hydrophobic diameters of DM and DDM micelles of 26.2 and 31.8 Å, respectively, as determined by SAXS [196]. Likewise, the decrease of quenching efficiency observed for the series of maltoside detergents OM, DM, and DDM correlates well with increasing alkyl chain length, which is also known to linearly affect conformational stability of Mistic [73, 105]. Still, a comparison of bilayer hydrophobic thickness with micellar hydrophobic diameter is likely to be an oversimplification in that it omits the impact of different headgroups of lipid and detergent as well as of the rugged micelle-surface structure on the accessibility of the hydrocarbon core. Third, although unfolding experiments yielded only qualitative results (Section 5.5.1), the mere fact that Mistic proved to be amenable to urea-induced unfolding after reconstitution indicates a certain accessibility of the protein backbone to the denaturant despite the lipid bilayer environment. Although Mistic reconstitutions, in general, contained residual LDAO, it is unlikely that considerable bilayer perturbations resulted from the small amount of detergent remaining in the bilayer phase, X_D^b. For POPC, in particular, it has recently been shown by means of a swelling assay using stopped-flow light scattering that addition of up to 1 mM LDAO to 0.3 mM POPC LUVs (corresponding to $X_D^b = 0.27$) had virtually no impact on water permeability of the lipid bilayer [197]. In Mistic reconstitutions used for urea-mediated unfolding, the fraction of residual LDAO was merely $X_D^b = 0.05$. Thus, putative bilayer defects indeed appear to be induced by Mistic itself rather than by the detergent.

6.2.2 Orientation of Termini

Experimental data on the membrane topology of Mistic is fairly sparse. The principal work on Mistic by Roosild and coworkers [82] included a biotinylation assay on monocysteine variants to elucidate their topology in the inner membrane of *E. coli* in terms of the location of termini and loops with respect to periplasm and cytoplasm. Exposure to the periplasmic side was only found for residue 110 at the C-terminus, whereas residues located in the interhelical loops and the single natural cysteine at position 3 of the N-terminus were inaccessible to the membrane-impermeable thiol biotinylation reagent [82]. By contrast, Marino and coworkers [198] concluded a cytoplasmic localization of the C-terminus on the basis of a reporter fusion assay with alkaline phosphatase (PhoA) and green fluorescent protein (GFP). However, the enhanced expression of Mistic fusion constructs has been demonstrated for different target protein topologies including both intra- and extracytoplasmic orientations of the N-terminus

[84–98], and, likewise, the topology of C-terminal Mistic fusion constructs might possibly be affected by the GFP- or PhoA-tag itself. Frustration of a periplasmic localization of Mistic's C-terminus induced by these reporter fusion tags is even more conceivable considering the large sizes of both fusion tags relative to Mistic [199], with molecular weights of GFP and PhoA being about two and four times that of Mistic, respectively. In general, the PhoA/GFP reporter fusion assay is known to occasionally yield ambiguous results. For instance, in a comprehensive topology study the assay was not applicable to three out of 34 integral MPs from *E. coli* [200], and the orientation of dual-topology MPs as determined by the assay has been shown to be sensitive to single charge mutations [45]. Moreover, the reporter fusion assay only focused on the position of the C-terminus. It has been shown that both the N- and C-terminus of most α-helical MPs are located in the cytoplasm [201, 202], but a co-localization of both termini outside the membrane would imply a TM orientation of Mistic, which is not supported by the results of OCD measurements. Unfortunately, other approaches to a topological mapping of α-helical MPs, such as deuterium exchange mass spectrometry [203], are putatively not applicable to or at least substantially complicated for Mistic as the accessible portion of the membrane-immersed polypeptide is limited to a few amino acid residues because of the lack of an extramembranous domain.

Similar to dual-topology MPs, the distribution of basic residues in Mistic lacks a substantial bias towards one side of the protein and thus does not seem to support a preferential orientation on basis of the positive-inside rule. Most MPs obey this rule by containing more positive charged residues on the cytoplasmic side of the membrane [51, 204]. Whilst the distribution of charged residues in Mistic though lacks an evident asymmetry (Fig. 2.3), its overall dipole moment as calculated with the Protein Dipole Moments Server [205] is oriented with its positive end towards the N-terminus and helices H1 and H2, whereas the negative end is oriented towards the C-terminus and helices H3 and H4 (Fig. 6.1). Assuming that the positive-inside rule is not strictly coupled to translocon-mediated membrane insertion and the requirement of a positive N-terminal signal sequence, this orientation of Mistic's dipole moment supports an extracytoplasmatic location of the C-terminus.

6.2.3 Rotational Orientation and Immersion Depth

Nevertheless, an unappreciated but interesting result from the biotinylation assay of Roosild and coworkers [82] is the fact that the N-terminal cysteine appeared to be inaccessible, in contrast with the C-terminus. Assuming a TM orientation of Mistic, albeit with a pronounced negative hydrophobic mismatch, both termini would be expected to co-localize at the same side of the membrane, regardless of whether this is the cytoplasmic or the periplasmic side of

the host inner membrane. Moreover, on the basis of the available three-dimensional structure determined by solution nuclear magnetic resonance (NMR) spectroscopy [82], the distances of both termini to the center of the helical bundle are similar (Fig. 2.4 A), which would suggest a comparable accessibility. Therefore, an explanation for the disparate accessibilities observed for the termini would require either a peripheral or extramembranous localization of helix H1 or H4 or a considerable tilt of the entire helix bundle relative to the membrane normal. Depending on its degree, such a tilt would enable membrane burial of the N-terminus or the transfer of one of the two termini to the opposite side of the lipid bilayer and, hence, an in-plane orientation of Mistic.

A membrane-embedded N-terminus would be energetically highly unfavorable and, thus, is unlikely. A peripheral localization of helix H1 can also be excluded on the basis of acrylamide quenching and DDFQ experiments as these revealed a position of W13 within the hydrophobic core of the membrane. By contrast, a conformational change upon membrane association involving a displacement of helix H4 has been suggested by the Sansom group [100] on the basis of 30-ns MD simulations on Mistic in LDAO micelles. A structural reorganization as such would pertain to the tertiary structure and, thus, would not necessarily result in a change of the CD spectrum upon reconstitution. Indeed, leaving aside differential scattering and absorption flattening effects at low LPRs, no substantial changes in secondary structure were observed upon reconstitution of Mistic as assessed by CD spectroscopy (Fig. 5.10 C). Also, rearrangement of a single helix cannot be excluded by the OCD measurements conducted, as these do not allow for an evaluation of individual contributions by one ore several helices to the overall polypeptide orientation.

This said, it is noteworthy that these MD simulations suggested Mistic to be stable in water but to partially unfold in detergent micelles, which is diametrically opposed to what is observed *in vitro* [73, 82]. Moreover, although micellar environments have helped to elucidate the thermodynamic stability of Mistic in great detail [73, 108], their capability of mimicking the native hydrophobic environment of Mistic must be considered inferior to lipid bilayer systems as they are unable to reproduce bilayer-specific properties such as a lateral pressure profile, the membrane dipole potential, or bilayer deformability. Fortunately, the Sansom group has also performed high-throughput coarse-grained MD simulations on a plethora of MPs in self-assembled 1,2-dipalmitoyl-*sn*-glycero-3-phosphocholine (DPPC) bilayers that account for aspects as these, covered an extended duration of 200 ns, and—most importantly—also included Mistic [104]. In fact, while these simulations suggested TM topologies for all other MPs investigated, solely Mistic appeared to have an in-plane topology in the final snapshot with two pairs of helices confined to either of the two bilayer leaflets and oriented perpendicular to the membrane normal. This *in silico* topology goes well in line with both the OCD data and

DDFQ experiments in this work. In fact, the distance of W13 to the center of the hydrophobic membrane, according to the coarse-grained MD simulation (Fig. 6.1), is ∼8 Å and thus in line with the results obtained with fluorescence quenching by brominated lipids. Moreover, revisiting the results of the biotinylation assay of Roosild and coworkers [82] in light of the coarse-grained MD simulation shows that both are indeed compatible with each other. As demonstrated in Figure 6.1, the MD simulation fully supports the experimental results on side chain accessibility, as E110 sticks out of the bilayer headgroup region, whereas the remaining four residues tested do not reach beyond the headgroup regions.

6.2.4 In-Plane Topology Model

The peculiar result of the coarse-grained MD simulation on Mistic has not been explicitly addressed in the literature so far. To investigate more closely the means by which an in-plane topology of Mistic might be governed, the coarse-grained snapshot of Mistic in a DPPC-bilayer that is available online[3] was back-mapped to an atomistic model as detailed in [206] (with kind help by Kristyna Pluhackova, Computational Biology, University of Erlangen-Nuremberg, Germany) and, after addition of solvent and counter ions, subjected to a short 1-ns equilibration with GROMACS [207] to allow for rotameric optimization of sidechains. This short simulation consisted of a steepest-descent energy minimization in vacuum at periodic boundary conditions and 310 K using the CHARMM forcefield. The resulting atomistic model is shown in Figure 6.1.

Membrane Distortion First, the summarized online report provided with the coarse-grained MD simulation snapshot includes projection maps depicting bilayer distortion[3]. From these, bilayer thinning in the annular lipid region around Mistic by up to 13 Å along the bilayer normal and extending to ∼10 Å from the protein surface becomes fairly obvious. Taking a closer look, deep penetration of DPPC headgroup moieties into the bilayer center and conformational flexibility of lipid alkyl chains are accompanied by close approximation of solvent molecules to the protein. In fact, 35 water molecules are both within 5 Å of the protein surface and, at the same time, within 5 Å of the bilayer plane centered at the protein. Thus, Mistic appears to induce a considerable water defect that allows for the hydration of some polar sidechains within the membrane and, hence, reduces the overall loss of solvation energy [208]. Thus, the MD simulation results strengthen the experimental indications for membrane perturbation. With particular regard to the high number of acidic and basic residues in Mistic, it is important to note that membrane defects are known to result in non-additive partitioning of charged residues, as the cost to embed the first charged amino acid by formation of a water defect is substantially

[3] Bond P. J., Chetwynd A. P., Scott K. A. & Sansom M. S.P.: Coarse-grained database (CGDB), University of Oxford, `http://sbcb.bioch.ox.ac.uk/cgdb/simtable.php?pdb=1ygm` accessed Friday 19th February, 2016

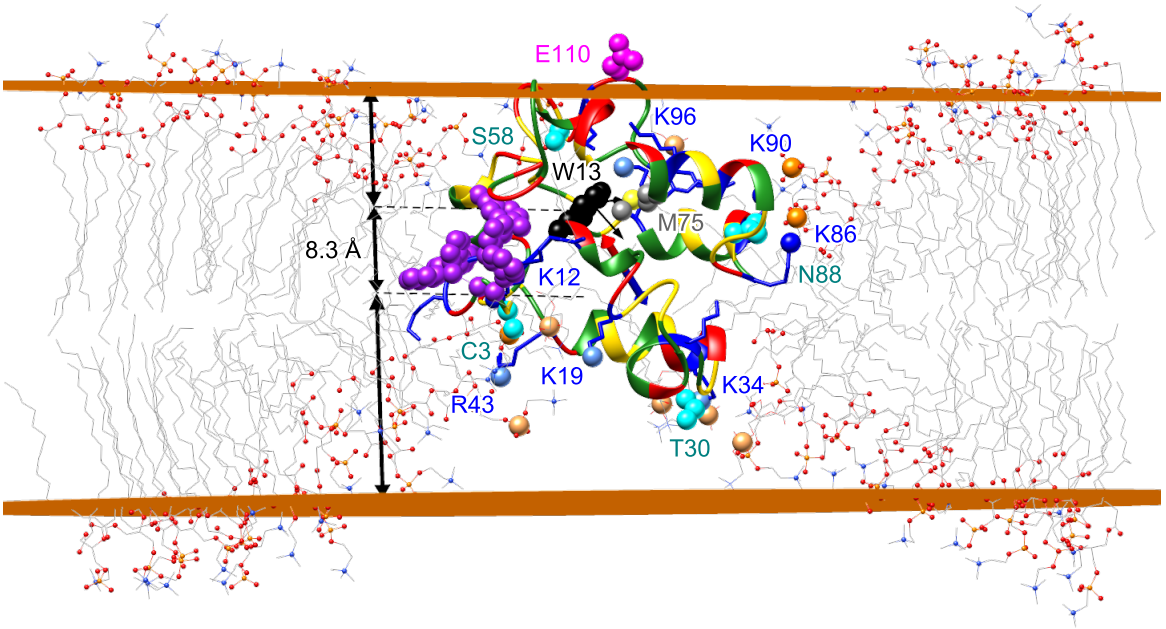

Figure 6.1: In-plane topology of Mistic based on coarse-grained MD simulation.
The atomistic model of Mistic in a DPPC bilayer was devised by back-mapping from the final snapshot of a 200-ns coarse-grained MD simulation of [104]. Only a slab of the lipid bilayer is shown and water molecules have been omitted for clarity. Lipid tails are depicted in wire representation, heteroatoms as small spheres. Color code of DPPC molecules depicts (gray) carbon, (red) oxygen, (blue) nitrogen, and (orange) phosphorus atoms. The protein is depicted in ribbon representation with residue segments colored according to hydropathy: (Red) Acidic, (blue) basic, (yellow) polar uncharged, (green) hydrophobic nonpolar. The dipole moment of Mistic as calculated with the Protein Dipole Moments Server [205] is depicted as a blue/red double arrow at the protein center. Snorkeling is illustrated by sphere representation for pairs of (blue) ε- or η-nitrogens of lysines and arginines, respectively, and (orange) phosphorus atoms of lipid headgroups that are less than (dark colors) 4 Å and (light colors) 6 Å away from the former. Additional specific features are also depicted in sphere representation: Residues that had been found [82] to be (cyan) inaccessible or (pink) accessible to a membrane-impermeable thiol biotinylation reagent. (Black) The single tryptophan residue, W13, the emission of which was monitored in fluorescence experiments, together with its distance from the bilayer center. The latter was determined in reference to (orange) two planes corresponding to the leaflet headgroup regions as deduced from the non-mass-weighted centroids of lipid headgroup phosphorus atoms. (Gray) M75 is within reach for a sulfur-aromatic interaction with W13. The sulfur atom is depicted in yellow, and vectors for the normal of the aromatic ring and its distance to the M75 sulfur atom are shown as black arrows. (Purple) The cluster of aromatic residues at the N-terminal side.

larger than for subsequently introduced charged side chains, which merely require an increase in size of the water defect [209–211]. Interestingly, as the location of W13 is central relative to the protein core, its distance of 8.3 Å to the hydrocarbon core of the membrane implies that the position of Mistic is actually shifted towards one bilayer leaflet. Accordingly, the MD simulation snapshot exhibits asymmetric membrane thinning with a water defect that is less pronounced on the C-terminal side.

Salt Bridges Besides hydration by penetrating water molecules, it has already been speculated that ionizable side chains of Mistic might be stabilized to some extent by formation of salt bridges [105]. Charges residing within the low dielectric medium of a membrane are energetically highly unfavorable and, hence, generally considered unlikely. Therefore, titratable side chains of bilayer-inserted MPs are usually expected to have a neutral protonation state. Nevertheless, ion-pairs preformed upon folding may well insert into the hydrocarbon core [212], and even more so if ancillary hydrogen bonds are possible. In fact, the MD simulation suggests that quite many salt bridges might be formed (Fig. 6.2), most of which would remain in vicinity to the headgroup regions. Only putative salt bridges in loops 1 and 3 are centered in the hydrophobic core of the lipid bilayer. Moreover, salt bridges between neighboring residues (that is, residues i and $i + 4$) of opposite charge, as in the case of K76 and D80, might contribute to helical stability [213].

Snorkeling In addition to intra-molecular interactions, protein–lipid interactions may further reduce the energetic costs that accompany the insertion of polar residues into the lipid bilayer. Notably, snorkeling of basic side chains towards the headgroup regions is well known for anchoring membrane peptides and proteins in the lipid bilayer [52, 54]. Indeed, the MD simulation suggests close contacts of at least half of the lysine side chains with DPPC phosphate moieties (Fig. 6.1). Actually, the distribution of lysine residues in the primary structure of Mistic appears to favor an in-plane topology, as it is characterized by a long central span comprising residues 35–75, which lacks any lysines (Fig. 2.3). As a result, the distribution of basic residues is roughly split into two clusters that are well accommodated by facing the opposing headgroup regions of the lipid bilayer. The basic side chains on either side of the bilayer further promote membrane thinning by pulling water and lipid headgroups [209, 215, 216].

Membrane dipole potential Mistic contains considerably more acidic residues than basic residues. Again, acidic side chains are generally expected to be protonated when burried in the membrane interior, as a lack in favorable charge–charge interactions or hydrogen bond acceptors leads to a substantial increase in pK_a. As argued above, the local microenvironment of titratable side chains may counteract these pK_a shifts by formation of salt bridges [217, 218]. However, with regard to acidic side chains in particular, Broecker and coworkers already speculated [73] that membrane association of Mistic might rely on the positive membrane dipole potential, Ψ_d [219–222]. The membrane dipole potential entails an internal positive charge of the membrane that drops off towards the headgroup regions. It arises from the alignment of lipid carbonyl groups, dipolar moieties of lipid headgroups, and water molecules of the hydration layer at the interface between lipid bilayer and aqueous bulk [221, 223] and is responsible for the higher permeability of membranes to anions relative to that for cations. Estimated values of

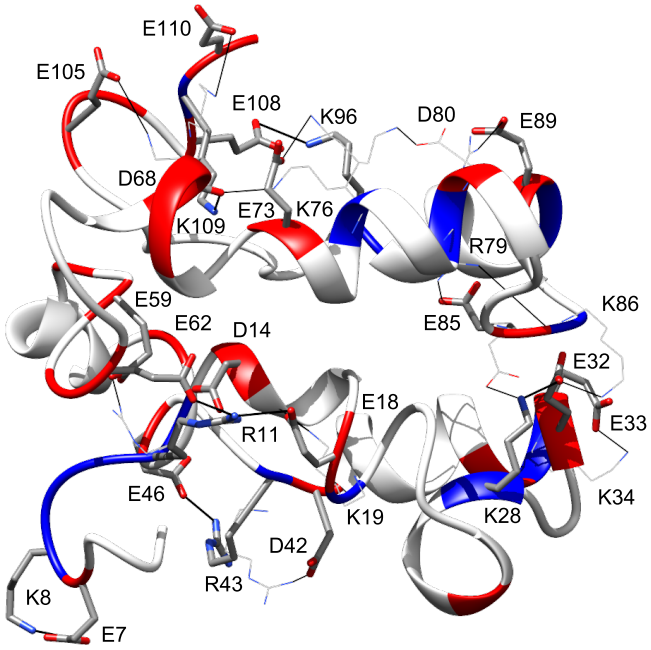

Figure 6.2: Potential salt bridges stabilizing charged residues in Mistic.
Atomistic model is based on the final coarse-grained MD snapshot for Mistic in a self-assembled DPPC bilayer [104]. (White) The protein is depicted in ribbon representation with ribbon segments colored corresponding to (blue) positively and (red) negatively charged residues, and oriented with the line of sight roughly parallel to the bilayer plane, with helices H1 and H2 at the bottom, and helices H3 and H4 at the top. (Black lines) Potential salt bridges between side chains of (K, R) positively and (D, E) negatively charged amino acid residues that might stabilize Mistic. Residues that might participate in salt bridges at a distance <4 Å between donor nitrogen and acceptor oxygen are depicted in stick representation. Additionally, side chain rotamers that might approach salt bridge partners in contrast to rotamers of the MD snapshot are depicted in line representation. Rotamers were taken from the Dunbrack backbone-dependent rotamer library as described in [214]. Note that some low-probability rotamers are included just to illustrate that more salt bridge partners might be in reach of certain residues. Color code depicts (gray) carbon, (red) oxygen, (blue) nitrogen atoms. Solvent and bilayer, interactions involving histidine residues, as well as charged side chains that are not in reach of a salt bridge partner have been omitted for clarity.

Ψ_{d} are rather large, lying in the range of several hundred millivolts [215, 221, 223]. Thus, an interplay between deprotonated aspartate and glutamate side chains of Mistic with the positive membrane dipole potential may well have a part in Mistic's membrane association. In fact, despite the rather homogeneous distribution of acidic side chains across Mistic's primary structure, the subdivided distribution of basic residues indirectly results in an accumulation of net negative charge in the central region of the protein. Moreover, considering that the membrane dipole moment hinders the insertion of positive charges as compared with negative charges, the orientation of Mistic's dipole moment (Fig. 6.1) suggests that the N-terminus is not transferred across the membrane and thus adopts a cytoplasmic localization.

6.2.5 Implications of an In-Plane Topology for Biological Function

Molecular Scale Although nothing is known yet about the biological function of Mistic on a molecular scale, one can almost certainly expect it to be directly related to Mistic's remarkable topology. A preliminary hypothesis raised so far suggests that Mistic might operate as a sensor of membrane thickness (Fig. 6.3). This concept mainly arises from the fact that Mistic's conformational stability substantially depends on hydrophobic thickness as assessed with micelles comprising maltoside surfactants of different alkyl chain lengths [73, 105]. The molecular response to a change in membrane thickness is envisaged to involve a change in distance between the two helix pairs that reside in the leaflets of the lipid bilayer. In this scenario, loop 2 would act as a flexible linker, whereas the helix pairs H1/H2 and H3/H4 would remain more or less fixed in close vicinity to the headgroup regions. The kink in helix H2 could contribute to flexibility like a hinge. In fact, in the back-mapped atomistic model after equilibration, the end of helix H2 following its kink appears to be more unraveled than in the original final snapshot of the coarse-grained MD simulation. Experimental indications for the hypothesis come from the Schlierf group that has applied single-molecule Förster resonance energy transfer spectroscopy to Mistic to elucidate unfolding kinetics [224]. Current continuation of these experiments using dual-labeled Mistic variants indicate both decreased and more dynamic packing of the protein core with longer alkyl chain length of solubilizing maltoside detergents, hence supporting the presumption that the distance between the helix pairs is sensitive to changes in hydrophobic thickness (Georg Krainer, B Cube, Center for Biological Engineering, University of Dresden, personal communication).

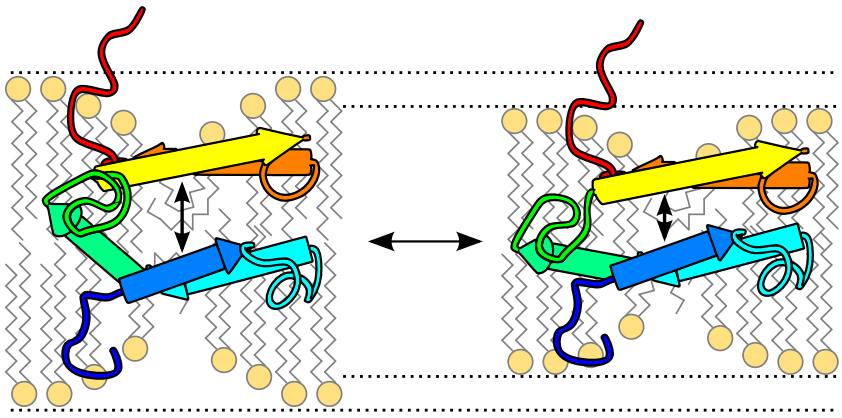

Figure 6.3: Hypothesis of Mistic acting as a sensor for hydrophobic thickness.
Mistic might be imagined to respond with a conformational rearrangement of its helix-bundle to changes in hydrophobic thickness. In this scenario, smaller hydrophobic thickness results in a decreased distance between helix pairs H1/H2 (blue to green) and H3/H4 (yellow to red).

In view of this hypothesis, the interplay between residues forming the protein core needs to be revisited, as functionally imposed dynamics of helix pair distance would require a finely tuned balance between stability and adaptability. In a structural disruption study, Roosild and coworkers identified M75 as a core residue essential for Mistic's integrity [82]. Moreover, a mutation of W13, which is part of a striking aromatic cluster containing H9, H10, F51, and Y55 (and also F5 and F6 in the coarse-grained MD simulation snapshot shown in Figure 6.1), reduced yield of a fusion construct with a potassium ion channel to less than 50% as compared with wild-type expression. In the NMR structure of Mistic, the center of the benzene ring of the W13 indole is 8.6 Å away from the M75 sulfur atom, with an angle between the sulfur-aromatic vector and the normal vector of the six-membered aromatic ring of 27°. Nevertheless, in the atomistic model based on the final coarse-grained MD simulation snapshot of the Sansom group, this distance approaches 5.8 Å with an angle of 55°. This suggests that W13 and M75 may well come within reach for a sulfur-aromatic interaction upon membrane insertion. These kinds of interactions are known to occur over longer distances of up to 6 Å as compared with hydrogen bonds or salt bridges [225–227]. Therefore, an interaction between W13 and M75 may be conceived to assist in the required flexibility between the two helix pairs without putting interhelical contact at risk. Similarly, auxiliary hydrogen bonds involving the M75 sulfur atom and backbone hydrogens that are longer than canonical hydrogen bonds [228, 229] as well as van der Waals interactions to proximate hydrophobic side chains (e.g. to residues 15–17) can contribute to protein core stability. Not least, the relatively large widths of DFQPs observed for W13 might reflect a less restrictive localization due to these dynamics along the membrane normal.

Cellular Scale The hypothesis outlined above includes speculations that raise more questions, such as how Mistic should be able to sense hydrophobic thickness whilst perturbing local bilayer order by introducing water defects. Furthermore, the question remains how information on hydrophobic thickness might be integrated and passed to the potassium ion channel YugO, which is presumably regulated by Mistic in the course of biofilm formation (Section 2.2), or to other putative interaction partners. Moreover, Mistic's alleged sensor function cannot be pinned down to hydrophobic thickness as the latter interdigitates with several related physicochemical membrane properties. In fact, pursuing the putative importance of Ψ_d for membrane insertion of Mistic suggests that hydrophobic thickness might rather be a secondary effector. Although still insufficiently understood, connections of the membrane dipole potential to both membrane hydration and hydrophobic thickness have been established. At low membrane hydration, Ψ_d shows a reversal in sign resulting in a negative membrane interior [230], and the spread of Ψ_d appears to depend on the hydrophobic thickness [215]. Moreover, the magnitude of Ψ_d

depends on lipid chain packing [231]. Although most of these findings are rooted in MD simulations and lack experimental evidence, they emphasize that a whole set of candidates of bilayer properties that might be sensed by Mistic must be considered. Taking this perspective, it appears tempting to build a bridge from membrane thickness and hydration to a cellular level involving salt concentration, in particular potassium ion concentration, and osmotic stress. Moreover, supposing that Mistic's function depends on the membrane dipole potential, one might speculate that Mistic might be sensitive, in addition, to the TM potential and the surface potential, as the total electrostatic potential profile of a membrane is a combination of all of these. As the dipole moment of Mistic adopts an angle of $\sim 45^{\circ}$ to the membrane normal (Fig. 6.1), dipole reorientation as described in [232] might occur in response to a change in the TM potential.

Reaching beyond the context of the membrane, the relevance of specific physicochemical membrane properties as well as of YugO and Mistic to biofilm formation or related processes remains unclear. This is in part due to the broad spectrum of pathways encountered in biofilm formation and affected by potassium ion concentration in particular. As outlined in Section 2.2, both Mistic and YugO play essential roles in the autoregulatory loop that promotes biofilm assembly in *B. subtilis* and involves potassium ion efflux. Many more cellular processes in *B. subtilis* though are known to be potassium ion-dependent, such as respiration [233], sporulation [234], response to osmotic stress [235], motility [236] and colony spreading [237]. Accordingly, there are more players that modulate potassium ion efflux, not all of which have yet been characterized. For instance, the *yhaSTU* operon has been identified, which includes a protein with sequence similarity to the monovalent cation/proton antiporter-2 (CPA2) family, referred to as YhaU, and two associated regulatory proteins, YhaS and YhaT [238]. YjaU and YhaS show interesting parallels to YugO and Mistic in that YhaU shows potassium ion efflux activity that is modulated by YhaS, and YhaS is predicted to have a peripheral membrane topology, lacks any reported homolog, and has a size of 112 amino acids. However, Mistic and YhaS do not share any similarities in terms of sequence or hydropathic profile. YhaS is mainly hydrophilic, too, but contains a hydrophobic N-terminal domain that is predicted to serve as a membrane-anchor.

6.3 Outlook

The in-plane topology of Mistic is the most striking finding of this work and raises a plethora of new questions. For the time being, corroborating the results from OCD measurements by other methods is of major importance. Complementary experiments by linear dichroism (LD) spectroscopy conducted in the course of this project proved unsuccessful because of technical

difficulties, as application of this method to MPs is still in its infancy. An ongoing collaboration between the group of Prof. Sandro Keller and Applied Photophysics (Leatherhead, UK) might advance the technical improvements required to resolve these issues. On the basis of the results in this work, efforts have though been initiated to scrutinize the topology of Mistic by other methods, above all by solid-state NMR spectroscopy [239]. To this end, Markus Fleisch now continues his work started in the Keller group with Prof. Bernd Reif (University of Munich) by producing isotopically labeled Mistic, which will need to be reconstituted before being subjected to solid-state NMR measurements. Sample preparation for these will be challenging, as they require very low LPRs and low ionic strength and, thus, might require switching to alternative systems for reconstitution such as bicelles or nanodiscs [203, 240]. Still, solid-state NMR is the most promising strategy to shed more light on Mistic's topology, as it does not suffer from the drawbacks of other methods, such as the introduction of membrane-perturbing labels or reporter molecules, or the requirement of substantially sized extramembranous loops or domains [241, 242]. Solution NMR experiments involving dissolved oxygen to enhance paramagnetic relaxation rates might add to the intended solid-state NMR experiments [243, 244].

Medium-term investigations should dissect the influence of different physicochemical bilayer properties on Misitc's topology. To this end, different probes with specific reporter capabilities or modulating activity should be employed. For example, the membrane dipole potential can be increased or reduced with 6-ketocholestanol and phloretin, respectively, and measured using hydrophobic ions [221]. The TM potential, on the other hand, can be assessed by potentiometric fluorescent dyes such as Thioflavin T [112] or di-8-ANEPPS. As LDAO tends to form worm-like micelles [95, 168], maybe even the micellar dipole potential can be made use of in future experiments as in [245]. Fluorescent probes may also allow following differential changes relating to membrane hydration [246]. Moreover, an assay providing information on changes in the flip–flop rate of NBD-labeled phospholipids [247] could elucidate the relevance of bilayer perturbations for Mistic reconstitution. For the same purpose, a vesicle swelling assay using stopped-flow light scattering as established in [197] will be used. Preliminary atomistic MD simulations in cooperation with Dr. Jochen Hub (University of Göttingen) support a higher bilayer permeability in the presence of Mistic as compared with pure POPC vesicles (personal communication).

In the long term, focus needs to be shifted more towards *in vivo* studies to gain more insight about Mistic's function. Certainly, a POPC bilayer as used for reconstitution herein is a simplification of the native membrane environment. The plasma membrane of *B. subtilis* is known to contain mainly polar lipids, 70% of which is phosphatidylglycerol, which bears a negatively charged headgroup, whereas 12% of polar lipids is phosphatidylethanolamine [248]. Specific lipid compositions can induce topology rearrangements [39], which has been shown

for phospholipids with polar headgroups in particular. For example, the lactose permease from *E. coli* undergoes topology flipping in the presence of phosphatidylethanolamine [48], and phosphatidylglycerol has been shown to affect the topology of leader peptidase [46] and of the TM segment derived from phospholamban [47]. Moreover, lipid composition has been shown to affect *in vitro* production of Mistic [102] and membrane interactions of single Mistic helices [109]. In conclusion, investigating more complex and native-like lipid compositions will be important for future functional studies. Moreover, emphasis on functional aspects will require production of YugO for interaction studies and include collaborations with groups from bacterial physiology and electrophysiology. Throughout all stages of upcoming research on Mistic's topology and function, MD simulations are expected to complement experimental results.

7 Conclusions

The α-helical membrane protein Mistic from *B. subtilis* was successfully reconstituted into a POPC bilayer and subjected to topology studies. The following major conclusions can be drawn on the basis of this work.

The advantages offered by cyclodextrin-mediated detergent extraction for membrane-protein reconstitution can be exploited by a new quantitative model. The model based on linked equilibria describes the supramolecular state of a ternary cyclodextrin/lipid/detergent mixture.

- All parameters required to apply the model to a given set of cyclodextrin, lipid, and detergent can conveniently be determined with a combination of microcalorimetric assays. The thermodynamic parameters are derived from a set of tried-and-tested isothermal titration calorimetry protocols and include the critical micelle concentration of the detergent, the phase boundary slopes $R_{\mathrm{D}}^{\mathrm{b,SAT}}$ and $R_{\mathrm{D}}^{\mathrm{b,SOL}}$ of the lipid/detergent phase diagram, and the dissociation constant $K_{\mathrm{D}}^{\mathrm{i/aq}}$ of the cyclodextrin/detergent inclusion complex.

- The model can be adapted to other cyclodextrin/lipid/detergent combinations provided that the detergent translocates quickly between bilayer leaflets and that unspecific lipid complexation by the cyclodextrin is negligible.

- The approach allows for highly reproducible and low-volume membrane-protein reconstitution, which enables the systematic optimization of key parameters such as the lipid/protein ratio and, hence, obviates cumbersome trial-and-error approaches.

- Most cyclodextrin derivatives are fairly inert and do not absorb considerably in the UV/Vis range. Therefore, by making use of automated titrations, spectroscopic monitoring of reconstitutions in real time is possible in addition to calorimetric monitoring. Moreover, downstream biophysical or biochemical investigations involving spectroscopic methods or scattering techniques are not impeded by the residual inclusion complexes.

- The model allows for predicting reconstitution trajectories and their cross points with phase boundaries. The possibility of tailoring reconstitution trajectories in a quantitative manner and, if necessary, adjusting the rate of detergent extraction is expected to provide better control over membrane-protein reconstitution in terms of the final concentrations of

all species involved. Improved control over the size and homogeneity of proteoliposomes and the orientation of membrane-embedded proteins can also be envisioned because these properties depend on the rate of detergent extraction.

Mistic proves to be an exception to canonical α-helical membrane proteins not only in terms of its uncommonly hydrophilic surface but also an in-plane topology *in vitro*.

- Oriented circular dichroism results suggest that the helix-bundle of Mistic is oriented parallel to the membrane plane. This result goes in line with a recent coarse-grained MD simulation of Mistic in a self-assembled lipid bilayer.

- Fluorescence quenching experiments suggest residual accessibility of Mistic's single tryptophan to a water-soluble quencher and that this residue is located about 8 Å from the hydrophobic core of the lipid bilayer. This suggests a position of the protein that is shifted towards one bilayer leaflet.

- Several experimental results suggest that perturbation of the lipid bilayer in the form of water defects accompanies Mistic reconstitution. These might be key to the unusual membrane association of Mistic.

References

[1] Singer, S. J. and Nicolson, G. L. (**1972**). "The fluid mosaic model of the structure of cell membranes." *Science*, *175*, 720–731.

[2] Guidotti, G. (**1972**). "Membrane proteins." *Annual Review of Biochemistry*, *41*, 731–752.

[3] Rees, D., DeAntonio, L., and Eisenberg, D. (**1989**). "Hydrophobic organization of membrane proteins." *Science*, *245*, 510–513.

[4] Delcour, A. H. (**2002**). "Structure and function of pore-forming beta-barrels from bacteria." *Journal of Molecular Microbiology and Biotechnology*, *4*, 1–10.

[5] Wallin, E. and von Heijne, G. (**2008**). "Genome-wide analysis of integral membrane proteins from eubacterial, archaean, and eukaryotic organisms." *Protein Science*, *7*, 1029–1038.

[6] Overington, J. P., Al-Lazikani, B., and Hopkins, A. L. (**2006**). "How many drug targets are there?" *Nature Reviews Drug Discovery*, *5*, 993–996.

[7] White, S. and von Heijne, G. (**2005**). "Transmembrane helices before, during, and after insertion." *Current Opinion in Structural Biology*, *15*, 378–386.

[8] Laage, R. and Langosch, D. (**2001**). "Strategies for prokaryotic expression of eukaryotic membrane proteins." *Traffic*, *2*, 99–104.

[9] Rudolph, R. and Lilie, H. (**1996**). "In vitro folding of inclusion body proteins." *The FASEB Journal*, *10*, 49–56.

[10] Bernaudat, F., Frelet-Barrand, A., Pochon, N., Dementin, S., Hivin, P., Boutigny, S., Rioux, J. B., Salvi, D., Seigneurin-Berny, D., Richaud, P., Joyard, J., Pignol, D., Sabaty, M., Desnos, T., Pebay-Peyroula, E., Darrouzet, E., Vernet, T., and Rolland, N. (**2011**). "Heterologous expression of membrane proteins: Choosing the appropriate host." *PLoS One*, *6*.

[11] Schlegel, S., Hjelm, A., Baumgarten, T., Vikström, D., and de Gier, J.-W. (**2014**). "Bacterial-based membrane protein production." *Biochimica et Biophysica Acta*, *1843*, 1739–1749.

[12] Ben-Tal, N., Ben-Shaul, A., Nicholls, A., and Honig, B. (**1996**). "Free-energy determinants of α-helix insertion into lipid bilayers." *Biophysical Journal*, *70*, 1803–1812.

[13] White, S. H., Ladokhin, A. S., Jayasinghe, S., and Hristova, K. (**2001**). "How membranes shape protein structure." *Journal of Biological Chemistry*, *276*, 32395–32398.

[14] Fiedler, S., Broecker, J., and Keller, S. (**2010**). "Protein folding in membranes." *Cellular and Molecular Life Sciences*, *67*, 1779–1798.

[15] Garavito, R. M. and Ferguson-Miller, S. (**2001**). "Detergents as tools in membrane biochemistry." *The Journal of Biological Chemistry*, *276*, 32403–32406.

[16] Tanford, C. (**1978**). "The hydrophobic effect and the organization of living matter." *Science*, *200*, 1012–1018.

[17] Fisher, L. R. and Oakenfull, D. G. (**1977**). "Micelles in aqueous solution." *Chemical Society Reviews*, *6*, 25–42.

[18] Bogusz, S., Venable, R. M., and Pastor, R. W. (**2000**). "Molecular dynamics simulations of octyl glucoside micelles : Structural properties." *Journal of Physical Chemistry B*, *104*, 5462–5470.

[19] Preston, W. C. (**1948**). "Some correlating principles of detergent action." *The Journal of Physical and Colloid Chemistry*, *52*, 84–97.

[20] Gunnarsson, G., Joensson, B., and Wennerstroem, H. (**1980**). "Surfactant association into micelles. An electrostatic approach." *Journal of Physical Chemistry*, *84*, 3114–3121.

[21] MacFarlane, C. B., Elworthy, P. H., and Gyane, D. O. (**1971**). "The effect of detergent concentration on monomer activity in a non-ionic detergent solution." *The Journal of Pharmacy and Pharmacology*, *23*, 33S–38S.

[22] Buboltz, J. T. and Feigenson, G. W. (**2005**). "Phospholipid solubility determined by equilibrium distribution between surface and bulk phases." *Langmuir*, *21*, 6296–6301.

[23] Kučerka, N., Tristram-Nagle, S., and Nagle, J. F. (**2006**). "Structure of fully hydrated fluid phase lipid bilayers with monounsaturated chains." *Journal of Membrane Biology*, *208*, 193–202.

[24] Ohki, S. and Arnold, K. (**1990**). "Surface dielectric constant, surface hydrophobicity and membrane fusion." *The Journal of Membrane Biology*, *114*, 195–203.

[25] White, S. H. and Wimley, W. C. (**1999**). "Membrane protein folding and stability: Physical principles." *Annual Review of Biophysics and Biomolecular Structure*, *28*, 319–365.

[26] Huang, W. and Levitt, D. G. (**1977**). "Theoretical calculation of the dielectric constant of a bilayer membrane." *Biophysical Journal*, *17*, 111–128.

[27] Chan, Y.-H. M. and Boxer, S. G. (**2007**). "Model membrane systems and their applications." *Current Opinion in Chemical Biology*, *11*, 581–587.

[28] Lagny, T. J. and Bassereau, P. (**2015**). "Bioinspired membrane-based systems for a physical approach of cell organization and dynamics: Usefulness and limitations." *Interface Focus*, *5*, 20150038–20150038.

[29] Fowler, P. W., Balali-Mood, K., Deol, S., Coveney, P. V., and Sansom, M. S. P. (**2007**). "Monotopic enzymes and lipid bilayers: A comparative study." *Biochemistry*, *46*, 3108–3115.

[30] Lau, T.-L. T.-L., Kim, C., Ginsberg, M. H., and Ulmer, T. S. (**2009**). "The structure of the integrin αIIbβ3 transmembrane complex explains integrin transmembrane signalling." *The EMBO Journal*, *28*, 1351–1361.

[31] Cortes, D. M. (**2001**). "Molecular architecture of full-length KcsA: Role of cytoplasmic domains in ion permeation and activation gating." *The Journal of General Physiology*, *117*, 165–180.

[32] Snijder, H., Kingma, R., Kalk, K., Dekker, N., Egmond, M., and Dijkstra, B. (**2001**). "Structural investigations of calcium binding and its role in activity and activation of outer membrane phospholipase A from *Escherichia coli*." *Journal of Molecular Biology*, *309*, 477–489.

[33] Tieleman, D. P., van der Spoel, D., and Berendsen, H. J. C. (**2000**). "Molecular dynamics simulations of dodecylphosphocholine micelles at three different aggregate sizes: Micellar structure and chain relaxation." *Journal of Physical Chemistry B*, *104*, 6380–6388.

[34] Blobel, G. (**1980**). "Intracellular protein topogenesis." *Proceedings of the National Academy of Sciences of the USA*, *77*, 1496–1500.

[35] Bocharov, E. V., Volynsky, P. E., Pavlov, K. V., Efremov, R. G., and Arseniev, A. S. (**2010**). "Structure elucidation of dimeric transmembrane domains of bitopic proteins." *Cell Adhesion & Migration*, *4*, 284–298.

[36] von Heijne, G. (**1994**). "Membrane proteins: From sequence to structure." *Annual Review of Biophysics and Biomolecular Structure*, *23*, 167–192.

[37] van Geest, M. and Lolkema, J. S. (**2000**). "Membrane topology and insertion of membrane proteins: Search for topogenic signals." *Microbiology and Molecular Biology Reviews : MMBR*, *64*, 13–33.

[38] von Heijne, G. (**2006**). "Membrane-protein topology." *Nature Reviews Molecular Cell Biology*, *7*, 909–918.

[39] Bowie, J. U. (**2013**). "Membrane protein twists and turns." *Science*, *339*, 398–399.

[40] MacCallum, J. L. and Tieleman, D. P. (**2011**). "Hydrophobicity scales: A thermodynamic looking glass into lipid-protein interactions." *Trends in Biochemical Sciences*, *36*, 653–662.

[41] Krishnakumar, S. S. and London, E. (**2007**). "Effect of sequence hydrophobicity and bilayer width upon the minimum length required for the formation of transmembrane helices in membranes." *Journal of Molecular Biology*, *374*, 671–687.

[42] Yohannan, S., Faham, S., Yang, D., Whitelegge, J. P., and Bowie, J. U. (**2004**). "The evolution of transmembrane helix kinks and the structural diversity of G protein-coupled receptors." *Proceedings of the National Academy of Sciences of the USA*, *101*, 959–963.

[43] Lee, A. G. (**2003**). "Lipid-protein interactions in biological membranes: A structural perspective." *Biochimica et Biophysica Acta*, *1612*, 1–40.

[44] Killian, J. A. and Nyholm, T. K. (**2006**). "Peptides in lipid bilayers: The power of simple models." *Current Opinion in Structural Biology*, *16*, 473–479.

[45] Rapp, M., Granseth, E., Seppälä, S., and von Heijne, G. (**2006**). "Identification and evolution of dual-topology membrane proteins." *Nature Structural & Molecular Biology*, *13*, 112–116.

[46] van Klompenburg, W. (**1997**). "Anionic phospholipids are determinants of membrane protein topology." *The EMBO Journal*, *16*, 4261–4266.

[47] Karp, E. S., Tiburu, E. K., Abu-Baker, S., and Lorigan, G. a. (**2006**). "The structural properties of the transmembrane segment of the integral membrane protein phospholamban utilizing ^{13}C CPMAS, ^{2}H, and REDOR solid-state NMR spectroscopy." *Biochimica et Biophysica Acta*, *1758*, 772–780.

[48] Vitrac, H., Bogdanov, M., Heacock, P., and Dowhan, W. (**2011**). "Lipids and topological rules of membrane protein assembly: Balance between long and short range lipid-protein interactions." *The Journal of Biological Chemistry*, *286*, 15182–15194.

[49] Geller, B., Zhu, H. Y., Cheng, S., Kuhn, A., and Dalbey, R. E. (**1993**). "Charged residues render pro-OmpA potential dependent for initiation of membrane translocation." *The Journal of Biological Chemistry*, *268*, 9442–9447.

[50] Ruta, V., Chen, J., and MacKinnon, R. (**2005**). "Calibrated measurement of gating-charge arginine displacement in the KvAP voltage-dependent K^+ channel." *Cell*, *123*, 463–475.

[51] Heijne, G. (**1986**). "The distribution of positively charged residues in bacterial inner membrane proteins correlates with the trans-membrane topology." *The EMBO Journal*, *5*, 3021–3027.

[52] Ulmschneider, M. B. and Sansom, M. S. (**2001**). "Amino acid distributions in integral membrane protein structures." *Biochimica et Biophysica Acta*, *1512*, 1–14.

[53] Esbjörner, E. K., Caesar, C. E. B., Albinsson, B., Lincoln, P., and Nordén, B. (**2007**). "Tryptophan orientation in model lipid membranes." *Biochemical and Biophysical Research Communications*, *361*, 645–650.

[54] Strandberg, E. and Killian, J. (**2003**). "Snorkeling of lysine side chains in transmembrane helices: How easy can it get?" *FEBS Letters*, *544*, 69–73.

[55] Rigaud, J. L., Pitard, B., and Lévy, D. (**1995**). "Reconstitution of membrane proteins into liposomes: Application to energy-transducing membrane proteins." *Biochimica et Biophysica Acta*, *1231*, 223–246.

[56] Ollivon, M., Lesieur, S., Grabielle-Madelmont, C., and Paternostre, M. (**2000**). "Vesicle reconstitution from lipid-detergent mixed micelles." *Biochimica et Biophysica Acta*, *1508*, 34–50.

[57] Rigaud, J. L., Chami, M., Lambert, O., Lévy, D., and Ranck, J. L. (**2000**). "Use of detergents in two-dimensional crystallization of membrane proteins." *Biochimica et Biophysica Acta*, *1508*, 112–128.

[58] Rigaud, J.-L. and Lévy, D. (**2003**). "Reconstitution of membrane proteins into liposomes." *Methods in Enzymology*, *372*, 65–86.

[59] Zhou, J. and Ritter, H. (**2010**). "Cyclodextrin functionalized polymers as drug delivery systems." *Polymer Chemistry*, *1*, 1552.

[60] Jiskoot, W., Teerlink, T., Beuvery, E. C., and Crommelin, D. J. A. (**1986**). "Preparation of liposomes via detergent removal from mixed micelles by dilution. The effect of bilayer composition and process parameters on liposome characteristics." *Pharmaceutisch Weekblad Scientific Edition*, *8*, 259–265.

[61] Racker, E., Violand, B., O'Neal, S., Alfonzo, M., and Telford, J. (**1979**). "Reconstitution, a way of biochemical research; some new approaches to membrane-bound enzymes." *Archives of Biochemistry and Biophysics*, *198*, 470–477.

[62] Jahnke, N., Krylova, O. O., Hoomann, T., Vargas, C., Fiedler, S., Pohl, P., and Keller, S. (**2014**). "Real-time monitoring of membrane-protein reconstitution by isothermal titration calorimetry." *Analytical Chemistry*, *86*, 920–927.

[63] Ruysschaert, T., Marque, A., Duteyrat, J.-L., Lesieur, S., Winterhalter, M., and Fournier, D. (**2005**). "Liposome retention in size exclusion chromatography." *BMC Biotechnology*, *5*, 11.

[64] Allen, T. M., Romans, A. Y., Kercret, H., and Segrest, J. P. (**1980**). "Detergent removal during membrane reconstitution". *Biochimica et Biophysica Acta*, *601*, 328–342.

[65] Reynolds, J. A., Nozaki, Y., and Tanford, C. (**1983**). "Gel-exclusion chromatography on S1000 sephacryl: Application to phospholipid vesicles." *Analytical Biochemistry*, *130*, 471–474.

[66] Lévy, D., Bluzat, A., Seigneuret, M., and Rigaud, J.-L. (**1990**). "A systematic study of liposome and proteoliposome reconstitution involving Bio-Bead-mediated Triton X-100 removal." *Biochimica et Biophysica Acta*, *1025*, 179–190.

[67] Rigaud, J. L., Mosser, G., Lacapere, J. J., Olofsson, A., Lévy, D., and Ranck, J. L. (**1997**). "Bio-Beads: An efficient strategy for two-dimensional crystallization of membrane proteins." *Journal of Structural Biology*, *118*, 226–235.

[68] Rigaud, J.-L., Lévy, D., Mosser, G., and Lambert, O. (**1998**). "Detergent removal by non-polar polystyrene beads." *European Biophysics Journal*, *27*, 305–319.

[69] Philippot, J., Mutaftschiev, S., and Liautard, J. (**1983**). "A very mild method allowing the encapsulation of very high amounts of macromolecules into very large (1000 nm) unilamellar liposomes." *Biochimica et Biophysica Acta*, *734*, 137–143.

[70] Young, H. S., Rigaud, J. L., Lacapère, J. J., Reddy, L. G., and Stokes, D. L. (**1997**). "How to make tubular crystals by reconstitution of detergent-solubilized Ca^{2+}-ATPase." *Biophysical Journal*, *72*, 2545–2558.

[71] de Grip, W., van Oostrum, J., and Bovee-Geurts, P. (**1998**). "Selective detergent-extraction from mixed detergent/lipid/protein micelles, using cyclodextrin inclusion compounds: A novel generic approach for the preparation of proteoliposomes." *Biochemical Journal*, *674*, 667–674.

[72] Signorell, G. a., Kaufmann, T. C., Kukulski, W., Engel, A., and Rémigy, H.-W. (**2007**). "Controlled 2D crystallization of membrane proteins using methyl-β-cyclodextrin." *Journal of Structural Biology*, *157*, 321–328.

[73] Broecker, J., Fiedler, S., Gimpl, K., and Keller, S. (**2014**). "Polar interactions trump hydrophobicity in stabilizing the self-inserting membrane protein mistic." *Journal of the American Chemical Society*, *136*, 13761–13768.

[74] Rekharsky, M. V. and Inoue, Y. (**1998**). "Complexation thermodynamics of cyclodextrins." *Chemical Reviews*, *98*, 1875–1918.

[75] Helenius, A., Sarvas, M., and Simons, K. (**1981**). "Asymmetric and symmetric membrane reconstitution by detergent elimination. Studies with Semliki-Forest-virus spike glycoprotein and penicillinase from the membrane of *Bacillus licheniformis*." *European Journal of Biochemistry*, *116*, 27–35.

[76] Jackson, M. L. and Litman, B. J. (**1985**). "Rhodopsin-egg phosphatidylcholine reconstitution by an octyl glucoside dilution procedure." *Biochimica et Biophysica Acta*, *812*, 369–376.

[77] Lasic, D. D. (**1988**). "The mechanism of vesicle formation." *Journal of Membrane Science*, *256*, 1–11.

[78] Engel, a., Hoenger, A., Hefti, A., Henn, C., Ford, R. C., Kistler, J., and Zulauf, M. (**1992**). "Assembly of 2-D membrane protein crystals: Dynamics, crystal order, and fidelity of structure analysis by electron microscopy." *Journal of Structural Biology*, *109*, 219–234.

[79] Milsmann, M. H., Schwendener, R. a., and Weder, H. G. (**1978**). "The preparation of large single bilayer liposomes by a fast and controlled dialysis." *Biochimica et Biophysica Acta*, *512*, 147–155.

[80] Textor, M., Vargas, C., and Keller, S. (**2015**). "Calorimetric quantification of linked equilibria in cyclodextrin/lipid/detergent mixtures for membrane-protein reconstitution." *Methods*, *76*, 183–193.

[81] Textor, M. and Keller, S. (**2016**). "Calorimetric quantification of cyclodextrin-mediated detergent extraction for membrane-protein reconstitution." *Methods in Enzymology*, *567*, 129–156.

[82] Roosild, T. P., Greenwald, J., Vega, M., Castronovo, S., Riek, R., and Choe, S. (**2005**). "NMR structure of Mistic, a membrane-integrating protein for membrane protein expression." *Science*, *307*, 1317–1321.

[83] Canlas, C. G., Cui, T., Li, L., Xu, Y., and Tang, P. (**2008**). "Anesthetic modulation of protein dynamics: Insight from an NMR study." *Journal of Physical Chemistry B*, *112*, 14312–14318.

[84] Xu, Y., Kong, J., and Kong, W. (**2013**). "Improved membrane protein expression in *Lactococcus lactis* by fusion to Mistic." *Microbiology (United Kingdom)*, *159*, 1002–1009.

[85] Choksupmanee, O., Hodge, K., Katzenmeier, G., and Chimnaronk, S. (**2012**). "Structural platform for the autolytic activity of an intact NS2B-NS3 protease complex from dengue virus." *Biochemistry*, *51*, 2840–2851.

[86] Gong, Z., Kessans, S. a., Song, L., Dörner, K., Lee, H.-H., Meador, L. R., LaBaer, J., Hogue, B. G., Mor, T. S., and Fromme, P. (**2014**). "Recombinant expression, purification, and biophysical characterization of the transmembrane and membrane proximal domains of HIV-1 gp41." *Protein Science*, *23*, 1607–1618.

[87] Nekrasova, O. V., Wulfson, A. N., Tikhonov, R. V., Yakimov, S. a., Simonova, T. N., Tagvey, A. I., Dolgikh, D. a., Ostrovsky, M. a., and Kirpichnikov, M. P. (**2010**). "A new hybrid protein for production of recombinant bacteriorhodopsin in *Escherichia coli*." *Journal of Biotechnology*, *147*, 145–150.

[88] Kahaki, F. A., Babaeipour, V., Memari, H. R., and Mofid, M. R. (**2014**). "High overexpression and purification of optimized bacterio-opsin from *Halobacterium Salinarum* R1 in *E. coli*." *Applied Biochemistry and Biotechnology*, *174*, 1558–1571.

[89] Lee, K. A., Lee, S.-S., Kim, S. Y., Choi, A. R., Lee, J.-H., and Jung, K.-H. (**2015**). "Mistic-fused expression of algal rhodopsins in *Escherichia coli* and its photochemical properties." *Biochimica et Biophysica Acta*, *1850*, 1694–1703.

[90] Kefala, G., Kwiatkowski, W., Esquivies, L., Maslennikov, I., and Choe, S. (**2007**). "Application of Mistic to improving the expression and membrane integration of histidine kinase receptors from *Escherichia coli*." *Journal of Structural and Functional Genomics*, *8*, 167–172.

[91] Blain, K. Y., Kwiatkowski, W., and Choe, S. (**2010**). "The functionally active mistic-fused histidine kinase receptor, EnvZ." *Biochemistry*, *49*, 9089–9095.

[92] Petrovskaya, L. E., Shulga, A. A., Bocharova, O. V., Ermolyuk, Y. S., Kryukova, E. A., Chupin, V. V., Blommers, M. J. J., Arseniev, A. S., and Kirpichnikov, M. P. (**2010**). "Expression of G-protein coupled receptors in *Escherichia coli* for structural studies." *Biochemistry (Mosc.)*, *75*, 881–891.

[93] Chowdhury, A., Feng, R., Tong, Q., Zhang, Y., and Xie, X. Q. (**2012**). "Mistic and TarCF as fusion protein partners for functional expression of the cannabinoid receptor 2 in *Escherichia coli*." *Protein Expression and Purification*, *83*, 128–134.

[94] Lyukmanova, E. N., Shenkarev, Z. O., Khabibullina, N. F., Kulbatskiy, D. S., Shulepko, M. a., Petrovskaya, L. E., Arseniev, a. S., Dolgikh, D. a., and Kirpichnikov, M. P. (**2012**). "N-terminal fusion tags for effective production of G-protein-coupled receptors in bacterial cell-free systems." *Acta Naturae*, *4*, 58–64.

[95] Lee, K. E., Kim, H. M., Lee, J. O., Jeon, H., and Han, S. S. (**2008**). "Regulation of CD40 reconstitution into a liposome using different ratios of solubilized LDAO to lipids." *Colloids and Surfaces B: Biointerfaces*, *62*, 51–57.

[96] Liu, X., Wu, L., Deng, G., Li, N., Chu, X., Guo, F., and Li, D. (**2008**). "Characterization of mitochondrial trifunctional protein and its inactivation study for medicine development." *Biochimica et Biophysica Acta*, *1784*, 1742–1749.

[97] Dvir, H. and Choe, S. (**2009**). "Bacterial expression of a eukaryotic membrane protein in fusion to various Mistic orthologs." *Protein Expression and Purification*, *68*, 28–33.

[98] Deniaud, A., Bernaudat, F., Frelet-Barrand, A., Juillan-Binard, C., Vernet, T., Rolland, N., and Pebay-Peyroula, E. (**2011**). "Expression of a chloroplast ATP/ADP transporter in *E. coli* membranes: Behind the Mistic strategy." *Biochimica et Biophysica Acta*, *1808*, 2059–2066.

[99] Dvir, H., Lundberg, M. E., Maji, S. K., Riek, R., and Choe, S. (**2009**). "Mistic: Cellular localization, solution behavior, polymerization, and fibril formation." *Protein Science*, *18*, 1564–1570.

[100] Psachoulia, E., Bond, P. J., and Sansom, M. S. P. (**2006**). "MD simulations of Mistic: Conformational stability in detergent micelles and water." *Biochemistry*, *45*, 9053–9058.

[101] Bröcker, J. (**2011**). "New approaches to studying membrane-protein stability and high-affinity protein-inhibitor interactions." PhD Thesis, University of Kaiserslautern.

[102] Debnath, D. K., Basaiawmoit, R. V., Nielsen, K. L., and Otzen, D. E. (**2011**). "The role of membrane properties in Mistic folding and dimerisation." *Protein Engineering Design Selection*, *24*, 89–97.

[103] Jacso, T., Franks, W. T., Rose, H., Fink, U., Broecker, J., Keller, S., Oschkinat, H., and Reif, B. (**2012**). "Characterization of membrane proteins in isolated native cellular membranes by dynamic nuclear polarization solid-state NMR spectroscopy without purification and reconstitution." *Angewandte Chemie International Edition*, *51*, 432–435.

[104] Sansom, M. S. P., Scott, K. A., and Bond, P. J. (**2008**). "Coarse-grained simulation: A high-throughput computational approach to membrane proteins." *Biochemical Society Transactions*, *36*, 27–32.

[105] Fiedler, S. (**2013**). "Thermodynamic stability of the α-helical membrane-interacting protein Mistic in detergent micelles." PhD Thesis, University of Potsdam.

[106] Dolinsky, T. J., Nielsen, J. E., McCammon, J. A., and Baker, N. A. (**2004**). "PDB2PQR: An automated pipeline for the setup of Poisson-Boltzmann electrostatics calculations." *Nucleic Acids Research*, *32*, W665–W667.

[107] Baker, N. A., Sept, D., Joseph, S., Holst, M. J., and McCammon, J. A. (**2001**). "Electrostatics of nanosystems: Application to microtubules and the ribosome." *Proceedings of the National Academy of Sciences of the USA*, *98*, 10037–10041.

[108] Jacso, T., Bardiaux, B., Broecker, J., Fiedler, S., Baerwinkel, T., Mainz, A., Fink, U., Vargas, C., Oschkinat, H., Keller, S., and Reif, B. (**2013**). "The mechanism of denaturation and the unfolded state of the α-helical membrane-associated protein Mistic." *Journal of the American Chemical Society*, *135*, 18884–18891.

[109] Marino, J., Bordag, N., Keller, S., and Zerbe, O. (**2015**). "Mistic's membrane association and its assistance in overexpression of a human GPCR are independent processes." *Protein Science*, *24*, 38–48.

[110] Roosild, T. P., Vega, M., Castronovo, S., and Choe, S. (**2006**). "Characterization of the family of Mistic homologues." *BMC Structural Biology*, *6*, 10.

[111] Lundberg, M. E., Becker, E. C., and Choe, S. (**2013**). "MstX and a putative potassium channel facilitate biofilm formation in *Bacillus subtilis*." *PloS One*, *8*, e60993.

[112] Prindle, A., Liu, J., Asally, M., Ly, S., Garcia-Ojalvo, J., and Süel, G. M. (**2015**). "Ion channels enable electrical communication in bacterial communities." *Nature*, *527*, 59–63.

[113] Skala, W., Goettig, P., and Brandstetter, H. (**2013**). "Do-it-yourself histidine-tagged bovine enterokinase: A handy member of the protein engineer's toolbox." *Journal of Biotechnology*, *168*, 421–425.

[114] Rath, H. (**2012**). "Production, purification, and biophysical characterisation of Mistic mutants." Master Thesis, University of Kaiserslautern.

[115] Olson, F., Hunt, C., Szoka, F., Vail, W., and Papahadjopoulos, D. (**1979**). "Preparation of liposomes of defined size distribution by extrusion through polycarbonate membranes." *Biochimica et Biophysica Acta*, *557*, 9–23.

[116] Gasteiger, E., Gattiker, A., Hoogland, C., Ivanyi, I., Appel, R. D., and Bairoch, A. (**2003**). "ExPASy: The proteomics server for in-depth protein knowledge and analysis." *Nucleic Acids Research*, *31*, 3784–3788.

[117] Rigaud, J. L., Paternostre, M. T., and Bluzat, A. (**1988**). "Mechanisms of membrane protein insertion into liposomes during reconstitution procedures involving the use of detergents. 2. Incorporation of the light-driven proton pump bacteriorhodopsin." *Biochemistry*, *27*, 2677–2688.

[118] Draczkowski, P., Matosiuk, D., and Jozwiak, K. (**2014**). "Isothermal titration calorimetry in membrane protein research." *Journal of Pharmaceutical and Biomedical Analysis*, *87*, 313–325.

[119] Keller, S., Vargas, C., Zhao, H., Piszczek, G., Brautigam, C. a., and Schuck, P. (**2012**). "High-precision isothermal titration calorimetry with automated peak-shape analysis." *Analytical Chemistry*, *84*, 5066–5073.

[120] Houtman, J. C. D., Brown, P. H., Bowden, B., Yamaguchi, H., Appella, E., Samelson, L. E., and Schuck, P. (**2007**). "Studying multisite binary and ternary protein interactions

by global analysis of isothermal titration calorimetry data in SEDPHAT: Application to adaptor protein complexes in cell signaling." *Protein Science*, *16*, 30–42.

[121] Brown, A. (**2009**). "Analysis of cooperativity by isothermal titration calorimetry." *International Journal of Molecular Sciences*, *10*, 3457–3477.

[122] Krylova, O. O., Jahnke, N., and Keller, S. (**2010**). "Membrane solubilisation and reconstitution by octylglucoside: Comparison of synthetic lipid and natural lipid extract by isothermal titration calorimetry." *Biophysical Chemistry*, *150*, 105–111.

[123] Ladokhin, A. S., Fernández-Vidal, M., and White, S. H. (**2010**). "CD spectroscopy of peptides and proteins bound to large unilamellar vesicles." *The Journal of Membrane Biologyiology*, *236*, 247–253.

[124] Warren, J. R. and Gordon, J. A. (**1966**). "On the refractive indices of aqueous solutions of urea." *Journal of Physical Chemistry*, *70*, 297–300.

[125] Wu, Y., Huang, H. W., and Olah, G. a. (**1990**). "Method of oriented circular dichroism." *Biophysical Journal*, *57*, 797–806.

[126] Bürck, J., Roth, S., Wadhwani, P., Afonin, S., Kanithasen, N., Strandberg, E., and Ulrich, A. S. (**2008**). "Conformation and membrane orientation of amphiphilic helical peptides by oriented circular dichroism." *Biophysical Journal*, *95*, 3872–3881.

[127] Clark, N. a., Rothschild, K. J., Luippold, D. a., and Simon, B. a. (**1980**). "Surface-induced lamellar orientation of multilayer membrane arrays. Theoretical analysis and a new method with application to purple membrane fragments." *Biophysical Journal*, *31*, 65–96.

[128] Davidsson, Å., Nordén, B., and Seth, S. (**1980**). "Measurement of oriented circular dichroism." *Chemical Physics Letters*, *70*, 313–316.

[129] Ladokhin, A. S., Jayasinghe, S., and White, S. H. (**2000**). "How to measure and analyze tryptophan fluorescence in membranes properly, and why bother?" *Analytical Biochemistry*, *285*, 235–245.

[130] Moro, F., Goni, F. M., and Urbaneja, M. a. (**1993**). "Fluorescence quenching at interfaces and the permeation of acrylamide and iodide across phospholipid bilayers." *FEBS Letters*, *330*, 129–132.

[131] Broecker, J. and Keller, S. (**2013**). "Impact of urea on detergent micelle properties." *Langmuir*, *29*, 8502–8510.

[132] McIntosh, T. J. and Holloway, P. W. (**1987**). "Determination of the depth of bromine atoms in bilayers formed from bromolipid probes." *Biochemistry*, *26*, 1783–1788.

[133] Ladokhin, A. S. (**1997**). "Distribution analysis of depth-dependent fluorescence quenching in membranes: A practical guide." *Methods in Enzymology*, *278*, 462–473.

[134] Chattopadhyay, A. and London, E. (**1987**). "Parallax method for direct measurement of membrane penetration depth utilizing fluorescence quenching by spin-labeled phospholipids." *Biochemistry*, *26*, 39–45.

[135] Ladokhin, A. S., Holloway, P., and Kostrzhevska, E. (**1993**). "Distribution analysis of membrane penetration of proteins by depth-dependent fluorescence quenching." *Journal of Fluorescence*, *3*, 195–197.

[136] Ladokhin, A. S. (**1999**). "Analysis of protein and peptide penetration into membranes by depth-dependent fluorescence quenching: Theoretical considerations." *Biophysical Journal*, *76*, 946–955.

[137] Ladokhin, A. S. (**2014**). "Measuring membrane penetration with depth-dependent fluorescence quenching: Distribution analysis is coming of age." *Biochimica et Biophysica Acta*, *1838*, 2289–2295.

[138] Ladokhin, A. S. (**1999**). "Evaluation of lipid exposure of tryptophan residues in membrane peptides and proteins." *Analytical Biochemistry*, *276*, 65–71.

[139] Hassan, P. a., Rana, S., and Verma, G. (**2015**). "Making Sense of brownian motion: Colloid characterization by dynamic light scattering." *Langmuir*, *31*, 3–12.

[140] Anderson, T. G., Tan, A., Ganz, P., and Seelig, J. (**2004**). "Calorimetric measurement of phospholipid interaction with methyl-β-cyclodextrin." *Biochemistry*, *43*, 2251–2261.

[141] Carvalho, M. C. (**2013**). "Integration of analytical instruments with computer scripting." *Journal of Laboratory Automation*, *18*, 328–33.

[142] Kemmer, G. and Keller, S. (**2010**). "Nonlinear least-squares data fitting in Excel spreadsheets." *Nature Protocols*, *5*, 267–281.

[143] Heerklotz, H., Lantzsch, G., Binder, H., Klose, G., and Blume, A. (**1995**). "Application of isothermal titration calorimetry for detecting lipid membrane solubilization." *Chemical Physics Letters*, *235*, 517–520.

[144] Wang, Z. X. (**1995**). "An exact mathematical expression for describing competitive binding of two different ligands to a protein molecule." *FEBS Letters*, *360*, 111–114.

[145] Krainer, G., Broecker, J., Vargas, C., Fanghänel, J., and Keller, S. (**2012**). "Quantifying high-affinity binding of hydrophobic ligands by isothermal titration calorimetry." *Analytical Chemistry*, *84*, 10715–10722.

[146] Krainer, G. and Keller, S. (**2015**). "Single-experiment displacement assay for quantifying high-affinity binding by isothermal titration calorimetry." *Methods*, *76*, 116–123.

[147] le Maire, M., Møller, J. V., and Champeil, P. (**1987**). "Binding of a nonionic detergent to membranes: Flip-flop rate and location on the bilayer." *Biochemistry*, *26*, 4803–4810.

[148] Wenk, M. R. and Seelig, J. (**1997**). "Vesicle-micelle transformation of phosphatidylcholine/octyl-β-D-glucopyranoside mixtures as detected with titration calorimetry." *Journal of Physical Chemistry B*, *101*, 5224–5231.

[149] Heerklotz, H. H., Binder, H., and Epand, R. M. (**1999**). "A "release" protocol for isothermal titration calorimetry." *Biophysical Journal*, *76*, 2606–2613.

[150] Heerklotz, H. and Seelig, J. (**2000**). "Titration calorimetry of surfactant-membrane partitioning and membrane solubilization." *Biochimica et Biophysica Acta*, *1508*, 69–85.

[151] Tsamaloukas, A. D., Keller, S., and Heerklotz, H. (**2007**). "Uptake and release protocol for assessing membrane binding and permeation by way of isothermal titration calorimetry." *Nature Protocols*, *2*, 695–704.

[152] Heerklotz, H. (**2008**). "Interactions of surfactants with lipid membranes." *Quarterly Reviews of Biophysics*, *41*, 205–264.

[153] Textor, M. and Keller, S. (**2015**). "Automated analysis of calorimetric demicellization titrations." *Analytical Biochemistry*, *485*, 119–121.

[154] Paula, S., Süs, W., Tuchtenhagen, J., and Blume, A. (**1995**). "Thermodynamics of micelle formation as a function of temperature: A high sensitivity titration calorimetry study." *Journal of Phyical Chemistry*, *99*, 11742–11751.

[155] Frotscher, E., Danielczak, B., Vargas, C., Meister, A., Durand, G., and Keller, S. (**2015**). "A fluorinated detergent for membrane-protein applications." *Angewandte Chemie International Edition*, *54*, 5069–5073.

[156] Heerklotz, H., Tsamaloukas, A. D., and Keller, S. (**2009**). "Monitoring detergent-mediated solubilization and reconstitution of lipid membranes by isothermal titration calorimetry." *Nature Protocols*, *4*, 686–697.

[157] Lichtenberg, D. (**1985**). "Characterization of the solubilization of lipid bilayers by surfactants." *Biochimica et Biophysica Acta*, *821*, 470–478.

[158] Lichtenberg, D., Robson, R. J., and Dennis, E. A. (**1983**). "Solubilization of phospholipids by detergents structural and kinetic aspects." *Biochimica et Biophysica Acta*, *737*, 285–304.

[159] Roth, Y., Opatowski, E., Lichtenberg, D., and Kozlov, M. M. (**2000**). "Phase behavior of dilute aqueous solutions of lipid−surfactant mixtures: Effects of finite size of micelles." *Langmuir*, *16*, 2052–2061.

[160] Mahammad, S. and Parmryd, I. (**2015**). "Cholesterol depletion using methyl-β-cyclodextrin." *Methods in Molecular Biology*, *1232*, 91–102.

[161] Tsamaloukas, A., Szadkowska, H., Slotte, P. J., and Heerklotz, H. (**2005**). "Interactions of cholesterol with lipid membranes and cyclodextrin characterized by calorimetry." *Biophysical Journal*, *89*, 1109–1119.

[162] Huang, Z. and London, E. (**2013**). "Effect of cyclodextrin and membrane lipid structure upon cyclodextrin-lipid interaction." *Langmuir*, *29*, 14631–14638.

[163] Loftsson, T., Jarho, P., Másson, M., and Järvinen, T. (**2005**). "Cyclodextrins in drug delivery." *Expert Opinion on Drug Delivery*, *2*, 335–351.

[164] Mehta, S., Bhasin, K., Dham, S., and Singla, M. (**2008**). "Micellar behavior of aqueous solutions of dodecyldimethylethylammonium bromide, dodecyltrimethylammonium chloride and tetradecyltrimethylammonium chloride in the presence of α-, β-, HPβ- and γ-cyclodextrins." *Journal of Colloid and Interface Science*, *321*, 442–451.

[165] Imaishi, Y., Kakehashi, R., Nezu, T., and Maeda, H. (**1998**). "Dodecyldimethylamine oxide micelles in solutions without added salt." *Journal of Colloid and Interface Science*, *197*, 309–316.

[166] Strop, P. and Brunger, A. (**2005**). "Refractive index-based determination of detergent concentration and its application to the study of membrane proteins." *Protein Science*, *14*, 2207–2211.

[167] Keller, S., Heerklotz, H., Jahnke, N., and Blume, A. (**2006**). "Thermodynamics of lipid membrane solubilization by sodium dodecyl sulfate." *Biophysical Journal*, *90*, 4509–4521.

[168] Uhríková, D., Kucerka, N., Islamov, A., Gordeliy, V., and Balgavý, P. (**2001**). "Small-angle neutron scattering study of *N*-dodecyl-*N*,*N*-dimethylamine *N*-oxide induced solubilization of dioleoylphosphatidylcholine bilayers in liposomes." *General physiology and biophysics*, *20*, 183–189.

[169] Lasala, R., Coudray, N., Abdine, A., Zhang, Z., Lopez-Redondo, M., Kirshenbaum, R., Alexopoulos, J., Zolnai, Z., Stokes, D., and Ubarretxena-Belandia, I. (**2015**). "Sparse and incomplete factorial matrices to screen membrane protein 2D crystallization." *Journal of Structural Biology*, *189*, 123–134.

[170] Mao, D. and Wallace, B. a. (**1984**). "Differential light scattering and absorption flattening optical effects are minimal in the circular dichroism spectra of small unilamellar vesicles." *Biochemistry*, *23*, 2667–2673.

[171] Wallace, B. a. and Mao, D. (**1984**). "Circular dichroism analyses of membrane proteins: An examination of differential light scattering and absorption flattening effects in large membrane vesicles and membrane sheets." *Analytical Biochemistry*, *142*, 317–328.

[172] Wallace, B. a. and Teeters, C. L. (**1987**). "Differential absorption flattening optical effects are significant in the circular dichroism spectra of large membrane fragments." *Biochemistry*, *26*, 65–70.

[173] Pencer, J., White, G. F., and Hallett, F. R. (**2001**). "Osmotically induced shape changes of large unilamellar vesicles measured by dynamic light scattering." *Biophysical Journal*, *81*, 2716–2728.

[174] Eftink, M. R. and Ghiron, C. A. (**1976**). "Fluorescence quenching of indole and model micelle systems." *Journal of Physical Chemistry*, *80*, 486–493.

[175] Eftink, M. R. and Ghiron, C. A. (**1981**). "Fluorescence quenching studies with proteins." *Analytical Biochemistry*, *114*, 199–227.

[176] Bastyns, K. and Engelborghs, Y. (**1992**). "Acrylamide quenching of the fluorescence of glyceraldehyde-3-phosphate dehydrogenase: Reversible and irreversible effects." *Photochemistry and Photobiology*, *55*, 9–16.

[177] Sommer, L. A. M., Janke, J. J., Bennett, W. F. D., Bürck, J., Ulrich, A. S., Tieleman, D. P., and Dames, S. A. (**2014**). "Characterization of the immersion properties of the peripheral membrane anchor of the FATC domain of the kinase "Target of Rapamycin" by NMR, oriented CD spectroscopy, and MD simulations." *Journal of Physical Chemistry B*, *118*, 4817–4831.

[178] Kragh-Hansen, U., le Maire, M., and Møller, J. V. (**1998**). "The mechanism of detergent solubilization of liposomes and protein-containing membranes." *Biophysical Journal*, *75*, 2932–2946.

[179] Lichtenberg, D., Ahyayauch, H., and Goñi, F. M. (**2013**). "The mechanism of detergent solubilization of lipid bilayers." *Biophysical Journal*, *105*, 289–299.

[180] Stuart, M. C. a. and Boekema, E. J. (**2007**). "Two distinct mechanisms of vesicle-to-micelle and micelle-to-vesicle transition are mediated by the packing parameter of phospholipid-detergent systems." *Biochimica et Biophysica Acta*, *1768*, 2681–2689.

[181] Heerklotz, H., Szadkowska, H., Anderson, T., and Seelig, J. (**2003**). "The sensitivity of lipid domains to small perturbations demonstrated by the effect of triton." *Journal of Molecular Biology*, *329*, 793–799.

[182] Ho, J. K. (**2002**). "Interactions of acyl carnitines with model membranes: A ^{13}C-NMR study." *The Journal of Lipid Research*, *43*, 1429–1439.

[183] Classen, J., Deuticke, B., and Haest, C. W. (**1989**). "Nonmediated flip-flop of phospholipid analogues in the erythrocyte membrane as probed by palmitoylcarnitine: Basic properties and influence of membrane modification." *The Journal of Membrane Biology*, *111*, 169–178.

[184] Cócera, M., Lopez, O., Coderch, L., Parra, J., and de la Maza, A. (**1999**). "Influence of the level of ceramides on the permeability of stratum corneum lipid liposomes caused by a C12-betaine/sodium dodecyl sulfate mixture." *International Journal of Pharmaceutics*, *183*, 165–173.

[185] Toro, C., Sanchez, S., Zanocco, A., Lemp, E., Gratton, E., and Gunther, G. (**2009**). "Solubilization of lipid bilayers by myristyl sucrose ester: Effect of cholesterol and phospholipid head group size." *Chemistry and Physics of Lipids*, *157*, 104–112.

[186] Heerklotz, H. (**2001**). "Membrane stress and permeabilization induced by asymmetric incorporation of compounds." *Biophysical Journal*, *81*, 184–195.

[187] Elsayed, M. M. and Cevc, G. (**2011**). "The vesicle-to-micelle transformation of phospholipid–cholate mixed aggregates: A state of the art analysis including membrane curvature effects." *Biochimica et Biophysica Acta*, *1808*, 140–153.

[188] Cabral, D. J., Small, D. M., Lilly, H. S., and Hamilton, J. a. (**1987**). "Transbilayer movement of bile acids in model membranes." *Biochemistry*, *26*, 1801–1804.

[189] Keller, S., Heerklotz, H., and Blume, A. (**2006**). "Monitoring lipid membrane translocation of sodium dodecyl sulfate by isothermal titration calorimetry." *Journal of the American Chemical Society*, *128*, 1279–1286.

[190] Contreras, F.-X., Sánchez-Magraner, L., Alonso, A., and Goñi, F. M. (**2010**). "Transbilayer (flip–flop) lipid motion and lipid scrambling in membranes." *FEBS Letters*, *584*, 1779–1786.

[191] Tsianou, M. and Fajalia, A. I. (**2014**). "Cyclodextrins and surfactants in aqueous solution above the critical micelle concentration: Where are the cyclodextrins located?" *Langmuir*, *30*, 13754–13764.

[192] Lasic, D. D. (**1982**). "A molecular model for vesicle formation." *Biochimica et Biophysica Acta*, *692*, 501–502.

[193] Lomize, A. L., Pogozheva, I. D., Lomize, M. a., and Mosberg, H. I. (**2006**). "Positioning of proteins in membranes: A computational approach." *Protein Science*, *15*, 1318–1333.

[194] Lasic, D. D., Martin, F. J., Neugebauer, J. M., and Kratohvil, J. P. (**1989**). "Phospholipid vesicles from mixed micelles of egg yolk lecithin and a zwitterionic detergent (CHAPS)." *Journal of Colloid and Interface Science*, *133*, 539–544.

[195] Cevc, G. and Richardsen, H. (**1999**). "Lipid vesicles and membrane fusion." *Advanced Drug Delivery Reviews*, *38*, 207–232.

[196] Oliver, R. C., Lipfert, J., Fox, D. A., Lo, R. H., Doniach, S., and Columbus, L. (**2013**). "Dependence of micelle size and shape on detergent alkyl chain length and head group." *PLoS One*, *8*, e62488.

[197] Danielczak, B. (**2015**). "Outer membrane phospholipase A: Folding and water permeability studies." Master Thesis, University of Kaiserslautern.

[198] Marino, J., Geertsma, E. R., and Zerbe, O. (**2012**). "Topogenesis of heterologously expressed fragments of the human Y4 GPCR." *Biochimica et Biophysica Acta*, *1818*, 3055–3063.

[199] Xie, H., Guo, X.-M., and Chen, H. (**2009**). "Making the most of fusion tags technology in structural characterization of membrane proteins." *Molecular Biotechnology*, *42*, 135–145.

[200] Rapp, M., Drew, D., Daley, D., Nilsson, J., Carvalho, T., Melen, K., De Gier, J. W., and von Heijne, G. (**2004**). "Experimentally based topology models for *E. coli* inner membrane proteins." *Protein Science*, *13*, 937–945.

[201] Daley, D. O. (**2005**). "Global topology analysis of the *Escherichia coli* inner membrane proteome." *Science*, *308*, 1321–1323.

[202] Kim, H., Melen, K., Osterberg, M., and von Heijne, G. (**2006**). "A global topology map of the *Saccharomyces cerevisiae* membrane proteome." *Proceedings of the National Academy of Sciences of the USA*, *103*, 11142–11147.

[203] Hebling, C. M., Morgan, C. R., Stafford, D. W., Jorgenson, J. W., Rand, K. D., and Engen, J. R. (**2010**). "Conformational analysis of membrane proteins in phospholipid bilayer nanodiscs by hydrogen exchange mass spectrometry." *Analytical Chemistry*, *82*, 5415–5419.

[204] von Heijne, G. (**1992**). "Membrane protein structure prediction. Hydrophobicity analysis and the positive-inside rule." *Journal of Molecular Biology*, *225*, 487–494.

[205] Felder, C. E., Prilusky, J., Silman, I., and Sussman, J. L. (**2007**). "A server and database for dipole moments of proteins." *Nucleic Acids Research*, *35*, W512–W521.

[206] Wassenaar, T. A., Pluhackova, K., Böckmann, R. A., Marrink, S. J., and Tieleman, D. P. (**2014**). "Going backward: A flexible geometric approach to reverse transformation from coarse grained to atomistic models." *Journal of Chemical Theory and Computation*, *10*, 676–690.

[207] Lindahl, E., Hess, B., and van der Spoel, D. (**2001**). "GROMACS 3.0: A package for molecular simulation and trajectory analysis." *Journal of Molecular Modelling*, *7*, 306–317.

[208] Bennett, W. D. and Tieleman, D. P. (**2011**). "Water defect and pore formation in atomistic and coarse-grained lipid membranes: Pushing the limits of coarse graining." *Journal of Chemical Theory and Computation*, *7*, 2981–2988.

[209] Johansson, A. C. V. and Lindahl, E. (**2009**). "Titratable amino acid solvation in lipid membranes as a function of protonation state." *Journal of Physical Chemistry B*, *113*, 245–253.

[210] Moon, C. P. and Fleming, K. G. (**2011**). "Side-chain hydrophobicity scale derived from transmembrane protein folding into lipid bilayers." *Proceedings of the National Academy of Sciences of the USA*, *108*, 10174–10177.

[211] Callenberg, K. M., Latorraca, N. R., and Grabe, M. (**2012**). "Membrane bending is critical for the stability of voltage sensor segments in the membrane." *The Journal of General Physiology*, *140*, 55–68.

[212] Honig, B. and Hubbell, W. (**1984**). "Stability of "salt bridges" in membrane proteins." *Proceedings of the National Academy of Sciences of the USA*, *81*, 5412–5416.

[213] Maxfield, F. and Scheraga, H. (**1975**). "The effect of neighboring charges on the helix forming ability of charged amino acids in proteins." *Macromolecules*, *8*, 491–493.

[214] Yang, Z., Lasker, K., Schneidman-Duhovny, D., Webb, B., Huang, C. C., Pettersen, E. F., Goddard, T. D., Meng, E. C., Sali, A., and Ferrin, T. E. (**2012**). "UCSF Chimera, MODELLER, and IMP: An integrated modeling system." *Journal of Structural Biology*, *179*, 269–278.

[215] Li, L. B., Vorobyov, I., and Allen, T. W. (**2012**). "The role of membrane thickness in charged protein-lipid interactions." *Biochimica et Biophysica Acta*, *1818*, 135–145.

[216] Li, L., Vorobyov, I., and Allen, T. W. (**2013**). "The different interactions of lysine and arginine side chains with lipid membranes." *Journal of Physical Chemistry B*, *117*, 11906–11920.

[217] Mehler, E., Fuxreiter, M., Simon, I., and Garcia-Moreno E, B. (**2002**). "The role of hydrophobic microenvironments in modulating pK_a shifts in proteins." *Proteins: Structure, Function, and Genetics*, *48*, 283–292.

[218] Panahi, A. and Brooks, C. L. (**2015**). "Membrane environment modulates the pK_a values of transmembrane helices." *Journal of Physical Chemistry B*, *119*, 4601–4607.

[219] Flewelling, R. F. and Hubbell, W. L. (**1986**). "The membrane dipole potential in a total membrane potential model. Applications to hydrophobic ion interactions with membranes." *Biophysical Journal*, *49*, 541–552.

[220] Clarke, R. J. (**2001**). "The dipole potential of phospholipid membranes and methods for its detection." *Advances in Colloid and Interface Science*, *89-90*, 263–281.

[221] Wang, L. (**2012**). "Measurements and implications of the membrane dipole potential." *Annual Review of Biochemistry*, *81*, 615–635.

[222] Zhan, H. and Lazaridis, T. (**2012**). "Influence of the membrane dipole potential on peptide binding to lipid bilayers." *Biophysical Chemistry*, *161*, 1–7.

[223] Brockman, H. (**1994**). "Dipole potential of lipid membranes." *Chemistry and Physics of Lipids*, *73*, 57–79.

[224] Hartmann, A., Krainer, G., Keller, S., and Schlierf, M. (**2015**). "Quantification of millisecond protein-folding dynamics in membrane-mimetic environments by single-molecule Förster resonance energy transfer spectroscopy." *Analytical Chemistry*, *87*, 11224–11232.

[225] Reid, K., Lindley, P., and Thornton, J. (**1985**). "Sulphur-aromatic interactions in proteins." *FEBS Letters*, *190*, 209–213.

[226] Pal, D. and Chakrabarti, P. (**2001**). "Non-hydrogen bond interactions involving the methionine sulfur atom." *Journal of Biomolecular Structure and Dynamics*, *19*, 115–128.

[227] Valley, C. C., Cembran, A., Perlmutter, J. D., Lewis, A. K., Labello, N. P., Gao, J., and Sachs, J. N. (**2012**). "The methionine-aromatic motif plays a unique role in stabilizing protein structure." *The Journal of Biological Chemistry*, *287*, 34979–34991.

[228] Gregoret, L. M., Rader, S. D., Fletterick, R. J., and Cohen, F. E. (**1991**). "Hydrogen bonds involving sulfur atoms in proteins." *Proteins: Structure, Function, and Genetics*, *9*, 99–107.

[229] Biswal, H. S., Gloaguen, E., Loquais, Y., Tardivel, B., and Mons, M. (**2012**). "Strength of NH···S hydrogen bonds in methionine residues revealed by gas-phase IR/UV spectroscopy." *Journal of Physical Chemistry Letters*, *3*, 755–759.

[230] Mashl, R. J., Scott, H. L., Subramaniam, S., and Jakobsson, E. (**2001**). "Molecular simulation of dioleoylphosphatidylcholine lipid bilayers at differing levels of hydration." *Biophysical Journal*, *81*, 3005–3015.

[231] Peterson, U., Mannock, D. A., Lewis, R. N., Pohl, P., McElhaney, R. N., and Pohl, E. E. (**2002**). "Origin of membrane dipole potential: Contribution of the phospholipid fatty acid chains." *Chemistry and Physics of Lipids*, *117*, 19–27.

[232] Honig, B., Hubbell, W. L., and Flewelling, R. F. (**1986**). "Electrostatic interactions in membranes and proteins." *Annual Review of Biophysics and Biophysical Chemistry*, *15*, 163–193.

[233] Samuilov, V. D. and Khakimov, S. A. (**1991**). "Dependence of *Bacillus subtilis* cell respiration on monovalent cations." *Biochemistry (Mosc.)*, *56*, 1209–1214.

[234] Eisenstadt, E. (**1972**). "Potassium content during growth and sporulation in *Bacillus subtilis*." *Journal of Bacteriology*, *112*, 264–267.

[235] Holtmann, G., Bakker, E. P., Uozumi, N., and Bremer, E. (**2003**). "KtrAB and KtrCD: Two K^+ uptake systems in *Bacillus subtilis* and their role in adaptation to hypertonicity." *Journal of Bacteriology*, *185*, 1289–1298.

[236] Kinsinger, R. F., Shirk, M. C., and Fall, R. (**2003**). "Rapid surface motility in *Bacillus subtilis* is dependent on extracellular surfactin and potassium ion." *Journal of Bacteriology*, *185*, 5627–5631.

[237] Kinsinger, R. F., Kearns, D. B., Hale, M., and Fall, R. (**2005**). "Genetic requirements for potassium ion-dependent colony spreading in *Bacillus subtilis*." *Journal of Bacteriology*, *187*, 8462–8469.

[238] Fujisawa, M., Wada, Y., and Ito, M. (**2004**). "Modulation of the K^+ efflux activity of *Bacillus subtilis* YhaU by YhaT and the C-terminal region of YhaS." *FEMS Microbiology Letters*, *231*, 211–217.

[239] Hansen, S. K., Bertelsen, K., Paaske, B., Nielsen, N. C., and Vosegaard, T. (**2015**). "Solid-state NMR methods for oriented membrane proteins." *Progress in Nuclear Magnetic Resonance Spectroscopy*, *88-89*, 48–85.

[240] Prosser, R. S., Evanics, F., Kitevski, J. L., and Al-Abdul-Wahid, M. S. (**2006**). "Current applications of bicelles in NMR studies of membrane-associated amphiphiles and proteins." *Biochemistry*, *45*, 8453–8465.

[241] Bogdanov, M., Zhang, W., Xie, J., and Dowhan, W. (**2005**). "Transmembrane protein topology mapping by the substituted cysteine accessibility method (SCAM): Application to lipid-specific membrane protein topogenesis." *Methods*, *36*, 148–171.

[242] Islam, S. T. and Lam, J. S. (**2013**). "Topological mapping methods for α-helical bacterial membrane proteins - an update and a guide." *MicrobiologyOpen*, *2*, 350–364.

[243] Al-Abdul-Wahid, M. S., Neale, C., Pomes, R., and Prosser, R. S. (**2009**). "A solution NMR approach to the measurement of amphiphile immersion depth and orientation in membrane model systems." *Journal of the American Chemical Society*, *131*, 6452–6459.

[244] Al-Abdul-Wahid, M. S., Verardi, R., Veglia, G., and Prosser, R. S. (**2011**). "Topology and immersion depth of an integral membrane protein by paramagnetic rates from dissolved oxygen." *Journal of Biomolecular NMR*, *51*, 173–183.

[245] Sarkar, P. and Chattopadhyay, A. (**2016**). "Micellar dipole potential is sensitive to sphere-to-rod transition." *Chemistry and Physics of Lipids*, *195*, 34–38.

[246] Bagatolli, L. A. (**2015**). "Monitoring membrane hydration with 2-(dimethylamino)-6-acylnaphtalenes fluorescent probes." *Subcellular Biochemistry*, *71*, 105–125.

[247] Nakao, H., Ikeda, K., Iwamoto, M., Shimizu, H., Oiki, S., Ishihama, Y., and Nakano, M. (**2015**). "pH-dependent promotion of phospholipid flip–flop by the KcsA potassium channel." *Biochimica et Biophysica Acta*, *1848*, 145–50.

[248] Clejan, S., Krulwich, T. a., Mondrus, K. R., and Seto-Young, D. (**1986**). "Membrane lipid composition of obligately and facultatively alkalophilic strains of *Bacillus* spp." *Journal Of Bacteriology*, *168*, 334–340.

Appendix

List of Figures

List of Tables

Abbreviations

AIX	anion exchange
aq	aqueous phase (superscript)
a.u.	arbitrary units
b	bilayer phase (superscript)
c	concentration
CD	circular dichroism
CyD	cyclodextrin
CMC	critical micelle concentration
D	detergent (subscript)
DA	distribution analysis
DDFQ	depth-dependent fluorescence quenching
DDM	*n*-dodecyl-β-D-maltopyranoside
demic	demicellization (subscript)
DFQP	depth-dependent fluorescence quenching profile
d_h	mean hydrodynamic diameter
DLPC	1,2-dilauroyl-*sn*-glycero-3-phosphocholine
DLS	dynamic light scattering
DM	*n*-decyl-β-D-maltopyranoside
DMPC	1,2-dimyristoyl-*sn*-glycero-3-phosphocholine
DPC	*n*-dodecyl phosphocholine
DPPC	1,2-dipalmitoyl-*sn*-glycero-3-phosphocholine
DIT	digital integration time
DTT	1,4-dithio-DL-threitol
EDTA	ethylenediamine tetraacetic acid

EK	enterokinase
EtOH	ethanol
ε	molar extinction coefficient
F	fluorescence intensity in the presence of quencher
F_0	fluorescence intensity in the absence of quencher
HPβCD	2-hydroxypropyl-β-cyclodextrin
h_m	mean depth
hw	half width at half-maximum (superscript)
I_{em}	emission intensity
i	inclusion complex (superscript)
IMAC	immobilised-metal affnity chromatography
IPTG	isopropyl-β-thiogalactopyranoside
ITC	isothermal titration calorimetry
kan	kanamycin
L	lipid (subscript)
LB	lysogeny broth
LD	linear dichroism
LDAO	*n*-dodecyl-*N,N*-dimethylamine-*N*-oxide
LPR	(molar) lipid/protein ratio
LUV	large unilamellar vesicle
λ_{em}	emission wavelength
λ_{ex}	excitation wavelength
m	micellar phase (superscript)
MβCD	methyl-β-cyclodextrin
MCR	mean count rate
MD	molecular dynamics
Mistic	membrane-integrating sequence for translation of integral membrane-protein constructs (acronym)
MP	membrane protein
MWCO	molecular weight cut-off
n	normalized (superscript)
NaCl	sodium chloride
NaN_3	sodium azide
NATA	*N*-acetyl-L-tryptophanamide
NLSF	nonlinear least-squares fit
NMR	nuclear magnetic resonance

OCD	oriented circular dichroism
OD	optical density
OM	*n*-octyl-β-D-maltopyranoside
x-*y*BrPC	1-palmitoyl-2-(*x*,*y*-dibromo)stearoyl-*sn*-glycero-3-phosphocholine
PDI	polydispersity index
PM	parallax method
POPC	1-palmitoyl-2-oleoyl-*sn*-glycero-3-phosphocholine
Ψ_d	membrane dipole potential
RT	room temperature
σ	dispersion
S	area of DFQP
SAT	saturation
SOL	solubilization
syr	injection syringe (superscript)
θ_{MRW}	mean residue molar ellipticity
TM	transmembrane
TOE	DL-tryptophan octyl ester
Tris	tris(hydroxymethyl)-aminomethane
Triton X-100	α-[4-(1,1,3,3-tetramethylbutyl)phenyl]ω-hydroxypoly(oxy-1,2-ethanediyl)
W	water (subscript)

List of Intractable Measurements and Bad Outcomes (LIMBO)

Goal	Method	Reasons for Failure
Determine rotational orientation of Mistic in a POPC bilayer	Linear dichroism (LD) spectroscopy[1]	• Large vesicle-entailed light scattering in the far-UV range, where absorption arising from transition dipole moments (TDMs) of α-helices is most pronounced. • Deconvolution of LD spectra comprising bands corresponding to multiple TDMs would be required. TDMs include those of α-helices, tryptophan residues, and tyrosine residues, with each of these residues in turn being characterized by multiple TDMs. • Time-dependent increase in spectrum amplitude due to shear-induced vesicle fusion in Couette cell.
Determine W13 insertion depth by 10-doxylnonadecane (10-DN) quenching	Fluorescence spectroscopy	• Quenching efficiency did not increase monotonically with molar fraction of 10-DN, but showed maximal values at 6% and 12%.
Quantify components in a complex reconstitution mixture	Infrared (IR) spectroscopy	• Overlapping bands of POPC/LDAO and HPβCD/Mistic. DirectDetect (Millipore) provides no signal in the range 1100–1300 cm^{-1}. • Sloping and varying baseline despite subtraction of blanks. Thus, insufficient precision of ∼0.5 mM.
	Thin layer chromatography (TLC)	• Insufficient detection limit of ∼0.5 mM.
Removal of cyclodextrin (CyD)/detergent inclusion complex	Dialysis	• CyD affects permeation behaviour of dialysis membrane, resulting in loss of protein even with lowest MWCO.
	Size exclusion chromatography (SEC)	• Substantial lipid retention on column matrix of ∼40%. • Results in dilution of the sample and, thus, requires subsequent concentration step that eliminates control over final concentrations.
	Differential centrifugation	• Density of POPC/Mistic proteoliposomes too low, preventing sedimentation even at prolonged durations (over night) and low sucrose concentrations of the step gradient (5 to 10%).
Verify membrane association of Mistic by demonstrating different diffusion of labeled variants in micelles and vesicles	Microscale thermophoresis (MST)	• Inadequate instrument reproducibility, even for repeat measurements of identical samples at identical experimental parameters.
Co-crystallization with Ca^{2+}-ATPase for cryo-electron microscopy (EM)	2D-crystallization	• Limited time and trial-end-error approach allowed only for the acquirement of a single 2D-crystal.
Monitor reconstitutions at very slow rates of detergent removal to assess impact on vesicle size	Dynamic light scattering (DLS)	• Unstable instrument software. Software repeatedly crashed after a few hours, preventing prolonged automated titrations.
Perform reconstitutions with phospholipids of shorter alkyl chain length, namely, DLPC and DMPC	CyD-mediated reconstitution	• Substantial binding of DLPC by both CyDs tested. Phase transition temperature of DMPC (24°C) would require to perform all steps at considerably higher temperatures (including shipping of samples to Karlsruhe for OCD measurements).

[1] Aside from small peptides, there are only a few examples where rotational orientation of an MP was elucidated by LD spectroscopy, such as done for cytochrome c (Caesar, C. E. B., Esbjörner, E. K., Lincoln, P., & Nordén, B. (**2009**). "Assigning membrane binding geometry of cytochrome c by polarized light spectroscopy." *Biophysical Journal*, *96*, 3399-–3411). This protein is a thankful model protein, as it harbors a heme cofactor that can be exploited as an additional chromophore.

Acknowledgements

This thesis could not have been accomplished without the continued support and involvement of many people. In particular, I thank:

- Prof. Sandro Keller (Molecular Biophysics, University of Kaiserslautern) for his outstanding commitment in supervising this work, for both scientific and personal guidance, and for helping me in becoming more optimistic;
- Prof. Johannes Herrmann (Cell Biology, University of Kaiserslautern) for stimulating discussions and for agreeing to act as the second adviser for this thesis;
- Dr. Torsten Möhlmann (Plant Physiology, University of Kaiserslautern) for agreeing to act as co-supervisor and for helpful discussions;
- Prof. Jan Riemer (Department of Chemistry, University of Cologne) and his former group members of Cellular Biochemistry at the University of Kaiserslautern for stimulating discussions and for providing access to fluorescence spectrometer and cold room;
- Dr. Jana Bröcker, Dr. Sebastian Fiedler (both University of Toronto), and Henryke Rath for helpful advice on Mistic, in particular, regarding production and purification at the beginning of my project;
- Dr. Wolfgang Skala (Department of Molecular Biology, University of Salzburg) for providing both the enterokinase plasmid as well as the protocol for enterokinase production and purification;
- Dr. Michael Schlierf, Georg Krainer, and Andreas Hartmann (B Cube, Center for Biological Engineering, University of Dresden) for helpful discussions, for giving me insight into single-molecule FRET, for sharing data, and for providing labeled Mistic variants for MST trials;
- Prof. Howard Young (Department of Biochemistry, University of Alberta) for agreeing to act as co-supervisor and for hosting me, and together with his former group members Dr. Jessica Gifford, Dr. Muhammad Bashir Khan, Catharine Trieber, Joseph Primeau, and Gareth Armanious for letting me have an exciting stay abroad;

- Dr. Jochen Bürck, Siegmar Roth, and Bianca Posselt (Department of Molecular Biophysics IBG-2, Karlsruhe Institute for Technology) for letting me perform SRCD and OCD measurements, for interesting discussions, and for being great hosts;

- PD Dr. Holger Becker (Zoology, University of Kaiserslautern) for providing access to the IR spectrometer;

- Dr. Kristyna Pluhackova (Computational Biology, University of Erlangen-Nuremberg) for back-mapping the coarse-grained MD simulation snapshot of Mistic, and for providing detailed advice on how to perform MD simulations;

- Dr. Gabriele Amoroso (Plant Physiology, University of Kaiserslautern) for organization of the IRTG 1830 graduate school and for giving helpful advice on administrative issues;

- the German National Academic Foundation for providing my PhD scholarship and the Deutsche Forschungsgemeinschaft (DFG) for funding;

- all members of the IRTG 1830 "Complex Membrane Proteins in Cellular Development and Disease", both from Germany and Canada, for exciting insights into a diverse set of projects and for interesting symposia and post-symposium meetings; thanks in particular to Aruna Augustine for a lot of support during my stay in Edmonton;

- all colleagues of the AG Keller, for the most intriguing discussions, for enjoyable and fun times both in and outside the lab, and for the encouragement, in particular to Dr. Carolyn Vargas, Andreas Werle-Rutter, Jessica Klement, Benjamin Klement, Katharina Gimpl, Rodrigo Cuevas Arenas, and Markus Fleisch. I am thankful, in particular, to Johannes Klingler, Erik Frotscher, and Bartholomäus Danielczak for helpful comments on the manuscript. Also thanks to old and new members, in particular Jonas Dörr, Sebastian Unger, Anne Grethen, Johannes Schnur, Abraham Olusegun Oluwole, and thanks to Ina Heimann for letting me use the Auto-iTC$_{200}$;

- the neighbours from the Nano Structuring Center (University of Kaiserslautern), in particular Christian Dautermann for support with virtually any technical problem;

- the neighbours from AG Kins (Human Biology, University of Kaiserslautern);

- Waldemar Windholz for being a great neighbor and friend;

- all my friends and my family, in particular my parents, for continuous support.

List of Publications

- Textor, M., Keller, S. (**2015**). "Calorimetric Quantification of Cyclodextrin-Mediated Detergent Extraction for Membrane-Protein Reconstitution", *Methods in Enzymology*, submitted.
- Textor, M., Keller, S. (**2015**). "Automated Analysis of Calorimetric Demicellization Titrations.", *Analytical Biochemistry*, *485*, 119–121.
- Herrmann M., Danielczak B., Textor, M., Klement J., Keller S. (**2015**). "Modulating Bilayer Mechanical Properties to Promote the Coupled Folding and Insertion of an Integral Membrane Protein.", *European Biophysics Journal*, *44*, 503–512.
- Textor, M., Vargas, C., Keller, S. (**2015**). "Calorimetric Quantification of Linked Equilibria in Cyclodextrin/Lipid/Detergent Mixtures for Membrane–Protein Reconstitution", *Methods*, *76*, 183–193.
- Lusiastuti, A.M., Textor, M., Seeger, H., Akineden, O., Zschöck, M. (**2012**). "The Occurrence of *Streptococcus agalactiae* Sequence Type 261 from Fish Disease Outbreaks of Tilapia *Oreochromis niloticus* in Indonesia", *Aquaculture Research*, *45*, 1260–1263.

Curriculum Vitae

Personal Information

Name	Martin Textor

Academic Career

06/2012—12/2015	PhD student in the Molecular Biophysics Departure, University of Kaiserslautern, with Prof. Dr. Sandro Keller.
09/2012—08/2015	PhD Scholarship of the German National Academic Foundation
06/2012—06/2015	Associated PhD student of the International Research Training Group 1830 "Complex Membrane Proteins in Cellular Development in Health and Disease"
12/2008—05/2011	**Diplom-Biologe**, Biology, Johannes Gutenberg University, Mainz; graduated with distinction (1,0) **Diploma Thesis:** *Structure determination by x-ray crystallography and functional characterisation of the hemoglobin of* Lama pacos
04/2006—12/2008	**Bachelor of Science**, Molecular Biology, Johannes Gutenberg University, Mainz; graduated with distinction (1,1) **Bachelor thesis:** *The keratins of the lamprey* L. fluviatilis*: expression and biochemical characterisation*
06/1996—06/2005	**General qualification for university entrance** Elly-Heuss-Gymnasium, Wiesbaden (1,2)

Employment

11/2011—04/2012	Private coaching for school pupils at Die Lernhilfe e.K.
05/2011—07/2011	Research assistant at the Institute of Molecular Biophysics, Johannes Gutenberg University, Mainz
11/2009 & 11/2010	Research assistant at the Institute of Microbiology and Wine Research, Johannes Gutenberg University, Mainz
07/2005—03/2006	Alternative civilian service, St. Josefs-Hospital, Wiesbaden

Internships

09/2011—12/2011	Veterinary Medicine, Hessian State Laboratory, Gießen
02/2009—04/2009	Max Planck Institute for Polymer Research, Mainz **Topic:** *pH dependence of potassium ion transport mediated by lysine-valinomycin across lipid membranes*

International Conferences

08/2014	18th IUPAB International Biophysics Congress, Brisbane, Australia; poster; **Young Scientist Travel Award**
07/2014	Mechanosensory Transduction Symposium, Gold Coast, Australia
05/2014	564th Haereus-Seminar "Physical Approaches to Membrane Proteins", Bad Honnef, Germany; poster
04/2014	57th Annual Meeting of the Canadian Society for Molecular Biosciences (CSMB), Banff, Canada; **invited plenary talk**
03/2014	International Workshop "Molecular Membrane Biophysics", Hünfeld, Germany; poster
04/2013	64th Mosbacher Kolloquium "Membranes in Motion", Mosbach, Germany; poster
06/2011	Joint Meeting of the Swedish and German Biophysical Societies, Hünfeld, Germany; poster

Zusammenfassung

Zellen und Organellen sind von Membranen umschlossen, die aus einer Lipid-Doppelschicht mit darin eingebetteten Membranproteinen (MP) bestehen. Diese verrichten essentielle Funktionen, und insbesondere α-helikale MP sind von wesentlicher pharmakologischer Bedeutung, da sie mehr als die Hälfte aller Zielproteine für Artzneimittel ausmachen. Es mangelt jedoch an Kenntnissen aus der Membranproteinforschung, da MP eine Membran-mimetische Umgebung benötigen, um ihre native Struktur und Funktion zu bewahren, und dementsprechend *in-vitro*-Untersuchungen nicht ohne Weiteres zugänglich sind. MP müssen rekonstituiert, d.h. aus Detergenzmizellen in eine Lipid-Doppelschicht überführt werden, um Einblicke in vektorielle Funktionen zu erhalten, wie im Falle von Kanälen und Transportern, sowie in ihre Topologie, also ihre Konformation und Orientierung im Kontext der Membran.

Das Ziel dieser Arbeit war die Aufklärung der Membrantopologie von Mistic, einem essentiellen Regulator der Biofilmbildung in *Bacillus subtilis*, der aus vier α-Helices besteht. Für eine stabile Konformation ist Mistic bekanntermaßen auf eine hydrophobe Umgebung angewiesen. Allerdings besitzt Mistic eine ungewöhnlich hydrophile Oberfläche, und seine Helices sind deutlich kürzer als die Transmembranhelices typischer integraler MP. Daher steht es zur Diskussion, wie Mistic seine Assoziation mit dem hydrophoben Membrankern bewerkstelligt. Um dieser Frage nachzugehen, wurde Mistic hergestellt, aufgereinigt, rekonstituiert und topologischen Studien unterzogen.

Mistic wurde rekonstituiert, indem in Anwesenheit von Lipiden die Detergenzkonzentration durch Zugabe von Cyclodextrin verringert wurde. Um die Vorteile, die diese Strategie bietet, voll auszunutzen, wurde ein quantitatives Modell entwickelt, das den supramolekularen Zustand des Rekonstitutionsansatzes beschreibt und die Vorhersage des Rekonstitutionsverlaufs sowie dessen Schnittpunkt mit den Phasengrenzen erlaubt. Automatisierte Titrationen ermöglichten die spektroskopische Überwachung der Mistic-Rekonstitutionen in Echtzeit.

Auf Grundlage des etablierten Rekonstitutionsprotokolls wurde die Membrantopologie von Mistic mit Hilfe von Fluoreszenzspektroskopie und Orientierter Zirkulardichroismusspektroskopie untersucht. Die Ergebnisse dieser Experimente offenbaren, dass Mistic eine Ausnahme zu der im Allgemeinen beobachteten Transmembranorientierung α-helikaler MP darstellt, da Mistic eine ungewöhnliche Topologie parallel zur Membranebene aufweist, die mit jüngsten Molekulardynamiksimulationen übereinstimmt.

Eidesstattliche Erklärung

Ich erkläre an Eides statt, dass mir die Promotionsordnung des Fachbereiches Biologie der Technischen Universität Kaiserslautern in der derzeit gültigen Fassung bekannt ist. Desweiteren versichere ich, die vorliegende Arbeit selbständig verfasst, keine anderen als die angegebenen Quellen und Hilfsmittel benutzt, sowie die Ergebnisse anderer Mitarbeiter bzw. Autoren klar gekennzeichnet zu haben. Ich habe diese Dissertation oder Teile daraus keinem anderen Fachbereich als dem der Biologie der Technischen Universitäat Kaiserslautern vorgelegt und mich zu keinem früheren Zeitpunkt um den Doktorgrad beworben.

Kaiserslautern, 1. Februar 2016 Martin Textor